Air Entrainment by Bow Waves

Thesis by
Tricia Ann Waniewski

In Partial Fulfillment of the Requirements
for the Degree of
Doctor of Philosophy

California Institute of Technology
Pasadena, California

1999

(Submitted 27 October 1998)

Acknowledgements

My thesis would not possibly be complete without acknowledging many sources of assistance. First, I am grateful for the financial support of the Office of Naval Research under grant number N00014-94-1-1210, and the American Society of Mechanical Engineers through a graduate teaching fellowship. Second, I am grateful to the many people whose names appear in the following paragraphs.

I would like to recognize the contributions of the Thomas Building staff, especially Jackie Beard, Cecilia Lin, and Dana Young and also Fran Matzen of the Keck Building staff. They all helped me in a friendly way through mazes of paperwork so that things were finished on time.

My experiments required a great deal of technical assistance. Special thanks go to Rich Eastvedt for his cheerful help with seemingly every aspect of the Keck SB lab, especially for patiently cutting a 4"x3" hole in 1" thick stainless steel and for figuring out how to ship hundreds of pounds of fragile lab equipment across the country. Thanks also go to Hai Vu for designing and building numerous ingenious and neatly packaged electronic circuits required for my experimental measurements. In addition, I am thankful for the machining and design expertise of Joe Fontana, Russ Green, Rodney Rojas, and John VanDeusen. Finally, I would like to thank Rod Barr, Bob Kowalyshyn, and Jim McGurrin at Hydronautics Research for their assistance in a series of experiments in March 1998.

My fellow graduate students were both my friends and my colleagues; they all made the basement of Thomas a cool place to spend five years. I gratefully acknowledge their help and friendship–especially Robert Behnken, Michael Kaneshige, Anna Karion, Amy Warncke Lang, Bruce Nairn, N.V.V. Rajan, Clancy Rowley, Roberto Zenit, and the members of the "Thomas Ensemble." I would also like to thank Christopher Hunter, Hilla Shaviv, and all of the undergraduate students who provided much needed assistance with my experiments and good company in the lab.

My advisor, Christopher Brennen, extended his professional guidance and support to me since my very first day at Caltech. His vast experience in experimental fluid mechanics was indispensable. I was also very fortunate to have a second advisor, Fredric Raichlen. Many productive research ideas originated in conversations with him, often as I was doing

experiments in the lab. I express my deepest gratitude to both of my advisors. In addition to offering many thoughtful research ideas, Allan Acosta was a fellow flutist who encouraged my interests in music and engaged in many delightful hours of chamber music with myself and other graduate students. Morteza Gharib and Theodore Wu served on my thesis committee and made many interesting comments and suggestions. Finally, I am grateful for the continued encouragement of John Gardner at the Pennsylvania State University.

Most importantly, I would like to acknowledge the loving support of my family. My brother, Brian Waniewski, who always had a humorous story to tell. My parents, David and Nancy Waniewski, who never failed to call and write to see how I was doing every week. And to my husband, Sudipto Sur, whom I met while I was a graduate student at Caltech, "চন্দন, আমি তোমাকে ভালোবাসি। " I thank you all with much love.

Abstract

Experimental studies of air entrainment by breaking waves are essential for advancing the understanding of these flows and creating valid models. The present study used three-dimensional simulations of a bow wave to examine its air entrainment process. The simulated waves were created by a deflecting plate mounted at an angle in a super-critical free surface flow. Since the air entrainment process is closely coupled with breaking wave dynamics, the present study included both air entrainment and free surface measurements.

Measurements of the free surface were obtained from the simulated bow waves at two scales, and also from the bow wave created by a towed wedge model. Contact line and bow wave profile measurements for the different experiments were compared, demonstrating the similarity of the experimental simulations to the towed model experiments. The plunging wave jet shape was measured in the larger scale stationary model and towed model experiments and used to calculate jet thickness, velocity, and impingement angle. The bow wave profile data from the towed model experiments were used to investigate the scaling of the wave with the flow and geometric parameters. Surface disturbances were observed on the plunging wave face, and their wavelength, frequency, and velocity were measured.

The primary mechanisms for air entrainment were the impact of the plunging wave jet and individual droplets in the splash region on the free surface. The air entrainment process was observed in the larger scale stationary model experiments, and the air bubbles were entrained in spatially periodic bubble clouds. Due to the shallow depth in these experiments, measurements of only the larger bubbles in the initial stages of air entrainment were obtained. An impedance based void fraction meter, developed specifically for the purpose, was used to measure void fractions and bubble size distributions beneath the wave. The bubble cloud size and void fraction increased with downstream distance.

There were indications that the surface disturbances control the periodicity of the bubble clouds. Namely, the surface disturbances divide the plunging liquid jet sheet into a series of plunging wave jets, each entraining air into a separate bubble cloud beneath the free surface.

Contents

List of Figures

List of Tables

Nomenclature

Symbol	Description
A	Flume width x depth (m^2)
α	Void fraction (%)
A_p	Projected area (m^2)
$b(x, z)$	Function describing hull surface
C	Capacitance (F)
C_d	Drag coefficient
d	Depth (m)
D	Drag force (N)
ΔT_{max}	Maximum spike width (s)
Δt	Fixed time interval (s)
δ	Interfacial region thickness
ϵ	Ratio of beam/length
ϵ	Electrical permittivity?
$\mathbf{F}$	Froude number based on depth, $\mathbf{F} = U/\sqrt{gd}$
g	Gravitational acceleration (m/s^2)
h	Elevation change between manometer columns
II	Distance between static pressure taps
i	$\sqrt{-1}$
k	Phase, $k \in 1, 2$
L	Length of the finite hull body

l	Bubble chord length
l_{max}	Location of maximum wave height in the r-direction
M	Local void fraction measurement (0 or 1)
N	Bubble count rate (counts/s)
n	Bubble count rate (counts/cm)
ν	Kinematic viscosity (m^2/s)
ω	Excitation frequency
ϕ	Velocity potential function
ϕ	Dihedral angle (degrees)
Q	Flow rate (m^3/s)
r	Horizontal coordinate along the deflecting plate
R	Resistance (Ω)
Re	Reynolds number
ρ	Density (kg/m^3)
$\overline{R}$	Average bubble radius (mm)
r'	Non-dimensional coordinate along the deflecting plate, $r' = r/\mathbf{F}d$
σ	Electrical conductivity
t	Time (s)
τ	Sampling time (s)
θ	Wedge half angle (degrees)
t_o	Reference time (s)
U	Free stream velocity (m/s)
V_{max}	Maximum spike amplitude (V)
We	Weber number
x	Streamwise coordinate
x_o	Reference point in space, measurement location
x'	Non-dimensional streamwise coordinate, $x' = x/\mathbf{F}d$
y	Cross stream coordinate

y'	Non-dimensional cross stream coordinate, $y' = y/\mathbf{F}d$
z	Vertical coordinate
Z	Complex impedance
Z	Free surface height
Z_{max}	Maximum wave height
Z'	Non-dimensional free surface height, $Z' = 90Z/\mathbf{F}d\theta$
Z''	Non-dimensional free surface height, $Z'' = Z/\mathbf{F}d$

Chapter 1

Introduction

Air entrainment by breaking waves has been an active area of research for many years because of its important role in chemical, biological, and physical processes which occur at the air-water interface. Since over 70% of the earth's surface is covered by water, these processes occur on a large scale. In the oceans, white caps are responsible for most of the air entrainment, and on average the world ocean white cap coverage is about 1% [35]. The air entrainment process dissipates surface wave energy. Lamarre and Melville [25] found that 40% of the total pre-breaking wave energy can be lost in breaking, and up to 50% of this energy loss is expended entraining air. In addition, the air entrainment process enhances air-water gas exchange [46]. Furthermore, the air entrainment process and the oscillations of both the individual bubbles and the clouds of bubbles it creates are a source of underwater sound. These bubbles also affect the propagation of underwater sound, and much of the early work in this area is summarized in Kerman [22]. Finally, the bursting of these bubbles at the air-water interface provides a mechanism for ejecting matter into the lower atmosphere such as salt nuclei [5] and bacteria [19, 4]. A description of recent contributions to the knowledge of wave breaking and its role in air-sea interaction is found in Melville [33].

1.1 Motivation

The motivation for studying air entrainment by *bow* waves comes from the field of naval hydrodynamics. When a displacement type ship moves through the water, it typically

Destroyer ship	White-water wake length (ft)	Waterline hull length (ft)	Midsection draft, d (ft)	Velocity, U (ft/s)	Froude No., $U/\sqrt{gd}$
1	3250	369	14.3	33.8	1.58
2	2370	369	14.3	27.0	1.26
3	4450	369	14.3	42.2	1.97
4	2240	369	14.3	38.0	1.77
5	1800	369	14.3	38.0	1.77
6	1540	369	14.3	38.0	1.77
7	2310	369	14.3	38.0	1.77
8	2280	369	14.3	38.0	1.77
9	3760	400	14.0	42.2	1.99
10	1730	369	14.3	38.8	1.77
11	1540	369	14.3	38.8	1.77
12	3480	369	14.3	33.8	1.77

Table 1.1 Wake lengths for destroyer ships traveling at typical speeds. Reproduced from Peltzer (1984) with the author's permission.

creates a white-water (foamy, aerated, turbulent water) wake. The three main sources of air bubbles in these white-water wakes are:

1. Bow wave breaking.

2. Air entrainment into the ship's turbulent hull boundary layer at the free surface.

3. Ventilation, racing, and cavitation caused by the rotation of the propeller.

Other sources include: hull slap in a rough seaway, wave slap against the hull, Kelvin wave breaking, and hull cavitation [40]. These bubbles can change parameters related to ship efficiency and performance such as total resistance and propeller efficiency. One specific example is that bubbles in the near wake of the ship are often entrained into the flow around the propeller. These bubbles can be a source of cavitation nuclei and increase the probability of cavitation, a highly damaging phenomenon responsible for erosion of blade surfaces, noise, decreased performance, and induced vibrations.

In recent years, a specific interest in these flows arises from the need for signature estimation from white-water wakes created by destroyer ships, otherwise known as "ships of opportunity," in the United States Navy. The photographs in Figure 1.1 show bow

(a) USS Barry (DDG52), christened 4/23/94. The hull length is 506 ft., and the navigational draft is 32 ft.

(b) USS Ramage (DDG61), christened 6/8/91. The hull length is 504 ft., and the navigational draft is 31 ft.

Figure 1.1 Examples of bow waves created by guided missile destroyer ships underway. Both photographs are courtesy of the U.S. Navy.

waves created by a DDG52 and a DDG61 destroyer ship which are propelled by gas turbine engines to speeds over 30 knots (51 ft/s). The white-water wakes are also visible in these photographs, especially in Figure 1.1(b). These bubbles, particularly the smaller ($O(\mu m)$) diameter bubbles, and foam are remarkably stable and can persist in the wake for long distances. Table 1.1 lists typical white-water wake lengths for destroyer ships measured from aerial photographs; in one case the white water extended 0.84 miles behind the ship! In addition to being visible to the naked eye and in photographs, the white-water wakes can be detected by other methods as well, i.e., the foam, bubbles, and increased vorticity in the wake change the water's surface emissivity which can be detected by microwave radar, synthetic aperture radar, and infrared radiometry [40].

Despite the complexity of these flows, numerical models have been developed and computations performed. Carrica et al. [7] demonstrated that the bubbles introduced at the bow of the ship have significant effects on the wake; however, this study and others lack an accurate model for the bow wave air entrainment process and use arbitrary bubble sources unrelated to the flow parameters. Increasing the accuracy of these calculations depends on including accurate models for the bow wave air entrainment process (perhaps similar to Baldy's [1] model for bubbles created by wind waves), and experimental work is the key to developing them.

1.2 Related studies

There are no records in the literature of void fraction and bubble size distribution measurements beneath breaking bow waves in the field, probably because this type of experiment would be exceedingly difficult and costly. There have been, however, numerous studies which measure void fraction and bubble size distributions beneath other types of plunging breaking waves including white caps, and two-dimensional and three-dimensional plunging waves created in laboratory wave tanks. An early example of such a study is Blanchard and Woodcock's [5] bubble size distributions under white caps. Many of the more recent theoretical and experimental studies were motivated by the 1987 NATO Advanced Research Workshop on Sea Surface Sound. Theoretical studies such as Prosperetti et al. [41] of the

acoustic behavior of bubbles produced by breaking ocean waves resulted in models requiring experimental validation, i.e., the acoustic behavior (sound speed) is directly related to the void fraction which can be experimentally measured. Sets of void fraction measurements were made by Lamarre and Melville for two-dimensional plunging waves [25], three-dimensional plunging waves [27], and white caps [26] using impedance-based void fraction instrumentation. One of their observations was that immediately after breaking a bubble cloud is created which can have a void fraction as high as 30–40%. This cloud, primarily comprised of large (O(mm)) bubbles, then degasses rapidly leaving behind a diffuse plume of microbubbles. Bubble production rates and size distribution measurements for the larger bubbles were made by Cipriano and Blanchard [15] and Loewen et al. [28], among others. Bubble populations in fresh and salt water were compared in studies such as Cartmill and Su [8] and Loewen et al. [28]. In general, bubble plumes in salt water contained larger quantities of bubbles and the bubbles were smaller in size whereas the plumes in fresh water contained fewer quantities of bubbles which were larger in size because their surface physical-chemical properties allow them to coalesce. The exact differences in the size distributions seem to depend on experimental techniques.

The air entrainment process for bow waves (continuously breaking plunging waves) is similar to that for an inclined plunging jet in cross flow [13]. There are numerous studies of air entrainment by plunging jets because of its wide spread applications; these studies have documented different air entrainment processes for plunging jets which have been shown to be dependent on various parameters including flow rate, jet surface turbulence, and jet geometry. Van de Sande and Smith [48] reported that high velocity jets (10–25 m/s) entrained air by "dragging" their boundary layer into the receiving liquid pool, while low velocity (2–5 m/s) jets entrained air because the receiving liquid cannot follow undulations on the jet surface [49]. Sene [43] continued this work, adding experimental and theoretical results for both planar and circular jets at low and high velocities. McKeogh [31] defined a critical velocity for the inception of air entrainment, and later studied the effects of jet turbulence levels [32]. Koga [23] and Detsch and Sharma [18] measured the critical angle for the inception of air entrainment. Bonetto and Lahey [6] were among the first to map local void fraction and velocity fields beneath an axisymmetric plunging jet, and additional

measurements were made and theory developed for a two-dimensional supported jet [16, 17]. A recent review by Bin [3] discusses these studies and others concerning gas entrainment by plunging liquid jets. Chanson and Cummings [12] use the information from these works to predict quantity of air entrained, bubble sizes, and bubble penetration depth for plunging breakers achieving good comparison with experimental field data from other researchers.

Lamarre and Melville [25] showed that the air entrainment process is closely coupled with the breaking wave dynamics, but virtually all of the investigations described above focus on "two-dimensional" wave breaking and there is little information on the highly three-dimensional processes which occur in a breaking bow wave. Therefore, direct application of the results from these studies to the bow wave air entrainment problem would be inappropriate.

1.3 Approach taken by this research

The research described herein used a three-dimensional simulated bow wave to examine the air entrainment process. The simulated bow wave was produced using a stationary deflecting plate in a supercritical free surface flow in a laboratory flume (recirculating free surface water channel). This stationary, simulated bow wave allowed for detailed examination of the breaking process, and towing tank tests using similar models and flow conditions confirmed that this was a valid simulation.

These experimental simulations were conducted at two scales. The initial studies focused on how the bow wave changed with the flow parameters and the geometric parameters, information which is a necessary prerequisite for understanding the air entrainment process. Flow visualization studies were performed and an electronic point gage was used to study the three-dimensional shape of the bow waves and the manner in which they impinge the free surface.

Further studies examined the air entrainment process. Bubble size distributions and void fraction were measured using high speed videos and an impedance based void fraction meter (IVFM). Because of the limited depth in the flume, only the initial stages of air entrainment were investigated.

1.4 Description of thesis contents

The following chapters present a study of the bow wave breaking process and a study of the air entrained. A description of the experimental equipment is presented in Chapter 2. Chapter 3 contains two different theoretical analyses of the contact line of the bow wave on the hull surface. Experimental measurements of the free surface are presented and discussed in Chapter 4. In Chapter 5, the air entrainment process is detailed and experimental measurements are presented. In addition, the wave breaking process and the resulting bubble clouds are related. Chapter 6 is a summary of the work presented in this thesis and a collection of ideas for future work.

Chapter 2

Experimental Equipment

This chapter presents a description of the facilities and the instrumentation used in the simulated bow wave experiments.

2.1 Facilities

2.1.1 40 m long flume

The larger scale experiments were conducted in a 40 m long tilting flume at a slope of one vertical to fifty horizontal. The flume is 109 cm wide and 61 cm deep with 1.3 cm thick tempered glass sidewalls and a stainless steel bottom plane to within ± 2.5 mm. It was filled with city tap water at about 23°C. A schematic is shown in Figure 2.1, and details are given in Vanoni et al. [50]. Flow rate, Q, is measured using a venturi meter and the depth, d, is measured with a point gage. The maximum discharge is approximately 0.394

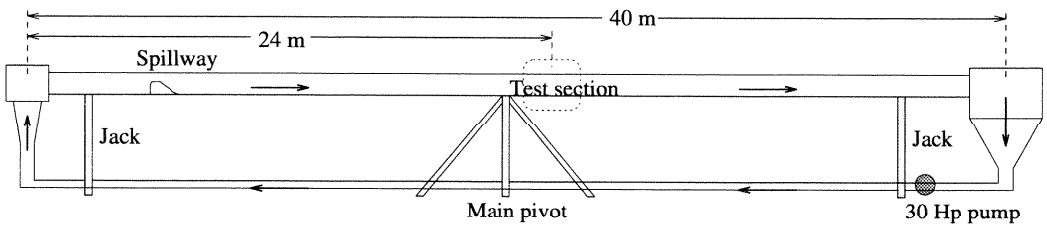

Figure 2.1 Schematic of the 40 m flume, W.M. Keck Laboratory of Hydraulics and Water Resources at Caltech.

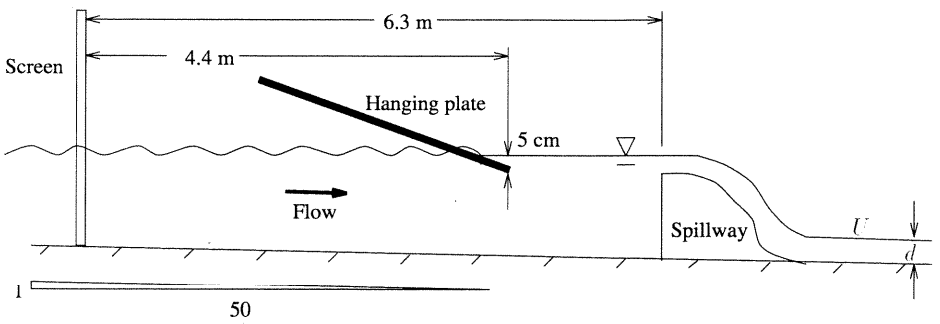

Figure 2.2 Upstream end of the 40 m flume.

m^3/s. The mean velocity of this flow, U, was calculated using $U = Q/A$ where $A = 1.1 \cdot d$ m^2. To create a super-critical flow, a 20.3 cm high two-dimensional spillway section was installed at the upstream end of the flume, downstream of a 8.1 m long reservoir. It was made of epoxy painted wood and was secured to the flume bottom using two bolts. A seal was created between the spillway section and the flume bottom with a rubber gasket, and a seal was created between the spillway section and the glass sidewalls using polyethylene caulking. Although the reservoir provided a settling region for the inflow which dissipated, to some extent, the larger scale turbulence at the flume inlet, additional flow-smoothing devices were installed. These included a wire screen (3 mm square holes) and a hanging steel reinforced lucite plate whose downstream edge was submerged approximately 5 cm beneath the free surface. Figure 2.2 shows the location of the flow smoothing devices and the spillway section.

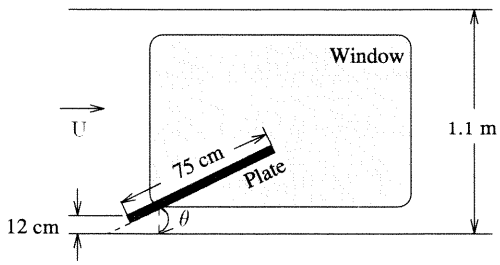

Figure 2.3 Test section in the 40 m flume.

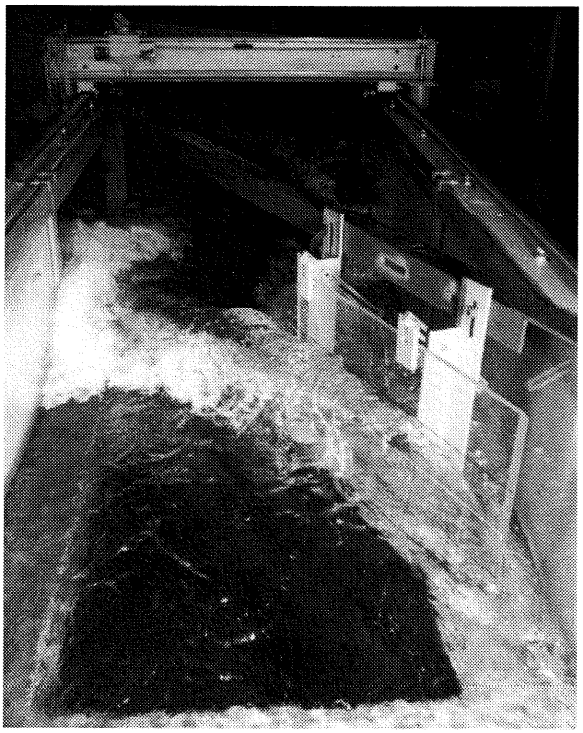

Figure 2.4 Photograph of the test section in the 40 m flume viewed from upstream; $\theta = 13.4°$, $\phi \approx 15°$, $U = 2.45$ m/s, $d = 11.45$ cm, and $\mathbf{F} = 2.31$.

The test section is located approximately 24 m (or over 200 depths for the flows investigated) downstream of the spillway and is shown in Figure 2.3. This location ensured a fully developed flow and also gave the air bubbles entrained in the flow downstream of the deflecting plate the maximum time to settle out. The test section has an 80.0 cm wide, 121 cm long, and 2.5 cm thick glass window fitted into the stainless steel bottom. Above this window, a 75 cm long by 50 cm high lucite plate was mounted at an angle θ to the oncoming flow to simulate a wedge shaped hull with half angle θ. The dihedral angle, ϕ, the angle between the plate surface and the undisturbed free surface, could also be changed. The plate's leading edge was machined to a sharp edge and displaced 12 cm from the glass flume sidewall to reduce the effect of the boundary layer on the wall of the flume. A steady breaking wave, similar to that observed at the bow of a ship, is created as the flow rides up on the plate as shown in Figure 2.4. The flow could also be observed through the glass

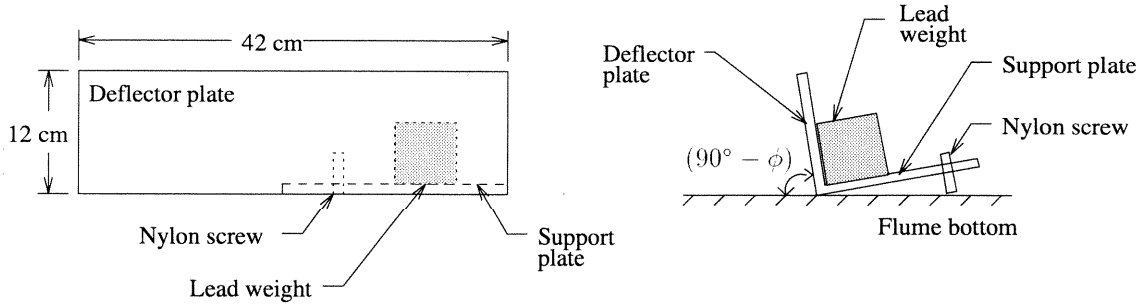

(a) Front view. (b) Side view.

Figure 2.5 Deflector plate used in the 2.6 m flume experiments.

sidewalls of the flume and from below through the glass window mounted in the bottom. A mirror was supported at an angle of 45° beneath the flume to facilitate these observations.

2.1.2 2.6 m long flume

Smaller scale experiments were conducted in a recirculating glass bottom tilting flume 265 cm long, 45.9 cm wide, and 12.7 cm deep. Tilting the flume achieved a more uniform flow through the test section. It was filled with city tap water at about 23°C, and the flow was adjusted using both a flow control valve downstream of the pump and a flap nozzle located at the entrance to the channel. For these experiments, super-critical flows approximately 1 cm deep were created. A mercury/water manometer connected to a standard orifice meter was used to determine the flow rate, Q (maximum about 0.01 m^3/s). It was connected to an orifice meter, was read to ± 1 cm mercury, and the reading converted to flow rate using its calibration graph. Upstream of the test section, the depth, d, was measured at five or more cross-stream locations using a point gage. Although the point gage could be read to ± 0.1 mm, the free surface fluctuated by as much as ± 0.7 mm during the higher velocity flows. This error was minimized by positioning the point gage tip so that it contacted the water 50% of the time. The mean depth was used to calculate the velocity of this flow, $U = Q/A$ where $A = 0.459 \cdot d$ m^2.

The test section was 35 cm downstream of the flap nozzle exit and contained a lucite

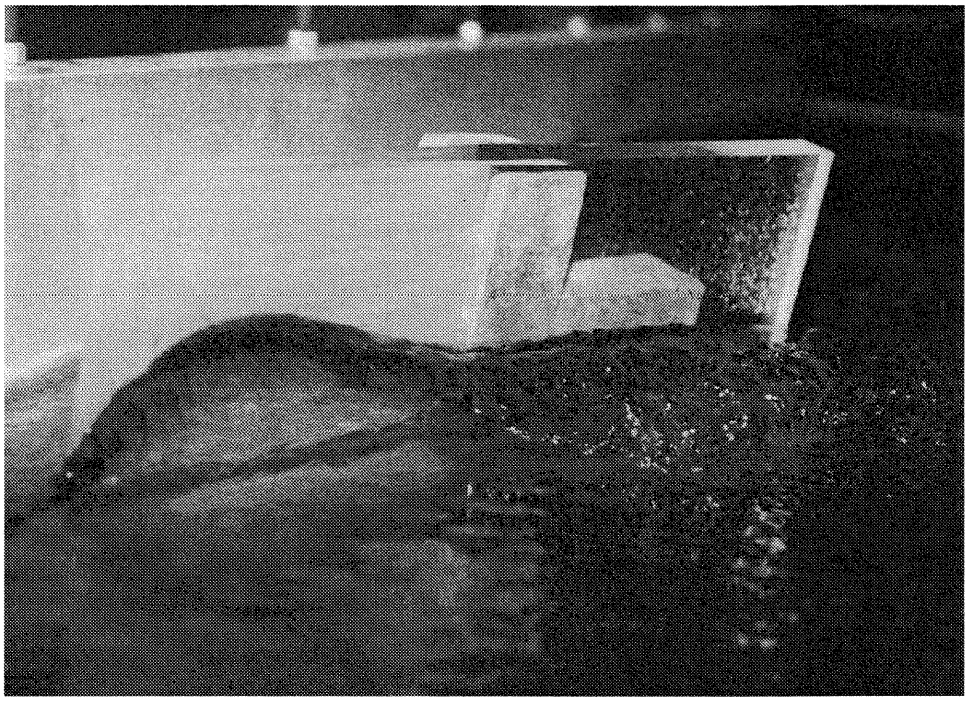

Figure 2.6 Photograph of the deflector plate in the 2.6 m flume experiments; $\theta = 25°$, $\phi \approx 10°$, and $\mathbf{F} = 3$.

deflector plate 12 cm high and 42 cm long. The deflector plate and its support shown in Figure 2.5 were displaced a few centimeters from the flume wall similar to the 40 m flume. Lead weights were placed on the support plate to keep it in place. A nylon screw through the support plate allowed for adjustment of the deflecting plate dihedral angle, tilting the plate toward the flow. The dihedral angle, ϕ, was measured using a protractor and a flat surface. The angle between the free stream and the plate, θ, was measured using an electronic point gage to be described in section 2.2.1. A photograph of the wave created by the deflector plate in this facility is shown in Figure 2.6. Kriegrocine dye injected upstream of the plate was used to enhance the contrast in this photograph.

2.1.3 Towing tank

Towed wedge experiments were conducted in a 126 m long, 7.5 m wide, and 3.7 m deep tank at Hydronautics Research, Inc., in Fulton, MD. The towing carriage is shown in Figure 2.7; its maximum velocity was approximately 5.2 m/s. The towing tank was filled with fresh water at about 16°C during these experiments.

Two wedge models were towed in these experiments, and these are shown in Figure 2.8. The smaller wedge had a bow half angle $\theta = 13°$, and the larger wedge had a bow half angle $\theta - 26°$. Each model consisted of two 1.3 cm thick lucite side panels, and 0.64 cm thick aluminum bottom and back panels attached to a frame constructed of 5.1 cm by 5.1 cm aluminum angles. Silicone was used to seal the seams, making the wedges water tight. In addition, a larger 0.64 cm thick aluminum bottom plate could be fastened to the bottom of either wedge as can be seen in Figure 2.8. The corners of the plate, in plan view, were rounded and the bottom of leading edge was cut away at an angle. For the larger wedge model, this larger bottom plate extended approximately 20.3 cm in all directions from the wedge perimeter.

A photograph of the towing carriage with the model is shown in Figure 2.9. The model was suspended from two force cells which were bolted to a steel I-beam. Clamps secured the I-beam to a support structure on the towing carriage which could be raised or lowered to change the draft of the wedge models. The carriage towed the models along their line of symmetry in the center of the tank.

2.1.4 Bubbly column

A bubbly-column-two-phase flow facility was used to calibrate the impedance based void fraction meter (IVFM) to be described later in section 2.2.3. A schematic of this facility may be found in Kytomaa [24]. It included a vertical lucite pipe 10.2 cm in diameter with an air injector located at the bottom of the pipe. The injector produced air bubbles of uniform size with a diameter of roughly 5 mm (at the injector), and the air flow rate was adjustable. Two static pressure taps located $H = 1.1$ m apart, and approximately equally spaced above and below the IVFM probe, were connected to an inverted manometer. The elevation change between the manometer columns is expressed as h, and the steady state

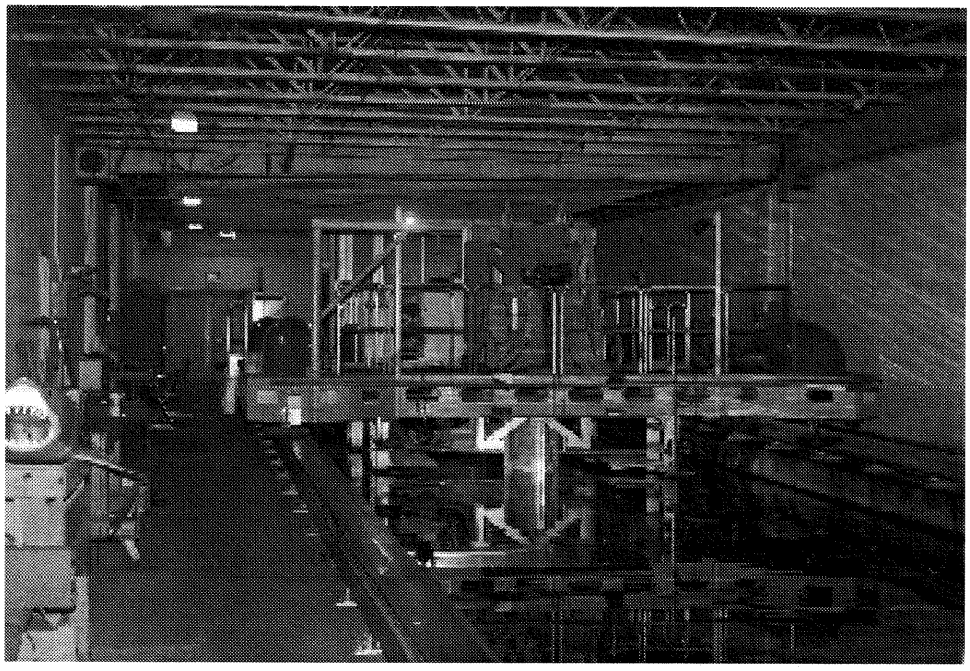

(a) Front view of towing carriage at one end of the tank. The wedge model can be seen suspended from the carriage hanging into the water at the center of the tank.

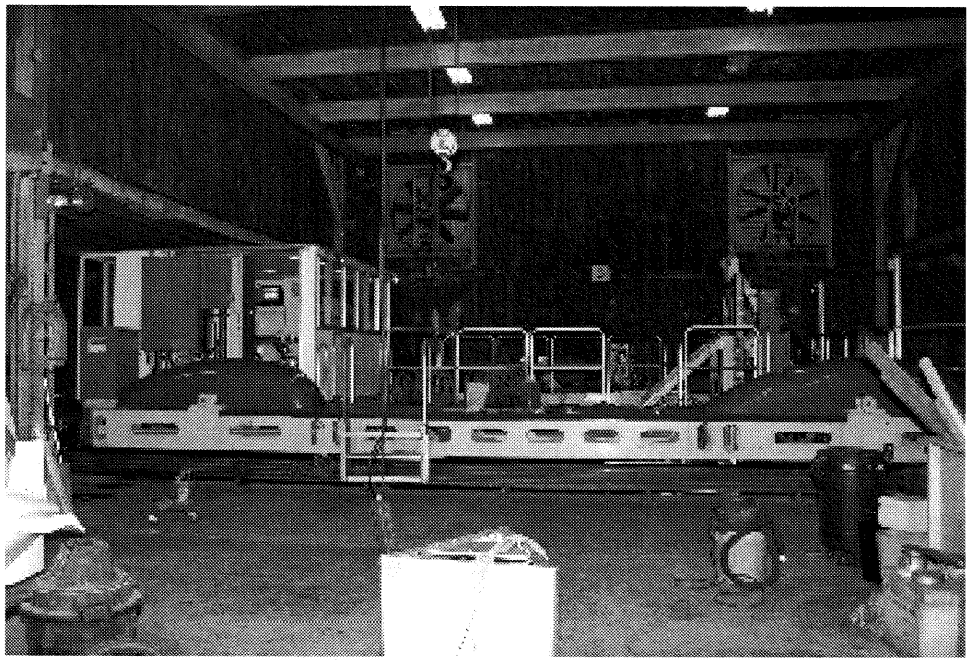

(b) Side view of towing carriage in the middle of the tank. A control room visible at the rear of the carriage housed the electronics for the experiment.

Figure 2.7 Towing carriage (Hydronautics Research, Inc.).

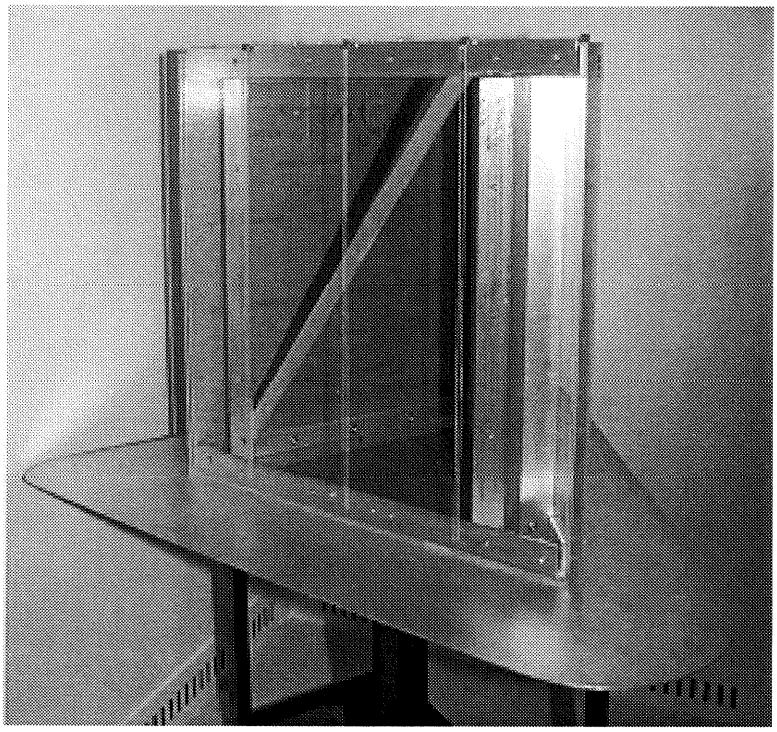

(a) Larger wedge, $\theta = 26°$.

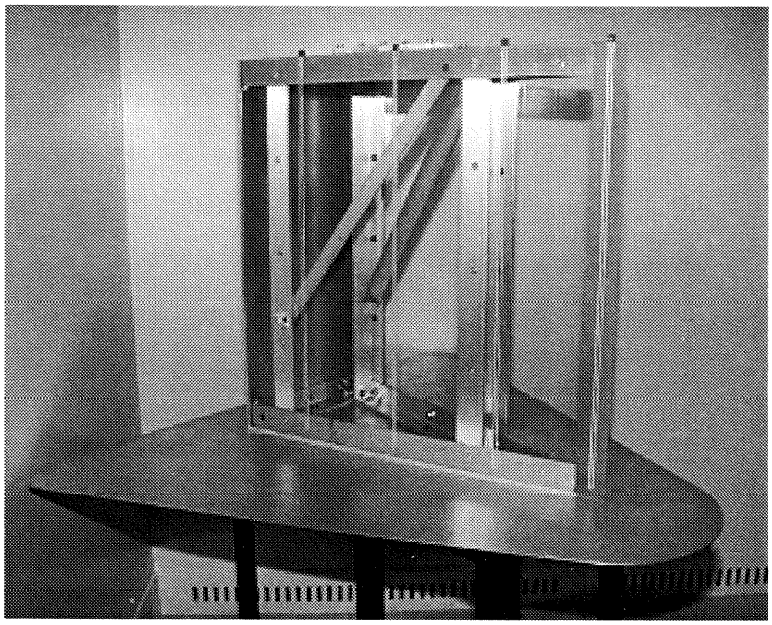

(b) Smaller wedge, $\theta = 13°$.

Figure 2.8 Wedge models shown with larger bottom plate for towed model experiments.

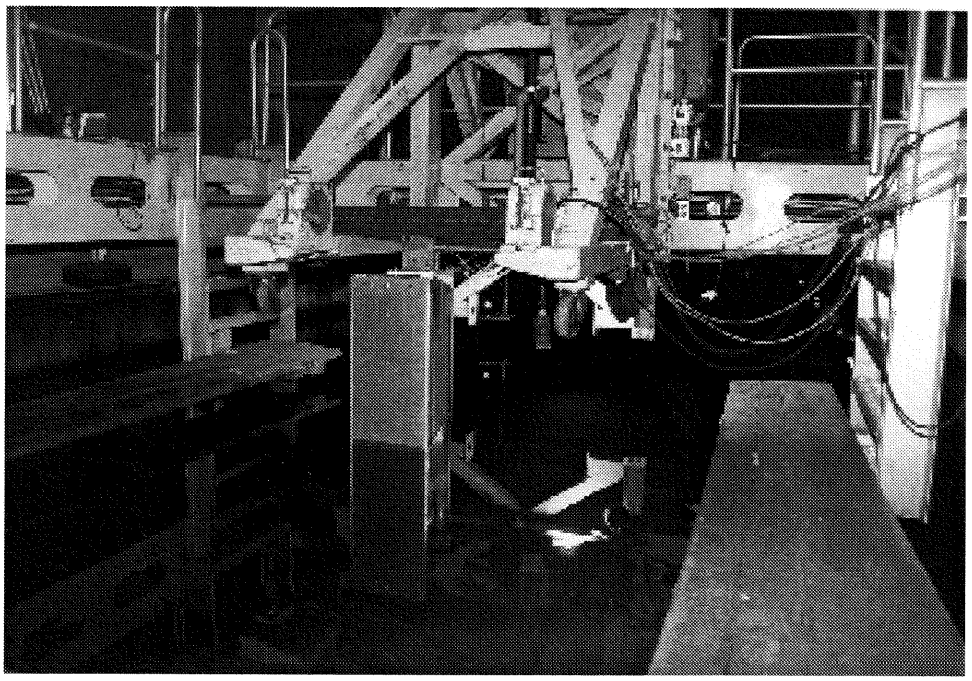

Figure 2.9 View of wedge model from the rear of the towing carriage (Hydronautics Research, Inc.).

void fraction, α, was obtained using the relation $\alpha = h/H$ [2]. Figure 2.10 shows examples of two different void fraction conditions in this facility.

A schematic of the test section is shown in Figure 2.11. The IVFM probe tip was held in place by a 0.64 cm diameter brass tube bent at a right angle in the shape of an L, 10.5 cm by 27.9 cm. For the calibration, the probe tip pointed downward and the brass tube was held in place by a lucite support. The lucite support consisted of two parts. First, a 5.1 cm diameter lucite piece was press fit with epoxy into the vertical lucite pipe of the test section. Then, a second lucite piece, 3.8 cm diameter and 12.7 cm long was threaded into the first and an O-ring created a seal between the two parts. The brass tube was located in the center of the lucite support, and a seal was created between the tube and the support using vacuum grease and an O-ring. A nylon set screw prevented rotation of the brass tube. Two wires extended from the IVFM probe tip through the brass tube to the associated electronics for the IVFM.

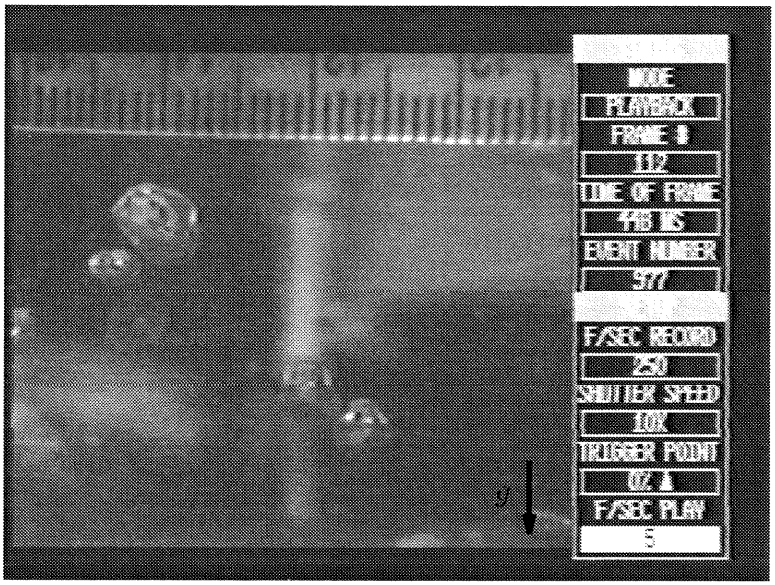

(a) Void fraction, $\alpha = 1.13\%$.

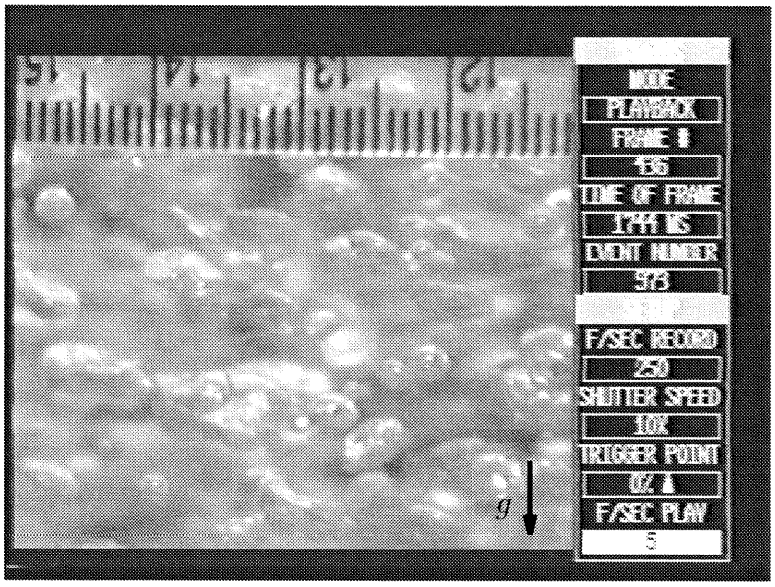

(b) Void fraction, $\alpha = 8.94\%$.

Figure 2.10 Examples of void fraction conditions in the bubbly column facility. A metric ruler is shown in the foreground, and the IVFM in the center of the column is obscured by bubbles. The direction of gravitational acceleration, g, is indicated.

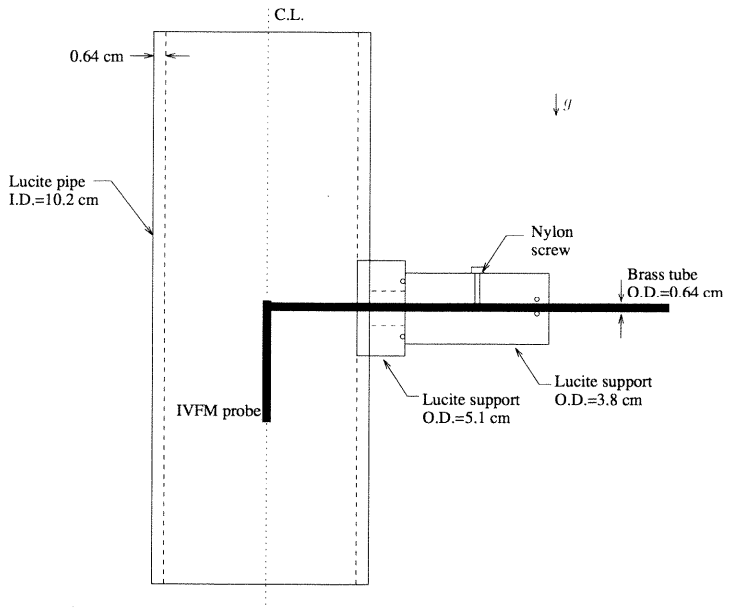

Figure 2.11 Schematic of bubbly column test section with IVFM support.

2.2 Instrumentation

2.2.1 Free surface probes

The location of the free surface of the wave was measured using an electronic point gage. The tip of the gage was a sharpened stainless steel rod 1.64 mm in diameter, and a reading was taken when the tip of the rod was in contact with the water surface 50% of the time. This was accomplished using an electronic system where the percentage of contact, time-averaged over several seconds, could be varied and set to a desired value. A light emitting diode was used to indicate when this desired immersion percentage was achieved. The circuit diagram of the free surface probe electronics is shown in Figure A.3. The vertical position of the electronic point gage could be controlled manually, or a motor driven by the circuit shown in Figure A.4 could be used to make the electronic point gage "hover" at the location of the free surface. For both the smaller and the larger scale experiments, the electronic point gage was attached to a carriage which travels on precision rails (parallel to

the bottom to within ± 0.1 mm) mounted to the top of the flume sidewalls. In the larger scale experiments, the carriage was moved in the cross-stream and downstream directions by two stepper motors. It is visible in Figure 2.4. In the smaller scale experiments, the carriage was moved manually.

A specific measurement procedure was used to define the contact line or the free surface height on the surface of the deflecting plate. In these experiments, an area of the plate above the contact line would be covered in a thin film of water and this wet region could produce false readings. This procedure was designed to avoid false readings produced when a droplet was "captured" between the point gage tip and the deflecting plate. First, the needle tip was positioned on the deflecting plate above the contact line. Second, the tip was moved away from the plate and lowered to the contact line height. Finally, the tip was moved toward the deflecting plate without changing the height and a reading was taken. For many flow conditions, in both the larger and the smaller scale experiments, the contact line was unsteady. In these experiments, an area of the plate above the contact line would be covered in a thin film of water and this wet region could produce false readings. Care was taken to position the probe so that it contacted the flowing water approximately 50% of the time.

For the larger scale experiments, the electronic point gage was also used to measure the free surface of the region containing the bow wave. The percentage of time that the point was immersed was preset, and a servo motor system connected to the point gage maintained this immersion percentage. The gage was connected to a linear voltage displacement transducer (LVDT) which produced an electrical signal which was, through calibration, proportional to the water surface elevation. A PC controlled the carriage stepper motors so that the electronic point gage could automatically traverse a sampling grid in the bow wave region. Figure 2.12 shows the various components of the data acquisition equipment.

2.2.2 Wave gages

In the larger scale experiments, three wave gages were used to measure the free surface height on the deflecting plate. A wave gage, shown in Figure 2.14, consists of a pair of electrodes spaced 0.64 cm apart. Each electrode was made using a pen which deposited

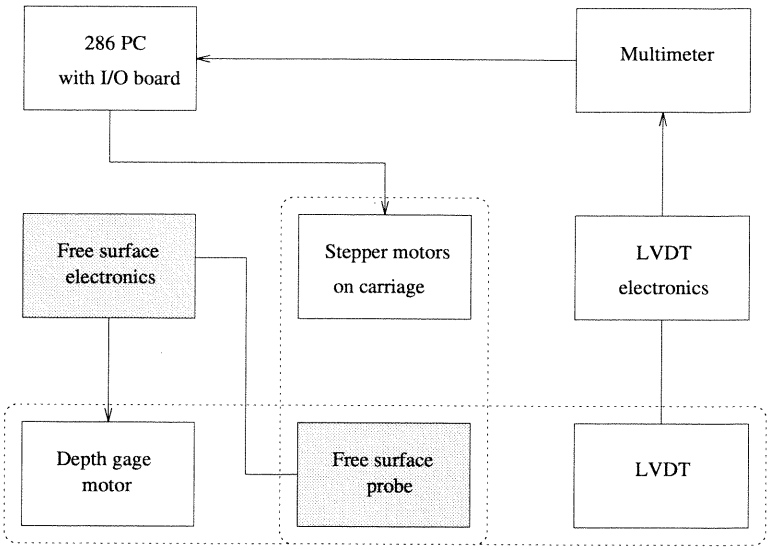

Figure 2.12 Free surface probe control and data acquisition system for the larger scale experiments in the 40 m flume. The solid lines indicate electronic connections, and the dotted lines indicate mechanical connections.

conductive silver traces on the deflecting plate surface. In order to produce electrodes which were flush with the plate surface, the traces were deposited in shallow grooves, 45 cm long and 1 mm wide. Figure 2.13 shows the deflecting plate with the location of the gages marked. The electrodes were connected using screw terminals to cabling which led to the electronics. The electronics measured the change in current flowing between the two electrodes and had a bandwidth of 2 kHz. As the water height increased, the impedance between the two electrodes decreased, thereby increasing the current flowing between the two electrodes. The circuit diagram for the wave gage electronics is included in Appendix A.

Although there was some runup and splashing on the wave gages, the data were only used to find the frequencies of oscillation of the free surface. Since absolute free surface heights were not measured, calibration of the gages was not required. Free surface oscillations in the upstream reservoir of the flume were measured using a wave gage consisting of a pair of stainless steel wires 0.26 mm in diameter spaced 4 mm apart. Attempts to use this type of wave gage in the test section upstream of the deflecting plate failed because the high flow velocities caused considerable splashing on the wires and disturbance to the free surface.

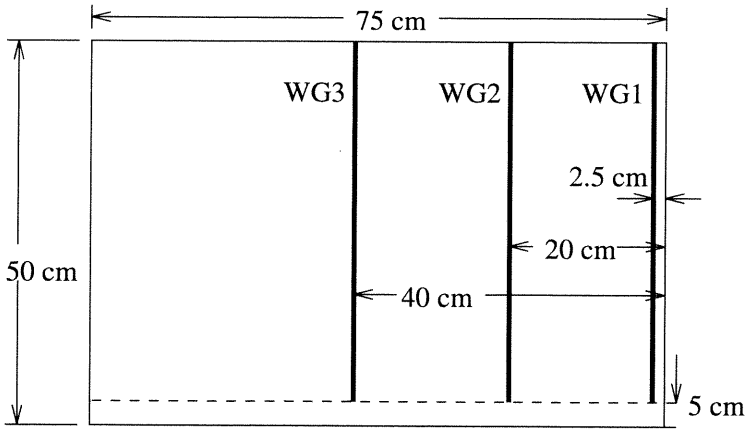

Figure 2.13 View of the deflecting plate with wave gages marked.

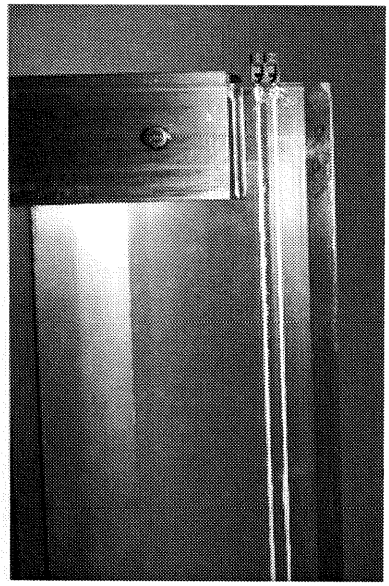

Figure 2.14 Photograph of the wave gage near the leading edge (WG1) on the larger angle wedge model.

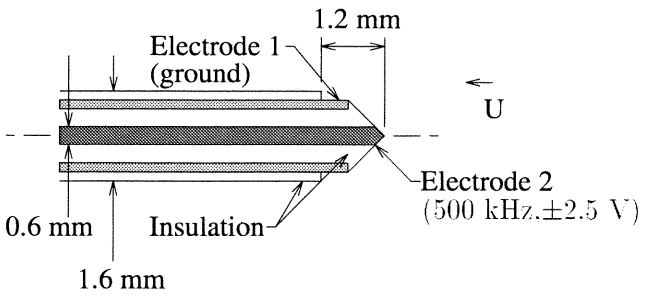

Figure 2.15 Cross sectional view of the IVFM probe (not to scale).

2.2.3 Impedance void fraction meter (IVFM)

An impedance based void fraction meter (IVFM) was developed to measure the void fraction, α, in this high speed, unsteady, multiphase flow. The IVFM probe consists of two concentric stainless steel electrodes based on a design by Chanson [10] and is shown in Figure 2.15. The outer annular electrode is a syringe needle with an outer diameter of 1.63 mm and a thickness of 0.3 mm. The inner electrode is a stainless steel rod with a diameter of approximately 0.6 mm. The inner electrode was wound with electrical tape and inserted into the syringe needle which was subsequently filled with epoxy. After the epoxy hardened, the tip was sharpened. Also, the outer electrode is insulated from the water except for a length of approximately 0.5 mm from the tip. The probe is mounted on a support system downstream of the probe.

The probe's small size allows it to respond to individual bubbles. Experiments with larger probes of this style did not produce desirable signal to noise ratios. Parallel plate style probes tested for use had grounding loop and vibration problems; they also entrained air in the separation zones generated by the plates.

The probe is immersed in the air-water mixture, and the impedance across the two electrodes increases with void fraction. This impedance, Z, can be modeled as a resistor, R, and a capacitor, C, in parallel so that

$$Z = \frac{R}{i\omega RC + 1} \tag{2.1}$$

where ω is the excitation frequency of the probe. Generally, the inductive impedance is negligible if the connecting cables are short. Following Bernier [2] we can rewrite the impedance in terms of the electrical conductivity and permittivity of the water. Maxwell [30] first modeled the effects of a dilute suspension of non-interacting spheres in a continuous phase on the bulk conductivity. He expressed the effective conductivity of the mixture, σ_{eff}, as a function of the volumetric concentration of the dispersed phase, α, the electrical conductivity of the dispersed phase σ_i, and the electrical conductivity of the continuous phase, σ_o

$$\sigma_{eff} = (1 - \frac{3\alpha}{\frac{2\sigma_o+\sigma_i}{\sigma_o-\sigma_i} + \alpha})\sigma_o. \tag{2.2}$$

For the case of air bubbles in water, $\sigma_o \ll \sigma_i$, and the expression reduces to

$$\sigma_{eff} = (1 - \frac{3\alpha}{2 + \alpha})\sigma_o. \tag{2.3}$$

As in Lamarre and Melville [26] the resistance, R, and capacitance, C, can be expressed as

$$R = \frac{K}{\sigma_{eff}}, C = \frac{\epsilon_{eff}}{K}, \tag{2.4}$$

where K is a constant with units l^{-1} depending on the geometry and spacing of the electrodes. Combining equations 2.1, 2.3, and 2.4 yields

$$Z = K(\frac{1 + \alpha/2}{1 - \alpha})(\frac{1}{\sigma + i\omega\epsilon}). \tag{2.5}$$

Equation 2.5 shows how the impedance would increase with an increase in void fraction. Furthermore, it implies that for low excitation frequencies ($\omega/2\pi \ll 1$ MHz), the impedance is mainly resistive but for high excitation frequencies ($\omega/2\pi \gg 1$ MHz), the impedance is mainly capacitive [26]. Operation in the resistive regime is desirable because of the problems with spurious signals and interference that can plague high frequency circuits [45]. Direct current excitation is seldom used for these types of probes because of polarization effects in the water.

The IVFM electronics were designed to detect a 1 mm diameter bubble moving at 2

m/s ($\Delta T = 0.0005$ s); therefore, the minimum frequency response required was 4 kHz. An oscillator generated a sinusoidal voltage signal of $\pm$ 2.5 V and 500 kHz which was applied to the inner electrode; the outer electrode is grounded. This frequency was chosen because the electronics were able to achieve the required frequency response while still operating in the resistive regime. When a bubble passes the probe tip, the current flowing between the two electrodes reduces, and a current meter circuit measures this change. The output is then low-pass filtered with a cutoff of 40 kHz and demodulated to provide a DC signal proportional to the local void fraction. The resulting DC signal from the IVFM is sampled using a data acquisition system with a data collection rate which was set according to the bubble velocity. The circuit diagram of the IVFM is included in Appendix A.

Single bubble tests were conducted to determine the sensitivity of the probe to bubble position. The probe was mounted in a water filled tank 25.4 cm wide, 50.8 cm long, and 30.5 cm deep with the tip pointing downward. A small air pump was connected to a 1.66 mm diameter stainless steel tube installed several centimeters below the probe tip. The air flow rate was adjusted so that single bubbles were intermittently released from the stainless steel tube. The bubbles were of uniform 5 mm diameter just before release and deformed as they traveled upward as shown in Figure 2.16. The high speed video camera and the IVFM data acquisition system were triggered simultaneously at time $t = 0$ ms. Figure 2.17 shows the voltage signal corresponding to the images shown in Figure 2.16. Correlation of numerous images and voltage signals like these confirmed that a large negative voltage spike is produced each time a bubble impacts the probe. The spike base width was defined as the time difference between the two crossings of a particular voltage level by the spike. The spike amplitude and spike base width were shown to be sensitive to the lateral location of the bubble at impact. Figure 2.18 shows a typical result for the non-dimensional mean spike amplitude and base width as a function of the displacement between the centerlines of the IVFM probe and the tube which released the bubbles. The mean spike amplitude was non-dimensionalized by V_{max}, the maximum spike amplitude; the mean spike base width was non-dimensionalized by ΔT_{max}, the maximum spike base width. A "direct" collision by a bubble produced a larger amplitude spike than a "glancing" collision since the entire bubble would disturb the field lines between the two electrodes instead of only a fraction

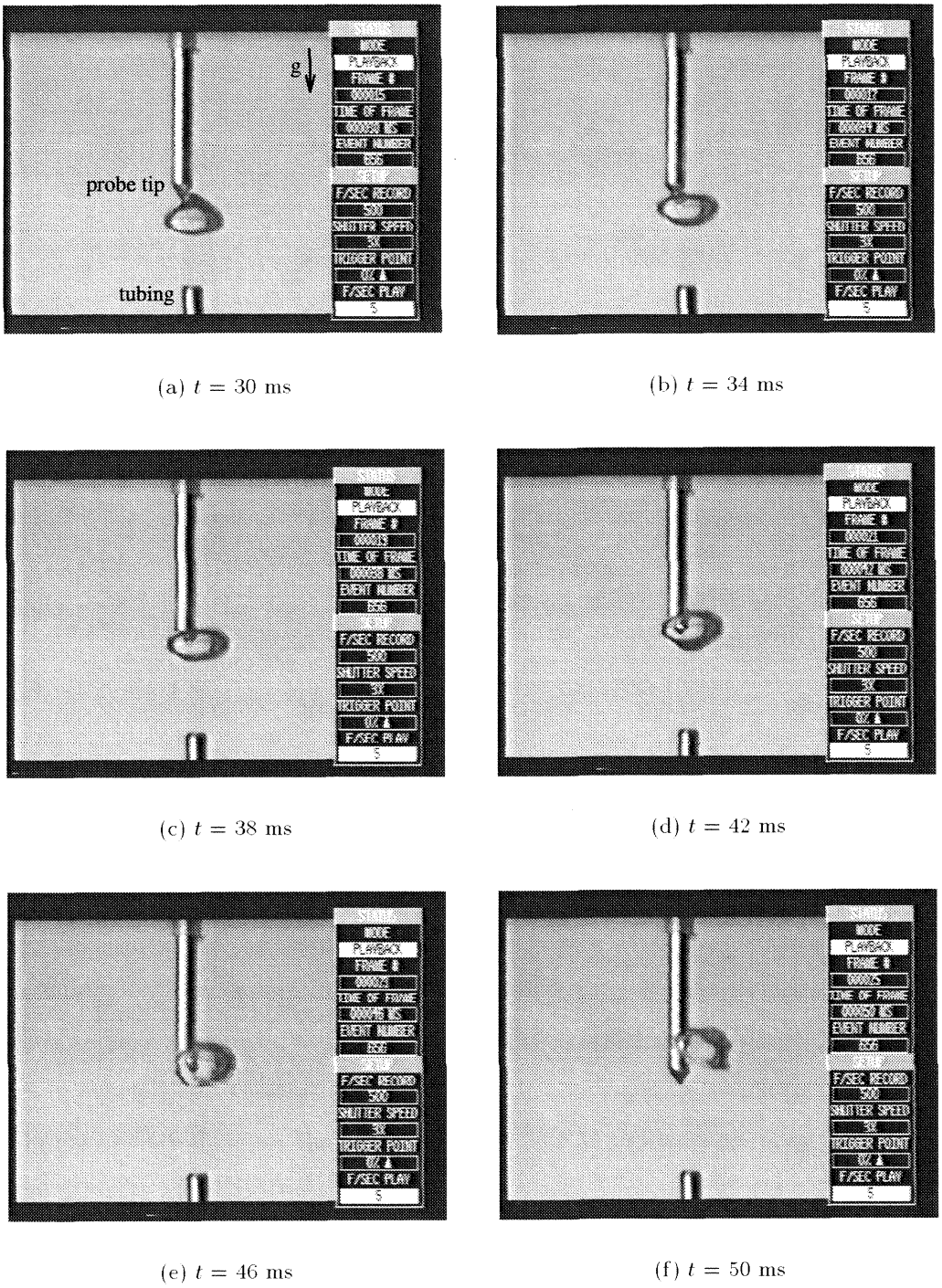

(a) $t = 30$ ms

(b) $t = 34$ ms

(c) $t = 38$ ms

(d) $t = 42$ ms

(e) $t = 46$ ms

(f) $t = 50$ ms

Figure 2.16 Frames from high speed video of single bubble tests. Once the bubbles detach from the tubing, they travel upwards with a velocity of 0.27 m/s, and impact the probe tip as oblate spheroids.

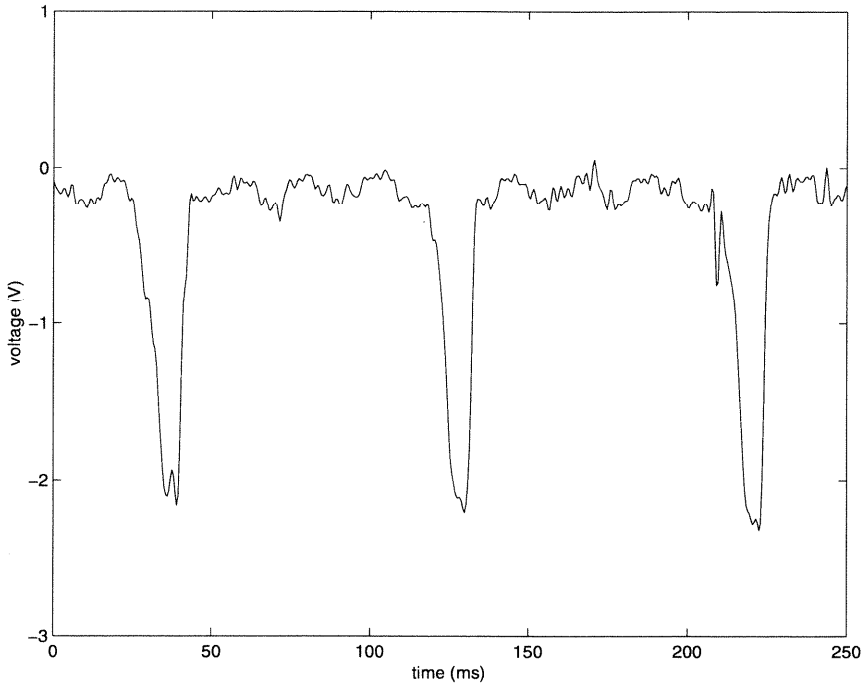

Figure 2.17 Typical IVFM signal from the single bubble tests; the frames from the corresponding high speed video are shown in Figure 2.16.

of a bubble. The spike base width corresponds to the residence time of the bubble on the probe; this time was longer for "direct" collisions. If the bubble is aligned with the probe, a greater volume of air disturbs the field lines, and since the bubbles move at a constant velocity, the duration of the disturbance increases.

The bubbly column facility described in section 2.1.4 was used to calibrate the IVFM. The IVFM signal was sampled at a rate of 2 kHz; a typical signal corresponding to $\alpha = 4.31\%$ is shown in Figure 2.19. The high speed videos again confirmed that each spike corresponded to the impact of a bubble on the probe tip. The IVFM signals were post-processed using software; a fourth order Butterworth filter with a cutoff frequency of 1 kHz (the Nyquist frequency) was used to eliminate any parts of the signal that had a non-physical origin. Forward and reverse filtering were used to prevent phase distortion, and the mean noise level was subtracted from each signal to compensate for any drift of the IVFM electronics.

The void fraction was calculated from the conditioned signals using a procedure based

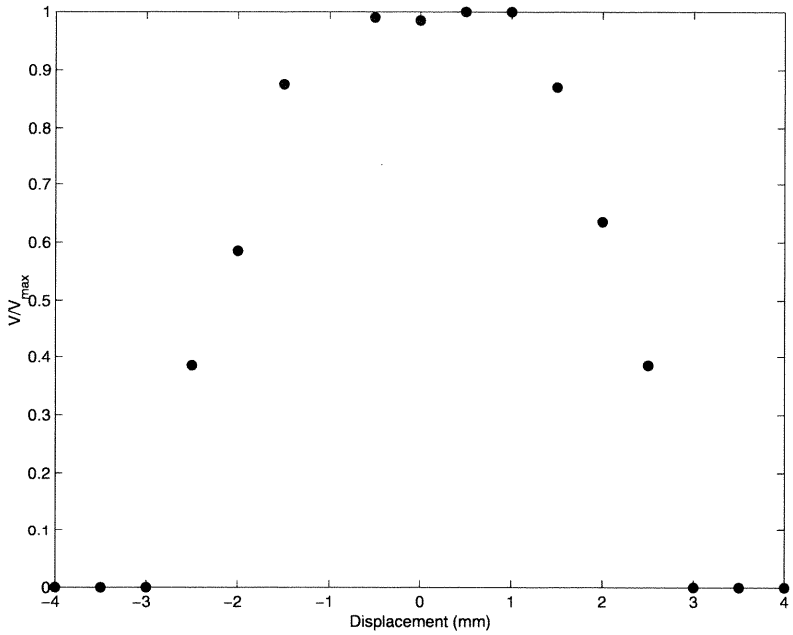

(a) Non-dimensional mean spike amplitude.

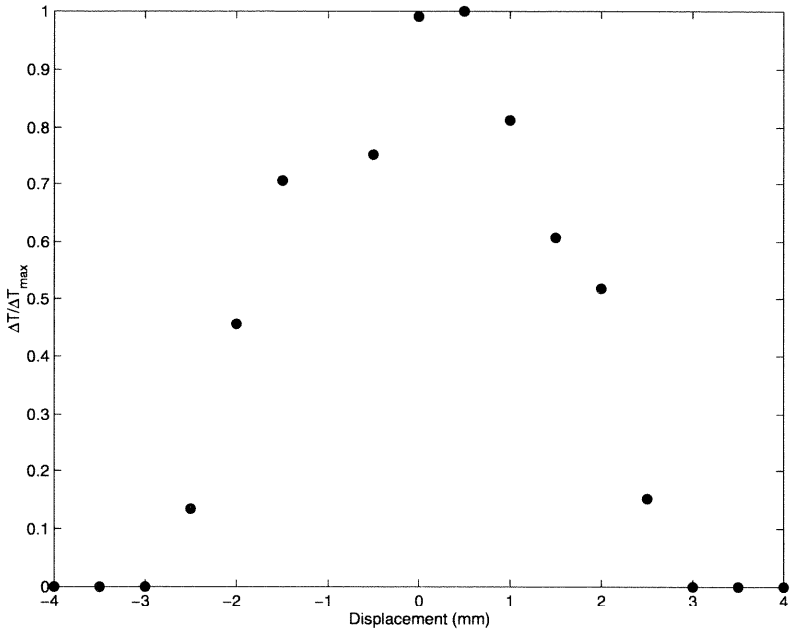

(b) Non-dimensional mean spike base width.

Figure 2.18 Non-dimensional mean spike amplitude and base width as a function of the displacement between the centerlines of the IVFM probe and the tube which released the bubbles.

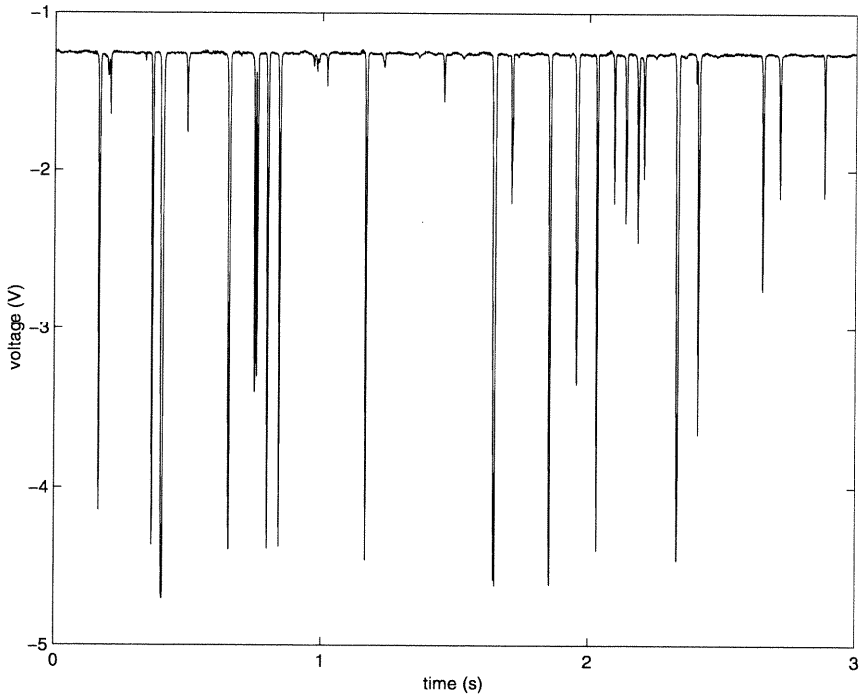

Figure 2.19 Typical IVFM signal from the calibration experiments. A voltage of -1.2 V occurs when no bubbles are touching the probe tip and each large negative spike corresponds to an air bubble passing by the probe tip.

on Eulerian time averaging methods for two phase flow mixtures suggested by Ishii [20]. This method assumes the interfacial region thickness, δ, to be very small. It further assumes that the interfaces are not stationary and do not occupy any reference location in space, x_o, for finite time intervals. In the following equations, the phase is designated by k where $k \in \{1, 2\}$. The state density function, M_k, is defined as

$$M_k(x, t) = 1$$

for a point, x, occupied by the k^{th} phase at time t. The time averaged phase density function, α_k, is defined as

$$\alpha_k(x_o, t_o) = \lim_{\delta \to 0} \frac{1}{\Delta t} \int_{[\Delta t]} M_k(x_o, t) dt \tag{2.6}$$

where t_o is a reference time and Δt is a fixed time interval large enough to smooth out local variations in flow properties. Physically, a_k represents a probability of finding the k^{th} phase; therefore, the time averaged phase density function is equivalent to the local void fraction of the k^{th} phase [20].

This theory assumes that for a given phase, say $k = 1$, the function $M_k(x,t)$ looks like that shown in Figure 2.20 where the phase alternates stepwise between phase 1 and phase 2. The IVFM signal is quite different from this, as can be seen in Figures 2.17 and 2.19, since all electronics have a finite frequency response. A single threshold method was used to extract the function $M_k(x,t)$ from the IVFM signals and is shown schematically in Figure 2.21. Specifically, for k =air, $M_k(x,t)$ was either 0 or 1 depending upon whether the signal exceeded a certain threshold or not. Similar procedures have been used by other researchers using conductivity probes to measure void fraction. For example, Teyssedou et al. [45] reported good agreement between void profiles obtained by their conductivity probe and an optical probe.

The calibration was repeated on four different days, and a typical calibration curve is shown in Figure 2.22. The void fractions were estimated using three different voltage thresholds, and a threshold of -0.75 V was shown to give the estimate closest to the measured value, especially at the lower void fractions. This threshold was then used for determining void fraction in the simulated bow wave experiments, even though in the simulated bow wave experiments the orientation of the probe was different and the bubbles were much smaller and more spherical in shape due to their more-or-less horizontal motion. The orientation of the probe was changed from vertical in the calibration to horizontal in the experiments to align the probe tip with the bubble velocity in the simulated bow wave experiments. In the calibration the probe tip pointed downward, and in the experiments the probe pointed upstream since the mean flow velocity (about 2 m/s) was much greater than typical bubble rise velocities (about 20 cm/s). Likewise, the difference in the size and shape of the bubbles did not diminish the relevance of the calibration since both flows contained many bubbles and the sampling times were long. The void fraction represents the likelihood of finding an air bubble on the tip of the probe at a given time and location, and this would be reflected in the void fraction signal irrespective of bubble size or shape.

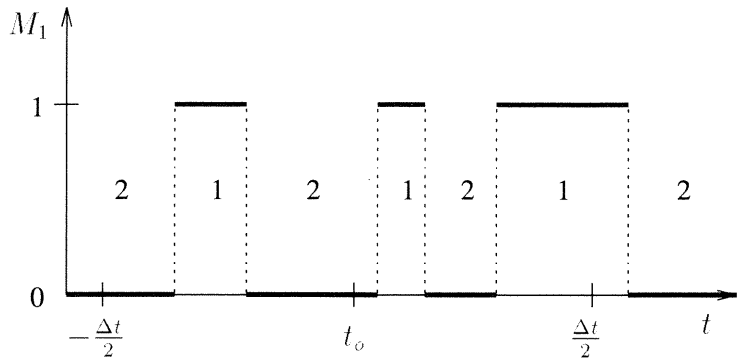

Figure 2.20 Theoretical state density function at a given location, x.

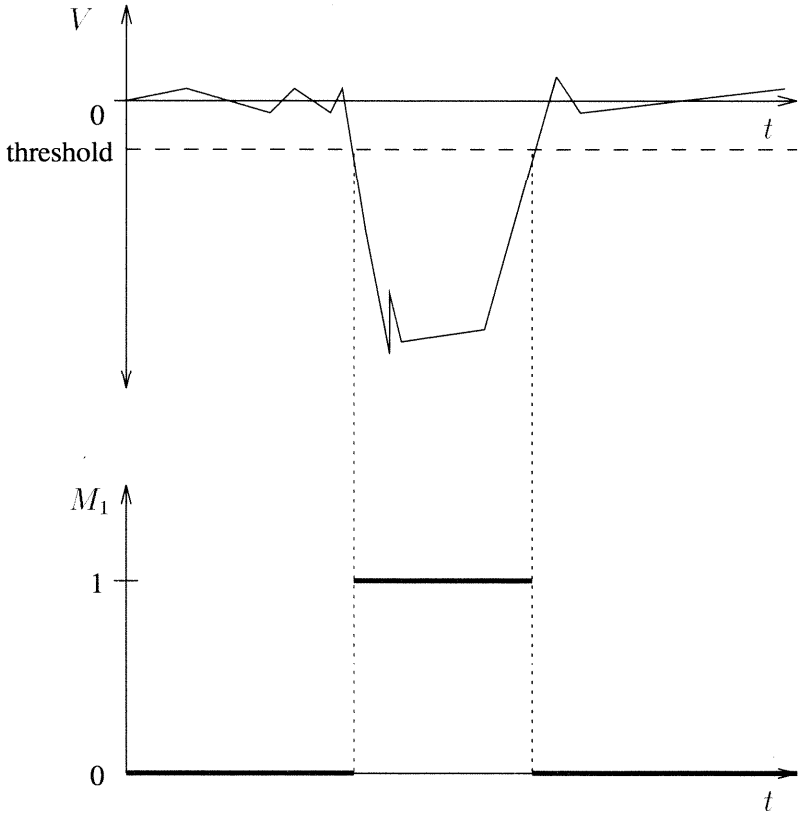

Figure 2.21 Schematic diagram of the construction of the function $M_k(x,t)$ from the IVFM voltage time history for a given location, x.

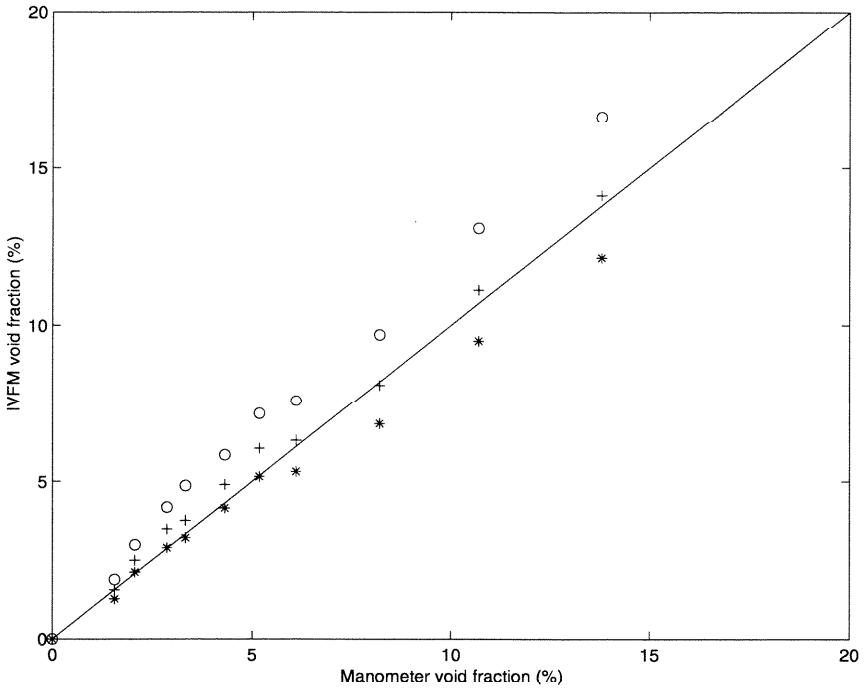

Figure 2.22 Calibration data for the IVFM from the bubbly column facility. The different groups of points were produced by processing the same data set using different thresholds; (∘) for threshold = -0.50 V, (+) for threshold = -0.75 V, and (∗) for threshold = -1.00 V. The linear curve fit for the data corresponding to threshold = -0.75 V has a slope of 1.00 and an intercept of 0.32.

2.2.4 Additional equipment associated with the IVFM

In the simulated bow wave experiments in the 40 m flume, the IVFM probe was mounted to the carriage described in section 2.2.1. Simultaneous high speed video was obtained with the IVFM signals using a camera which had a maximum framing rate of 500 fps, and a high intensity strobe light synchronized to the camera's framing rate illuminated the flow. A trigger box provided the TTL pulse used to synchronize the camera and the data acquisition card, and Figure 2.23 illustrates the components in the IVFM system. In some experiments, two high speed video cameras were used, and that configuration is detailed in Figure 2.24.

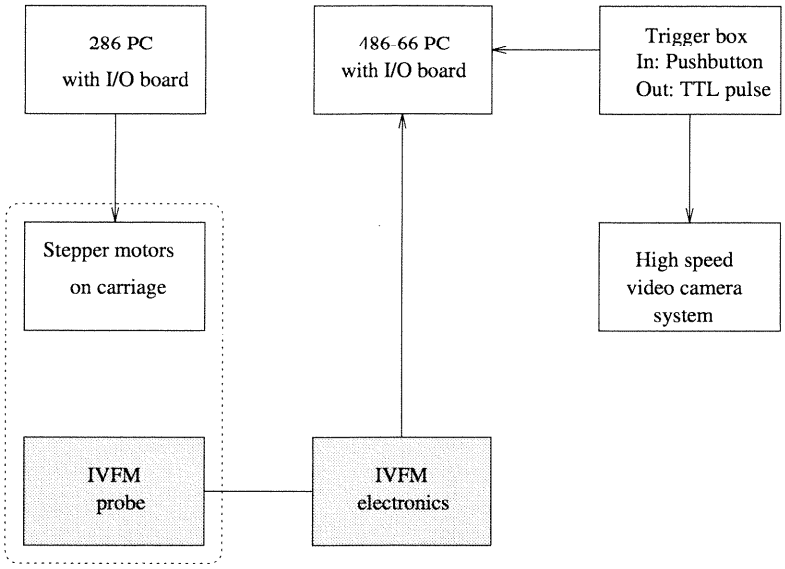

Figure 2.23 IVFM probe control and data acquisition system. The solid lines indicate electronic connections, and the dotted lines indicate mechanical connections.

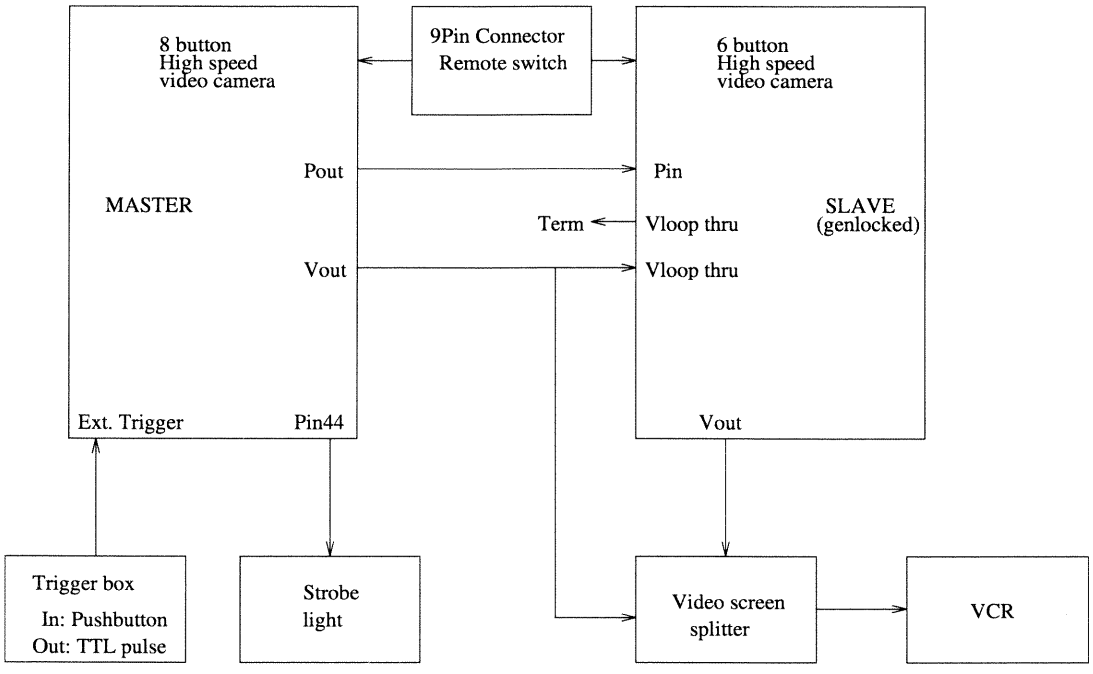

Figure 2.24 High speed video system.

Chapter 3

Theoretical Analyses of the Contact Line

One of the simplest ways to describe a bow wave is to specify its contact line on the hull surface. In this chapter we seek an analytical solution for the contact line and the form of other important functions (such as the velocity potential), and two different approaches are discussed. The first approach is an extension of Ogilvie's slender body theory [39] in which there is a finite depth equal to the draft. The second approach attempts to improve on this work, using perturbations of planar potential flow around a finite hull body to yield a three-dimensional solution. A section comparing the two approaches concludes this chapter.

3.1 Slender body analysis

3.1.1 Problem description

Figure 3.1 depicts the orientation of the slender body (ship) where the coordinate z is measured vertically upward, $z = 0$, being the ocean bottom and $z = h$ being the undisturbed free surface. Its shape is symmetric about the centerplane at $y = 0$, and it is described by the planforms, $b(x, z)$. The free stream velocity, U, is in the x-direction. The flow is assumed to be steady. Further simplifications are made by using order of magnitude arguments as in Ogilvie [39]. Let ϵ =beam/length and/or ϵ =draft/length so that as $\epsilon \to 0$, the ship approaches a line of length l. We denote the magnitude of the small quantity $\delta b/\delta x \approx \delta y/\delta x \approx$ beam/length by ϵ. Then, we choose to examine the region within $x = O(\epsilon^{1/2})$ and $r = \sqrt{y^2 + z^2} = O(\epsilon)$ which will define the near field of the flow close to

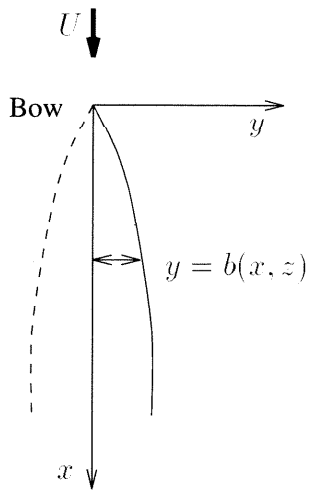

Figure 3.1 Planform view of a flow with velocity, U, impinging on the bow of a slender ship. The vertical coordinate, z, is perpendicular to the plane of the paper.

the bow. Using this, it follows that $\delta/\delta x = O(1/\epsilon^{1/2})$, $\delta/\delta y = O(1/\epsilon)$, and $\delta/\delta z = O(1/\epsilon)$.

We now make the standard potential flow assumptions (inviscid and incompressible) in order to find a velocity potential that satisfies the Laplace equation. The homogeneous three-dimensional Laplace equation,

$$\phi_{xx} + \phi_{yy} + \phi_{zz} = 0,$$

can be approximated by

$$\phi_{yy} + \phi_{zz} = 0$$

because $\phi_{xx} = O(\phi/\epsilon)$ and $\phi_{yy}, \phi_{zz} = O(\phi/\epsilon^2)$. The total velocity potential, ϕ_{total}, will take the form

$$\phi_{total} = Ux + \phi(x, y, z).$$

The four boundary conditions are:

1. The kinematic condition on the ocean bottom: $\phi_z = 0$ on $z = 0$.

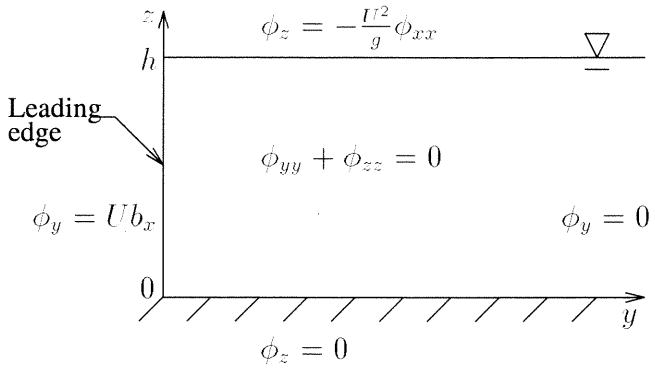

Figure 3.2 Semi-infinite strip domain with boundary conditions.

2. The approximate, linearized condition at the free surface:
   $\phi_z = -\frac{U^2}{g}\phi_{xx}$ on $z = h$.

3. The approximate, linearized kinematic condition at the hull surface:
   $\phi_y = Ub_x$ on $y = b(x, z)$.

4. The condition at infinity: $\phi_y = 0$ as $y \to \infty$,

and the details of their derivation may be found in Ogilvie [39]. The dynamic boundary condition at the free surface is

$$\zeta(x, y) = -\frac{U}{g}\phi_x|_{z=h}$$

and this is used after the solution has been obtained in order to find the free surface elevation.

We simplify the problem further by applying the hull boundary condition at $y = 0$ instead of at $y = b(x, z)$ which limits the validity of the results to slender ships. Figure 3.2 shows the semi-infinite strip within which we seek a solution.

3.1.2 Problem solution

We seek a separable solution of the form $\phi(x, y, z) = X(x)Y(y)Z(z)$. Substituting this into Laplace's equation yields

$$-\frac{Y''}{Y} = \frac{Z''}{Z} = \lambda^2$$

where λ is a real number and $\lambda^2 > 0$. Note that $\lambda^2 = 0$ implied that $\phi = f(x)$ which is impossible, and $\lambda^2 < 0$ implied that $\phi = 0$ which is also impossible. For the y-equation, $Y'' + \lambda^2 Y = 0$, the boundary conditions become:

$$Y'(0) = \frac{Ub_x}{X(x)Z(z)} \tag{3.1}$$

and

$$Y'(\infty) = 0. \tag{3.2}$$

For the z-equation, $Z'' - \lambda^2 Z = 0$, the boundary conditions become:

$$Z'(0) = 0 \tag{3.3}$$

and

$$\frac{Z'(h)}{Z(h)} = \frac{-U^2 X''(x)}{g X(x)}. \tag{3.4}$$

Using equations 3.2 and 3.3 with their separable boundary conditions gives $Y(y, \lambda) = Ae^{-\lambda y}$ and $Z(z, \lambda) = B\cos\lambda z$, where A and B are unknown coefficients. Thus

$$\phi(x, y, z) = \int X(x, \lambda)e^{-\lambda y}\cos(\lambda z)d\lambda.$$

To find the dispersion relation, we apply the dynamic free surface boundary condition,

equation 3.4, which yields,

$$X''(x) - \frac{g\lambda \tan(\lambda h)}{U^2} X(x) = 0 \tag{3.5}$$

where we will denote

$$\alpha^2 = \frac{g\lambda \tan(\lambda h)}{U^2}.$$

Note that the velocity of propagation, c, of small amplitude waves with wavelength λ on an ocean of depth, h, is

$$c = \left(\frac{g\lambda tanh(\frac{2\pi h}{\lambda})}{2\pi} \right)^{\frac{1}{2}};$$

therefore, α^2 is similar to a Froude number. Then the solution to equation 3.5 is

$$X(x,\lambda) = f_1(\lambda)e^{\alpha x} + f_2(\lambda)e^{-\alpha x}$$

where f_1 and f_2 are unknown functions. Substituting this into the expression for $\phi(x,y,z)$ yields

$$\phi(x,y,z) = \int (f_1(\lambda)e^{\alpha x} + f_2(\lambda)e^{-\alpha x})e^{-\lambda y}\cos(\lambda z)d\lambda,$$

and the free surface profile may be expressed as

$$\zeta(x,y) = -\int \frac{\alpha U}{g}(f_1(\lambda)e^{\alpha x} - f_2(\lambda)e^{-\alpha x})e^{-\lambda y}\cos(\lambda h)d\lambda.$$

To determine f_1 and f_2, the hull boundary condition, equation 3.1, is used yielding

$$-\int \lambda X(x,\lambda)\cos(\lambda z)d\lambda = Ub_x.$$

To solve this equation, we express Ub_x as a Fourier series in z as

$$Ub_x = U \int C(x,\lambda)\cos(\lambda z)d\lambda$$

where

$$C(x,\lambda) = \frac{2}{h}\int_0^h b_x \cos(\lambda z)dz.$$

Substituting this expression for Ub_x into the boundary condition, we have

$$-\lambda(f_1(\lambda)e^{\alpha x} + f_2(\lambda)e^{-\alpha x}) = UC(x,\lambda).$$

Since

$$C(x,\lambda) = -\frac{\lambda}{U}(f_1(\lambda)e^{\alpha x} + f_2(\lambda)e^{-\alpha x}),$$

then

$$Ub_x = -\int \lambda(f_1(\lambda)e^{\alpha x} + f_2(\lambda)e^{-\alpha x})cos(\lambda z)dz,$$

and

$$b(x,z) = -\int \frac{\lambda}{\alpha U}(f_1(\lambda)e^{\alpha x} + f_2(\lambda)e^{-\alpha x})\cos(\lambda z)d\lambda.$$

Furthermore, $b(0,z) = 0$; therefore, $f_1(\lambda) = -f_2(\lambda)$ and

$$b(x,z) = -\int \frac{\lambda}{\alpha U} f_1(\lambda)(e^{\alpha x} - e^{-\alpha x})\cos(\lambda z)d\lambda. \tag{3.6}$$

The free surface equation then becomes

$$\zeta(x,y) = -\int \frac{\alpha U}{g} f_1(\lambda)(e^{\alpha x} + e^{-\alpha x})e^{-\lambda y}\cos(\lambda h)d\lambda \tag{3.7}$$

and the contact line of the wave on the hull may be found by evaluating $\zeta(x,y)$ at $y = 0$.

3.1.3 Scaling implicit in the solution

We can extract information on the scaling of the free surface geometry from the above solution, and this is useful in examining the experimental measurements. To non-dimensionalize the preceding solution set

$$f_1{}^*(\lambda^*) = -\frac{\lambda^*}{\sqrt{gh^5\alpha^*}} f_1(\lambda) \tag{3.8}$$

and

$$\alpha^* = \sqrt{\lambda^* \tan \lambda^*}, \lambda^* = \lambda h, x^* = \frac{x}{\mathbf{F}h}, z^* = \frac{z}{h}.$$

Thus, the non-dimensional form of $b(x, z)$, $b^* = b/h$, is

$$b^*(x^*, z^*) = \int f_1^*(\lambda^*)(e^{\alpha^* x^*} - e^{-\alpha^* x^*}) \cos(\lambda^* z^*) d\lambda^*. \tag{3.9}$$

It follows that the non-dimensional contact line, $\zeta^*(x^*, 0)$, is given by

$$\zeta^*(x^*, 0) = \int f_1^*(\lambda^*)(e^{\alpha^* x^*} + e^{-\alpha^* x^*}) sin(\lambda^*) d\lambda^*. \tag{3.10}$$

It is clear from equations 3.9 and 3.10 that distances in the x-direction scale with the product of the Froude number and the depth, $\mathbf{F}h$, or $U\sqrt{h/g}$. Ogilvie [39] used the same factor, $\mathbf{F}h$, to non-dimensionalize length scales. In addition, equations 3.9 and 3.10 show that distances in the z-direction scale simply with h.

The method of solution is clearly to solve equation 3.9 for f_1^* since the shape of the ship hull, b^*, is known. Specifically, for fixed values of z^* it is possible to generate a family of curves, $f_1^*(x^*)$. However, since we are interested in the free surface shape, we only need $f_1^*(x^*)$ for $z^* = 1$. This function can be substituted into equation 3.10 to find the contact line, ζ^*. The non-dimensional contact line is only a function of x^*. It may be easily expanded into dimensional form by using f_1^* to solve for f_1 in equation 3.8 for a given draft, h. Then, f_1 may be substituted into equation 3.7, and by setting $y = 0$ we arrive at the dimensional form of the contact line, $\zeta(x, 0)$.

3.1.4 Numerical results

A computation based on this analysis predicted the shape of the free surface, $\zeta(x, y)$, for a given set of parameters, $U, h, b(x, z)$. Equation 3.9 can be rewritten using numerical, discrete $k = n\delta_k$ spectrum intervals as

$$b^*(x^*, z^*) = \sum_{n=0}^{\infty} f_1^*(n\delta_k)(e^{\alpha_n^* x^*} - e^{-\alpha_n^* x^*}) \cos(n\delta_k z^*), \tag{3.11}$$

where

$$\alpha_n^* = \sqrt{n\delta_k tan(n\delta_k)}$$

and

$$f_1^*(n\delta_k) = -\frac{n\delta_k}{\sqrt{gh^5}\alpha_n^*} f_1(\frac{n\delta_k}{h}).$$

The computer program takes the specified $b^*(x^*, z^*)$, a wedge shape for this case, and finds $f_1^*(n\delta_k)$ for fixed values of n and δ_k. Letting $n = 2$, we have

$$\begin{aligned} b^*(x^*, z^*) = \quad & f_1^*(1\delta_k)(e^{\alpha_1^* x^*} - e^{-\alpha_1^* x^*})cos(1\delta_k z^*) + \\ & f_1^*(2\delta_k)(e^{\alpha_2^* x^*} - e^{-\alpha_2^* x^*})cos(2\delta_k z^*). \end{aligned} \tag{3.12}$$

The value of δ_k as well as the ratio $f_1^*(2\delta_k)/f_1^*(\delta_k)$ are arbitrarily specified, and equation 3.12 is solved for f_1^*. This f_1^* is then used to find $\zeta^*(x^*, 0)$, the contact line. Equation 3.10 can similarly be rewritten using numerical, discrete $k = n\delta_k$ spectrum intervals as

$$\zeta^*(x^*, 0) = \sum_{n=0}^{\infty} f_1^*(n\delta_k)(e^{\alpha_n^* x^*} + e^{-\alpha_n^* x^*})sin(n\delta_k), \tag{3.13}$$

and equation 3.13 may be solved for $\zeta^*(x^*, 0)$.

The computation predicts a typical bow wave shape, but the amplitude of this wave is at least one order of magnitude smaller than the amplitudes observed in the stationary model experiments. Figure 3.3 shows the shape of the ship hull and the resulting bow

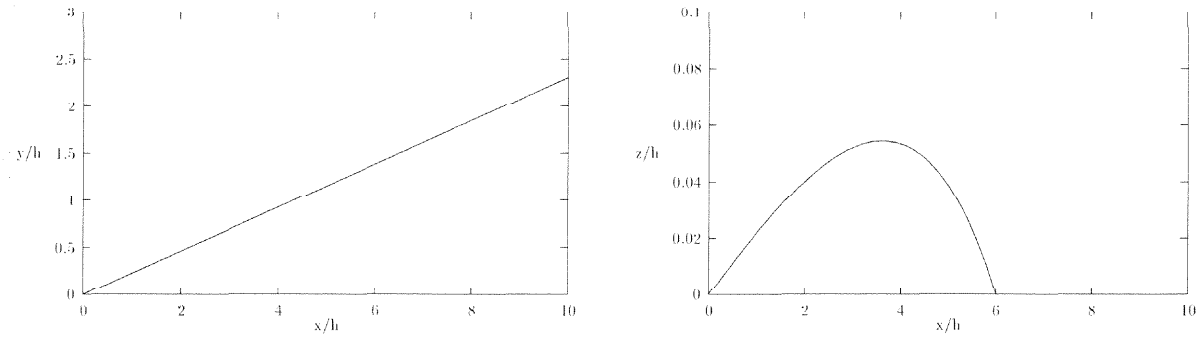

(a) Hull shape.

(b) Wave shape.

Figure 3.3 Typical numerical results.

wave predicted by this computer program for the following parameter set: $n = 2$, $\delta_k = 0.3$, $f_1^*(2\delta_k)/f_1^*(\delta_k) = -0.2$, $U = 2.46$ m/s, $d = 7.54$ cm, and $b/h = 0.231x/h$. The method is also excessively sensitive, i.e., small changes in the input parameter set cause widely varying results. The approximation of the hull boundary condition, the slender ship approximation, used in the analysis is probably responsible for most of the deficiencies of the numerical results. The equation $b/h = 0.231x/h$ describes a hull with a bow half angle of 25°, certainly not a very slender ship! We must conclude that there may be some flaw in the approximations used in the Ogilvie approach, in particular in the argument regarding the orders of magnitude for the various terms in the equation. Noblesse [37] arrives at the same conclusion in his study of bow flows.

3.2 Finite hull analysis

This section describes a second approach where an exact solution for planar potential flow around an appropriate finite body is found. This velocity potential, ϕ_1, is then perturbed by ϕ_2 to give the full three-dimensional solution, ϕ, where $\phi = \phi_1 + \phi_2$. Note that in this section Z represents a complex number, and β represents the bow half angle instead of θ.

3.2.1 Two-dimensional flow around a finite body

A body of an appropriate shape may be generated by a modified form of the Joukowski mapping. Figure 3.4 depicts the generation of a finite body which represents a two-dimensional ship hull. In a Z'' plane, the horizontal planform of the hull is described by

$$Z'' = ce^{i\theta''} \tag{3.14}$$

and the potential flow solution for the flow around this cylinder is given by

$$f_1(Z'') = U(Z'' + \frac{c^2}{Z''}) \tag{3.15}$$

assuming symmetry and no circulation. Then the body is mapped into a Z' plane using the translation

$$Z' = Z'' + c \tag{3.16}$$

or

$$Z' = c(1 + e^{i\theta''}). \tag{3.17}$$

Then, the potential flow solution is given by

$$f_1(Z') = U(Z' - c + \frac{c^2}{Z' - c}). \tag{3.18}$$

A second mapping into the Z plane is then used,

$$\frac{Z}{c} = Q(\frac{Z'}{c})^k + \frac{Z'}{c}, \tag{3.19}$$

to produce a finite body with a wedge-like leading edge as shown in Figure 3.4(c) where $k < 1$ and Q is a large, positive integer. Using the variables from the Z'' plane, this can be

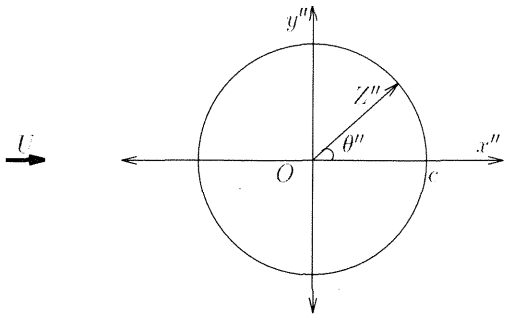

(a) Z'' plane, $Z'' = x'' + iy''$

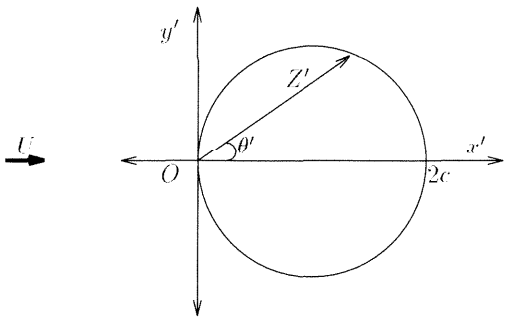

(b) Z' plane, $Z' = x' + iy'$

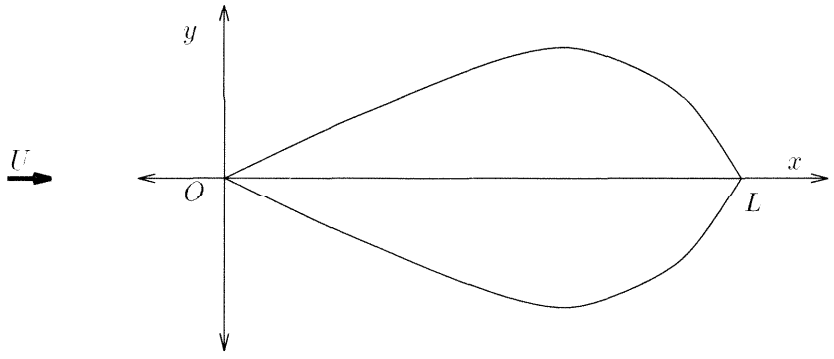

(c) Z plane, $Z = x + iy$

Figure 3.4 A circle in the Z'' plane is mapped into the Z' plane by translation and then mapped into the Z plane by distortion.

rewritten as

$$\frac{Z}{c} = Q(1 + \cos\theta'' + i\sin\theta'')^k + 1 + \cos\theta'' + i\sin\theta''. \tag{3.20}$$

The resulting body is similar to a symmetric, uncambered Joukowski airfoil with the trailing edge pointing upstream.

In order to relate k and the half angle of the wedge, consider the "bow" where $\theta'' \to \pi$. Let $\theta'' = \pi - \epsilon$, where ϵ is a small angle, and approximate $\cos(\pi - \epsilon) \approx -1 + \epsilon^2/2$ and $\sin(\pi - \epsilon) \approx \epsilon$. Substituting these approximations into the Z plane surface equation 3.20 yields

$$\frac{Z}{c} = Q\epsilon^k i^k (1 - \frac{\epsilon}{2}i)^k + \frac{\epsilon^2}{2} + i\epsilon. \tag{3.21}$$

Manipulating this result and separating its real and imaginary parts gives

$$\frac{x}{c} = Q\epsilon^k(\cos\frac{k\pi}{2} + \frac{k\epsilon}{2}\sin\frac{k\pi}{2}) + \frac{\epsilon^2}{2} \tag{3.22}$$

and

$$\frac{y}{c} = Q\epsilon^k(-\frac{k\epsilon}{2}\cos\frac{k\pi}{2} + \sin\frac{k\pi}{2}) + \epsilon. \tag{3.23}$$

Near the "bow," ϵ is small and so the wedge half angle

$$\beta = \frac{k\pi}{2}. \tag{3.24}$$

In order to normalize Z by a variable with physical meaning, we let $\theta'' = 0$ in equation 3.19. Then

$$\frac{Z}{c} = Q2^k + 2 \tag{3.25}$$

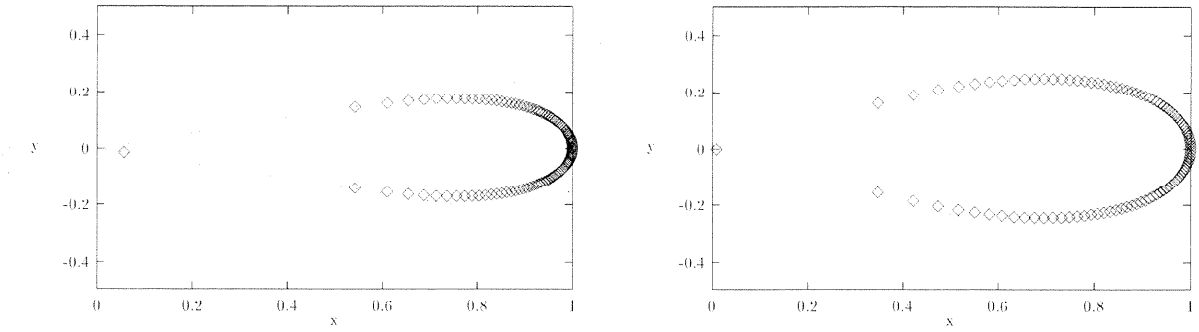

(a) $\beta = 15°, Q = 10000$

(b) $\beta = 25°, Q = 1000$

Figure 3.5 Examples of wedge-like finite bodies. The wedge with half angle β is shown by the dotted lines, and the set of points shows the finite body generated by the computer program.

which yields

$$\frac{L}{c} = Q2^k + 2 \tag{3.26}$$

and

$$\frac{Z}{L} = \frac{Q(1+\epsilon^{i\theta''})^k + 1 + \epsilon^{i\theta''}}{Q2^k + 2} \tag{3.27}$$

where L is the length of the body in the Z plane as shown in Figure 3.4(c).

A computer program was written to generate finite bodies corresponding to these equations for different values of β and Q. For $Q > 100$, the "bow" of these bodies appeared wedge-like. Two examples are shown in Figure 3.5. Therefore, parameter Q will have a value such that $Q \gg 1$.

The potential flow solution may be expressed in parametric form by combining equations 3.14, 3.15, 3.24, and 3.27. Letting $Z^* = Z/L$, $Z''^* = Z''/c$, and $-\pi < \theta'' < \pi$, we have

$$f_1(Z^*) = U(Z''^* + \frac{1}{Z''^*}) \tag{3.28}$$

where

$$Z^* = \frac{Q(1+Z''^*)^k + 1 + Z''^*}{Q2^k + 2}.$$

Furthermore, since $f_1(Z^*) = \phi_1 + i\psi_1$, the velocity potential function $\phi_1 = Re\{f_1(Z^*)\}$ and the stream function $\psi_1 = Im\{f_1(Z^*)\}$. The velocity components u and v may be obtained using $u = \partial\phi_1/\partial x$ and $v = \partial\phi_1/\partial y$ so that $df_1/dZ^* = u - iv$. First we express df_1/dZ^* using the chain rule as

$$\frac{df_1}{d(Z^*)} = \frac{df_1}{d(Z''^*)} \cdot \frac{d(Z''^*)}{d(Z^*)} \tag{3.29}$$

where

$$\frac{df_1}{d(Z''^*)} = U(1 - \frac{1}{(Z''^*)^2}) \tag{3.30}$$

and

$$\frac{d(Z''^*)}{d(Z^*)} = \frac{2^k + 2}{Qk(1+Z''^*)^{k-1} + 1}.$$

Representing $d(Z''^*)/d(Z^*)$ as the sum of an imaginary quantity, q_i, and a real quantity, q_r, so that

$$\frac{d(Z''^*)}{d(Z^*)} = q_r + iq_i,$$

we have

$$u - iv = \frac{U(1 - e^{-2i\theta''})(q_r - iq_i)}{q_r^2 + q_i^2} \tag{3.31}$$

from equation 3.29. Finally, the real and imaginary parts of equation 3.31 may be separated to yield

$$\frac{u}{U} = \frac{q_r(1 - \cos(2\theta'')) + q_i \sin(2\theta'')}{q_r^2 + q_i^2}$$

and

$$\frac{v}{U} = \frac{q_i(1-\cos(2\theta'')) - q_r \sin(2\theta'')}{q_r^2 + q_i^2}.$$

3.2.2 Perturbation analysis

In this subsection, we consider the velocity potential function in the three-dimensional flow, ϕ. The flow has depth h and $z = 0$ is the location of the undisturbed free surface and $z = -h$ is the location of the bottom. The velocity potential function may be found by adding a three-dimensional perturbation, ϕ_2, to the two dimensional velocity potential so that $\phi = \phi_1 + \phi_2$. Of course, we must have $\nabla^2\phi_2 = 0$, with boundary conditions for the bottom and for the free surface. The boundary condition for the bottom, $z = -h$, is simply

$$\left(\frac{\partial \phi_2}{\partial z}\right)_{z=-h} = 0. \tag{3.32}$$

If the free surface is at $z = \zeta(x, y)$, then the simplified kinematic and dynamic free surface boundary conditions are

$$\frac{\partial \phi_2}{\partial z} \approx \frac{\partial h}{\partial x}\left(\frac{\partial \phi_1}{\partial x}\right)_{z=\zeta} + \frac{\partial h}{\partial y}\left(\frac{\partial \phi_1}{\partial y}\right)_{z=\zeta} \tag{3.33}$$

and

$$\frac{g\zeta}{U^2} \approx \frac{1}{2} - \frac{1}{2U^2}\left(\left(\frac{\partial \phi}{\partial x}\right)^2_{z=\zeta} + \left(\frac{\partial \phi}{\partial y}\right)^2_{z=\zeta} + \left(\frac{\partial \phi}{\partial z}\right)^2_{z=\zeta}\right) \tag{3.34}$$

where the flow is assumed to be steady. Since $\phi = \phi_1 + \phi_2$, equation 3.34 is

$$\zeta^* \approx \frac{1}{2U^2}\left(U^2 - \left(\frac{\partial \phi_1}{\partial x}^2 + 2\frac{\partial \phi_1}{\partial x}\frac{\partial \phi_2}{\partial x} + \frac{\partial \phi_2}{\partial x}^2\right) - \left(\frac{\partial \phi_1}{\partial y}^2 + 2\frac{\partial \phi_1}{\partial y}\frac{\partial \phi_2}{\partial y} + \frac{\partial \phi_2}{\partial y}^2\right) - \frac{\partial \phi_2}{\partial z}^2\right) \tag{3.35}$$

where $\zeta^* = (g/U^2)\zeta$, the non-dimensional free surface height. We can use equation 3.35 to solve for ζ^*, and by evaluating ζ^* on $\theta = \beta$, the bow half angle, we can arrive at the contact line. Let $\zeta^* = \zeta_1^* + \zeta_2^*$ where the higher order perturbation terms are assumed to be small

and

$$\zeta_1^* = \frac{1}{2U^2}\left(U^2 - \frac{\partial\phi_1}{\partial x}^2 - \frac{\partial\phi_1}{\partial y}^2\right) \tag{3.36}$$

and

$$\zeta_2^* = -\frac{1}{U^2}\left(\frac{\partial\phi_1}{\partial x}\frac{\partial\phi_2}{\partial x} + \frac{\partial\phi_1}{\partial y}\frac{\partial\phi_2}{\partial y}\right). \tag{3.37}$$

This assumption is valid for most of the bow wave profile.

First we seek a solution for ζ_1^*, a straight-forward process since the two-dimensional flow is solved. The terms on the right-hand side of equation 3.36 are written in terms of f_1, its complex conjugate $\bar{f}_1$, and Z and $\bar{Z}$ as

$$\zeta_1^* = \frac{1}{2} - \frac{1}{2U^2}\frac{\partial f_1}{\partial Z}\frac{\partial \bar{f}_1}{\partial \bar{Z}} \tag{3.38}$$

where $\bar{Z}$ is the complex conjugate of Z. Recall the two-dimensional flow solution from equation 3.15, namely

$$f_1(\eta) = U\left(\eta - 1 + \frac{1}{\eta - 1}\right) \tag{3.39}$$

where $\eta = 1 + e^{i\theta''}$. Further, $f_1(\eta)$ can be approximated by a series expansion so that

$$f_1 \approx U(-2 - \eta^2 + \cdots)$$

and

$$\frac{\partial f_1}{\partial \eta} \approx -2U\eta + \cdots \tag{3.40}$$

since near the bow leading edge, η is small. Also recall equation 3.27, the finite body solution. It may also be written in terms of η such that

$$\frac{Z}{L} = \alpha_1\eta^k + \alpha_2\eta$$

where $\alpha_1 = Q/(Q2^k + 2)$ and $\alpha_2 = 1/(Q2^k + 2)$. But since Q is large, $\alpha_1\eta^k \gg \alpha_2\eta$, and then

$$\frac{Z}{L} = \alpha_1\eta^k + \cdots$$

and

$$\frac{\partial Z}{\partial \eta} \approx L\alpha_1 k\eta^{k-1} + \cdots . \tag{3.41}$$

Using equations 3.40 and 3.41 and the chain rule, we have

$$\frac{\partial f_1}{\partial Z} = -\frac{2U}{Lk\alpha_1^{2/k}} Z^{2/k-1} \tag{3.42}$$

Substitution of the expression for $\partial f_1/\partial Z$ in equation 3.42 into equation 3.38 allows us to solve for ζ_1^* which is

$$\zeta_1^* = \frac{1}{2} - \frac{2}{L^2k^2\alpha_1^{4/k}} Z^{2/k-1}\bar{Z}^{2/k-1}$$

or

$$\zeta_1^* = \frac{1}{2} - \frac{2}{L^2k^2\alpha_1^{4/k}} r^{4/k-2} \tag{3.43}$$

where $Z = re^{i\theta}$.

We now seek a solution for ζ_2^* which is more complicated since f_2 is unknown. As a first step, we examine the kinematic free surface boundary condition and the bottom boundary condition and guess that

$$\frac{\partial^2\phi_2}{\partial z^2} = \frac{1}{h}\left(\frac{\partial\phi_2}{\partial z}\right)_{z=\zeta}$$

so that the field equation for ϕ_2 becomes

$$\frac{\partial^2\phi_2}{\partial x^2} + \frac{\partial^2\phi_2}{\partial y^2} = \frac{1}{h}\left(\frac{\partial\phi_2}{\partial z}\right)_{z=\zeta} \tag{3.44}$$

where the right-hand side is a function only of x and y. We now continue to use the free surface kinematic condition to cast the right-hand side of equation 3.44 in terms of known quantities, and after significant algebraic manipulation we have

$$\frac{\partial^2 \phi_2}{\partial x^2} + \frac{\partial^2 \phi_2}{\partial y^2} = R\epsilon \left\{ \frac{1}{gh} \left(\frac{\partial f_1}{\partial Z} \right)^2 \frac{\partial^2 \bar{f}_1}{\partial \bar{Z}^2} \right\}.$$

Furthermore, since $f_2 = fcn(Z, \bar{Z})$, the field equation for f_2 can be written as

$$4 \frac{\partial^2 f_2}{\partial Z \partial \bar{Z}} = \frac{1}{gh} \left(\frac{\partial f_1}{\partial Z} \right)^2 \frac{\partial^2 \bar{f}_1}{\partial \bar{Z}^2}$$

and integrated with respect to $\partial \bar{Z}$ to give

$$\frac{\partial f_2}{\partial Z} = \frac{1}{4gh} \left(\frac{\partial f_1}{\partial Z} \right)^2 \frac{\partial \bar{f}_1}{\partial \bar{Z}} + fcn(Z). \tag{3.45}$$

Using the expression for $\partial f_1 / \partial z$ in equation 3.42 and integrating equation 3.45 with respect to $\bar{Z}$, we have

$$f_2 = -\frac{2U^3 Z^{4/k-1} \bar{Z}^{2/k-1}}{ghk^2(4-k)\alpha_1^{6/k} L^3} + fcn(Z) + fcn(\bar{Z}).$$

Since f_2 is now known, we begin to evaluate the terms on the right-hand side of equation 3.37 to arrive at ζ_2^*. Using $\phi_1 = (f_1 + \bar{f}_1)/2$ and $\phi_2 = (f_2 + \bar{f}_2)/2$, we rewrite equation 3.10 as

$$\zeta_2^* = -\frac{1}{U^2} \left[R\epsilon \left\{ \frac{\partial f_1}{\partial Z} \left(\frac{\partial f_2}{\partial Z} + \frac{\partial \bar{f}_2}{\partial Z} \right) \right\} \right]. \tag{3.46}$$

Finally, using $Z = re^{i\theta}$ and the expressions for $\partial f_1 / \partial Z$ and $\partial f_2 / \partial Z$ from equations 3.42 and 3.45, we have

$$\zeta_2^* = -\frac{4U^2}{gh(4-k)\alpha_1^{8/k} k^4} R\epsilon \left\{ r^{6/k-4} \epsilon^{i\theta(2/k-2)} r^{2/k} \left[(4-k)e^{2i\theta/k} + (2-k)e^{-2i\theta/k} \right] \right\}. \tag{3.47}$$

Recall that $\zeta^* = \zeta_1^* + \zeta_2^*$, and using the expressions for ζ_1^* and ζ_2^* in equations 3.43 and 3.47,

the total free surface height, ζ^*, is

$$\begin{aligned}\zeta^* &= \frac{1}{2} - \frac{2}{L^2k^2\alpha_1^{4/k}} r^{4/k-2} - \frac{4U^2}{gh(4-k)\alpha_1^{8/k}k^4} \\ &\quad Re\left\{ r^{6/k-4} e^{i\theta(2/k-2)} r^{2/k} \left[(4-k)e^{2i\theta/k} + (2-k)e^{-2i\theta/k} \right] \right\}. \end{aligned} \tag{3.48}$$

Evaluating the expression in equation 3.48 at $\theta = \pm\beta$ and using equation 3.24 yields the non-dimensional free surface height along the ship hull (contact line), namely

$$(\zeta^*)_{\theta=\pm\beta} = \frac{1}{2} - \frac{2}{L^2k^2\alpha_1^{4/k}} r^{4/k-2} - \frac{4\mathbf{F}^2}{(4-k)\alpha_1^{8/k}k^4}(6-2k)\cos 2\beta, \tag{3.49}$$

a power series in $\mathbf{F}^2$ where $\mathbf{F} < 1$ for the series to converge. Multiplying both sides of equation 3.49 by g/U^2 and examining the order of the flow parameters in the terms gives

$$(\zeta)_{\theta=\pm\beta} = O(\mathbf{F}^2 h) + O(\mathbf{F}^4 h).$$

Even though this solution involved numerous simplifications and is only valid near the bow leading edge for low $\mathbf{F}$, it suggests a complicated non-linear relationship between the free surface height and the flow parameters $\mathbf{F}$ and h, and the geometric parameter β.

3.3 Comparison of the theoretical analyses

The first analytical approach presented in this chapter was simply an extension of Ogilvie's work in which a finite depth equal to the draft was considered. The main approximation in this analysis was inherent in the slender body theory. Specifically, the hull boundary condition was applied at $y = 0$ instead of at $y = b(x, z)$, in a sense linearizing in the y-direction. The numerical results based on this analysis were poor; however, this was not too surprising since Ogilvie's analysis also gave poor agreement with his experiments. Other researchers, including Noblesse [37], use slender body theory and report similar difficulties predicting bow wave shapes.

The main approximation of the second analytical approach was that the perturbation was small, essentially linearizing in the z-direction. The form of the perturbation was also

assumed; however, many forms of $\partial^2\phi/\partial z^2$ would satisfy the kinematic free surface boundary condition and the bottom boundary condition. If a numerical calculation was performed based on this analysis, an iterative process could be used to find the perturbation form yielding the best agreement with the experimental data. Then, it would be worthwhile to refine the predicted free surface height, ζ, by evaluating the higher order perturbation terms such as $\partial\phi_2^2/\partial^2 x$ and $\partial\phi_2^2/\partial^2 y$ in equation 3.35. However, the second approach clearly leads to an expansion in the Froude number $\mathbf{F}$ and this requires $\mathbf{F} < 1$ for the expansion to converge. Since we are primarily concerned here with flow in which $\mathbf{F} > 1$, this approach is unlikely to succeed.

The failure of these two analytical approaches demonstrates that bow flows are highly non-linear since linearizing in either direction yields unacceptable results. We are forced to conclude that there appears, at present, to be no satisfactory analytical approach to the bow wave flow.

Numerical solutions of this flow have been more successful. Studies such as those by Ni [36] and Jensen [21] used the hull boundary condition and the non-linear free surface conditions in their exact form in their computations, but the discrepancies between theory and experiment remained. The experimental free surface data are almost a factor of two greater than the calculations. In a later paper, Noblesse et al. [38] discussed whether the physical assumptions or numerical methods were responsible for this discrepancy. His analytical expressions and examination of experimentally measured wave profiles showed that at the bow the flow speed is nearly equal to the ship speed, but directed vertically upward. At other points along the wave profile, the velocity of the flow disturbance due to the hull is small, and he concluded that non-linearities are very important only for small regions near the bow and that fine discretization is required in these regions for all numerical calculations. The "2D + t", or two dimensions plus time, method can give the high resolution required, and it has been implemented by other researchers with some success. This method uses the exact boundary conditions and a change of variables, $x - Ut$, so that the equations are in terms of y, z, and t. The equations then become similar to those for a two-dimensional wavemaker, and numerous studies of these flows can be found such as those by Chapman [14]. Çalişal and Chan [9] used the "2D + t" and the boundary

integral methods to solve bow flows for wedge models. When compared to experimental data, their computations slightly overpredict the free surface heights, and the discrepancy increases with increasing wedge angle. However, it is able to produce the over-turning of the bow wave and trace the plunging wave jet. Tulin and Wu [47] used this technique for flows around wedges and "Wigley-like" hulls, and found it to be most effective for fine ships moving at high speeds like destroyers.

Chapter 4

Experimental Measurements of the Free Surface

Bow waves are highly three-dimensional with complex free surface shapes; therefore, it is necessary to describe them in several ways. This chapter presents a qualitative description of the waves followed by experimental measurements. First, the contact line of the bow wave on the model or plate surface is discussed. Second, the bow wave profile, the profile of the maximum free surface height of the wave, is presented. Third, cross sections and frontal aspects of the wave are given to show the plunging wave jet. The presentation of these measurements is then followed by a discussion on the scaling of the wave with the flow parameters and geometric parameters. Finally, observations and measurements of surface disturbances observed on the plunging wave jet are presented and discussed.

4.1 Bow wave observations

The larger scale stationary model experiments were the first set of experiments performed. In these experiments, as the flow accelerated to the test velocity, the wave generated by the deflecting plate transitioned through three distinct flow regimes. The first flow regime was for sub-critical conditions ($\mathbf{F} < 1$); the model created a disturbance extending 5 to 10 cm upstream of the leading edge. The second flow regime was for near critical conditions ($\mathbf{F} \approx 1$), and a wave similar to an oblique hydraulic jump was observed. The third flow regime was for super-critical conditions ($\mathbf{F} > 1$) and a wave similar to a bow wave resulted. In each case, the free surface was unsteady and turbulent on and behind the wave front. These flow regimes were also observed later in the smaller scale stationary model and the

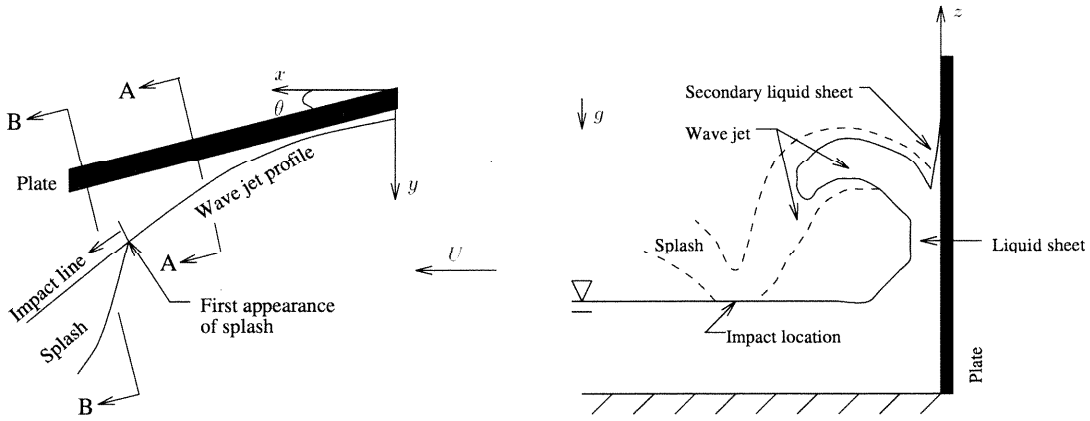

(a) Top view of the wave created by the deflecting plate.

(b) Cross-sectional views A (—) and B (--) of the wave. The horizontal coordinate along the deflecting plate, r, is perpendicular to the plane of the paper.

Figure 4.1 Schematic diagram of the main features of the wave.

towed model experiments, but they were particular to models with half angles of about 15° to 25°. Miyata [34] made observations of similar waves in towed model experiments and reported that models with a half angle greater than 45° would not produce oblique hydraulic jumps or bow waves.

Flow visualization studies were performed in the larger scale stationary model experiments to define the main features of the wave in the super-critical flow regime. Syringes with cannulae were used to inject kriegrocine dye into the flow and a video camera, high speed movie camera, and a Nikon N90AF camera were all used to record the results. Figure 4.1 shows an exaggerated schematic of the bow wave with the key features labeled. The top view of the test section is shown in Figure 4.1(a); the planform profile of the wave jet, the impact line, and the splash region are indicated. These features are clarified in the cross-sectional views presented in Figure 4.1(b).

The impingement of the flow on the deflecting plate causes its momentum to change direction. In fact, Noblesse [38] showed that at the bow of a wall-sided hull, the velocity will

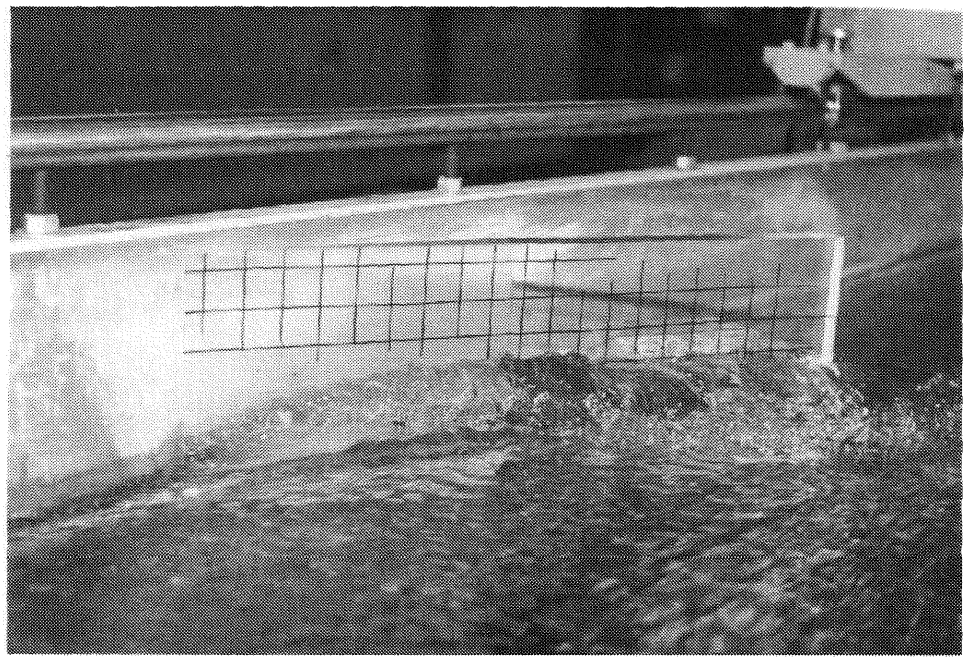

(a) Leading edge against the flume wall.

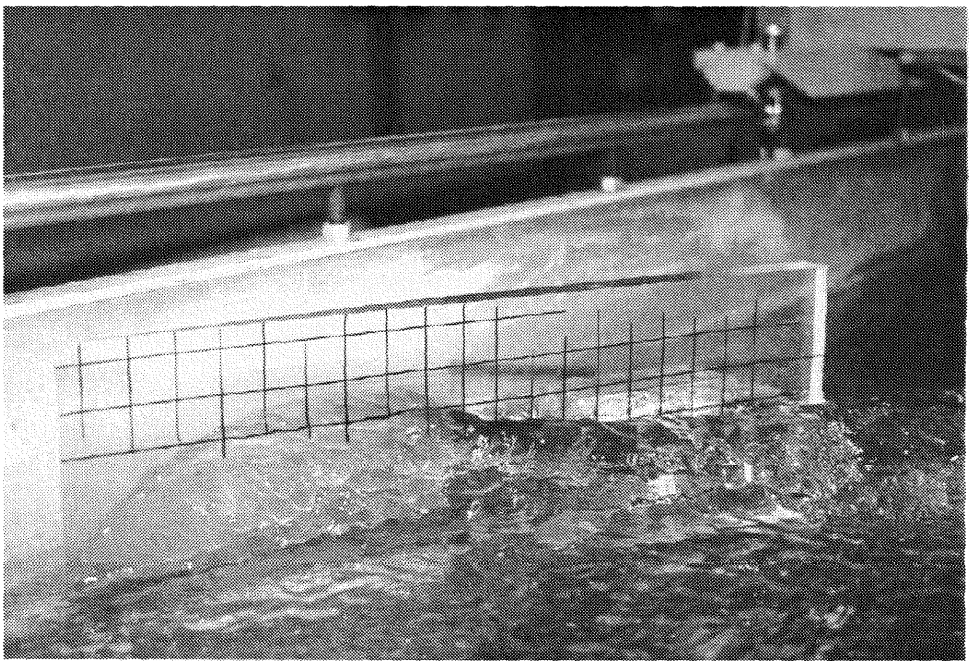

(b) Leading edge displaced 2.5 cm away from the flume wall.

Figure 4.2 Photographs of the bow waves in the 2.6 m flume. The grid on the deflecting plate is 2 cm by 2 cm, and $\theta = 25°$, $\phi = 0°$, $U = 1.58$ m/s, $d = 1.21$ cm, and $\mathbf{F} = 4.59$.

have a component in the vertical direction only. Vertical velocity at the bow is necessary for bow wave formation. Note the difference in the photographs presented in Figure 4.2(a) and (b). In Figure 4.2(a) the deflecting plate is against the flume wall and "turns" the flow creating a wave similar to an oblique hydraulic jump. In Figure 4.2(b) the deflecting plate is displaced from the flume wall and the velocity changes as described above. The vertical velocity at the bow creates a liquid sheet which rides up on the plate before it separates. As the flow moves away from the plate, it continues in the upward direction so that the maximum height of the bow wave is located a few centimeters away from the deflecting plate. A thin secondary liquid sheet is observed on the wall in the experiments as shown in Figure 4.1(b). The water in this secondary liquid sheet seemed to result from the unsteadiness of the contact line on the plate.

Once the wave has reached its maximum height, gravity causes it to plunge back towards the free surface as shown in cross section B-B in Figure 4.1(b). Inspection of the breaking wave jet reveals almost equally spaced striations along the surface oriented perpendicular to the wave crest. These will be discussed further in section 4.7. The edge of the breaking wave is irregular and appears to be comprised of individual jets or strings of droplets as can be seen in Figure 2.4. It impacts the free surface along a line called the impact line in Figure 4.1(a).

After the wave jet impacts the free surface, a splash region is formed as seen in Figure 2.4 and shown schematically in Figure 4.1. Although the majority of the splash is formed by the wave jet "bouncing" off the undisturbed free surface, the flow visualization tests showed that some of the freestream flow is deflected and also enters the splash region. The splash region has a limited upstream extent as sketched in Figure 4.1(a).

The waves generated in the towed model experiments were similar to the waves generated in the stationary model experiments even though the stationary model experiments had a much smaller depth and the model extended to the bottom of the flume. The other difference between the experiments was simply a Galilean transformation, and this was not expected to affect the results. The similarity of the two experiments will be shown quantitatively in section 4.4. One difference, however, was that the waves created in towed model experiments had a glassier appearance and a steadier contact line since the water in the towing tank was

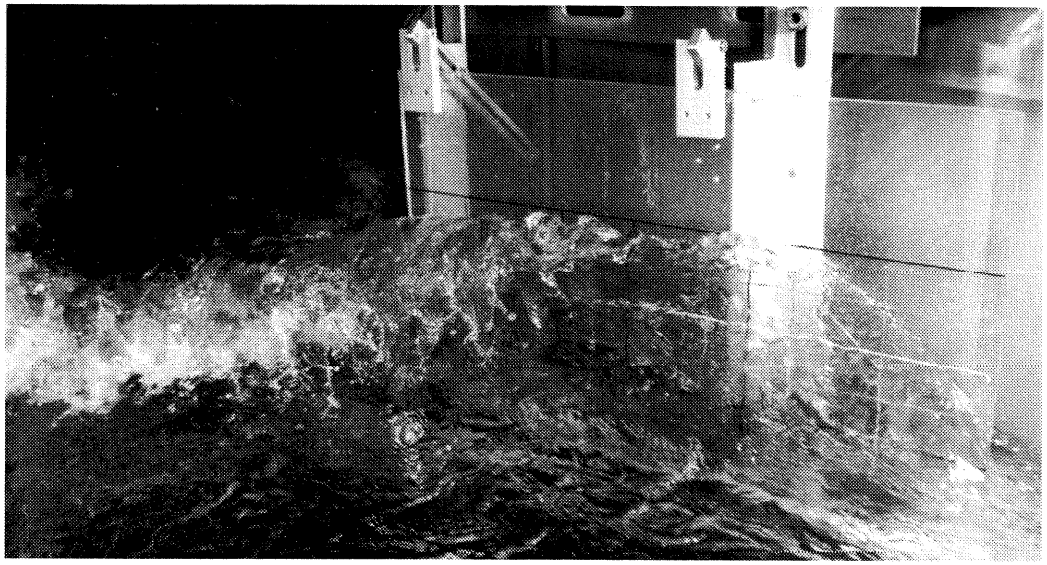

(a) Stationary model experiment in 40 m flume.

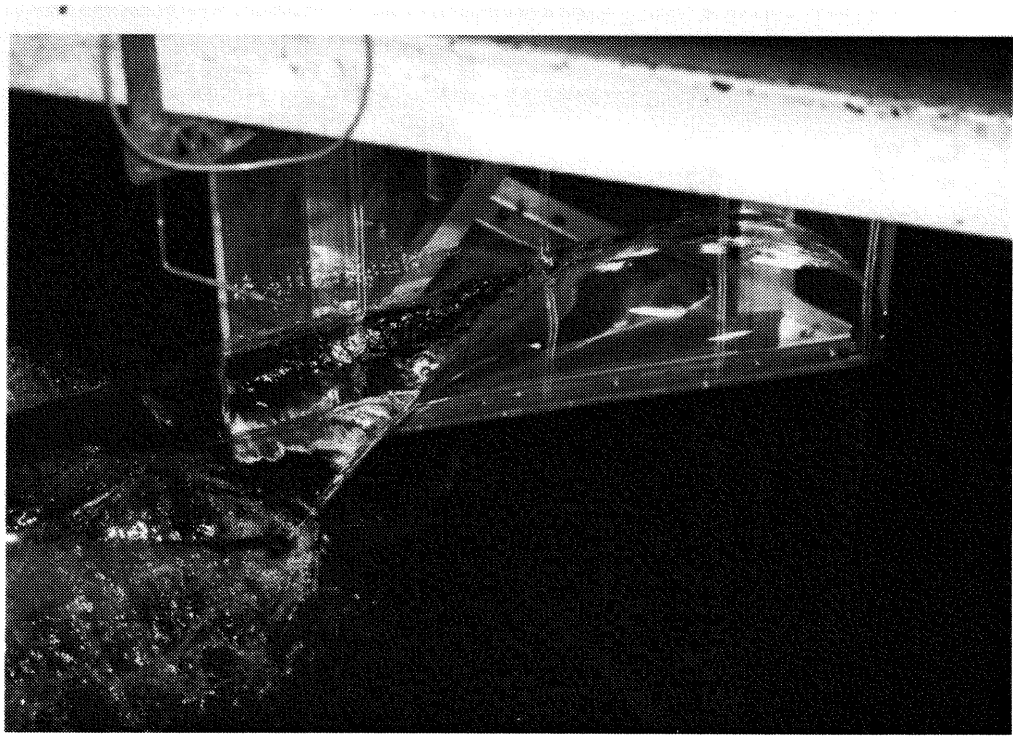

(b) Towed model experiment at Hydronautics Research.

Figure 4.3 Photographs of the bow waves for conditions with similar velocity and draft.

Run	Experiment	θ (°)	U (m/s)	d (cm)	**F**
1s	Smaller scale	13.2	1.97	0.95	6.46
2s	Smaller scale	13.2	1.11	1.35	3.06
3s	Smaller scale	13.2	1.07	1.35	2.93
4s	Smaller scale	13.2	0.94	1.35	2.57
5s	Smaller scale	26.3	1.11	1.35	3.06
6s	Smaller scale	26.3	1.07	1.35	2.93
1l	Larger scale	13.4	2.44	6.66	3.01
2l	Larger scale	13.4	2.43	7.55	2.81
3l	Larger scale	13.4	2.46	9.21	2.59
4l	Larger scale	26.6	2.61	6.45	3.29
5l	Larger scale	26.6	2.40	7.62	2.77
6l	Larger scale	26.6	2.46	9.32	2.57

Table 4.1 Stationary model contact line experimental conditions.

quiescent. In the stationary model experiments, the surface of the waves was visibly rough despite efforts to "smooth" the free surface upstream of the test section. Photographs of the waves from both the larger scale stationary model experiments and the towed wedge experiments demonstrate these points and have been included as Figure 4.3.

4.2 Contact line results

The contact line was measured in both the smaller and larger scale stationary model experiments using the free surface probe described in section 2.2.1. Figure 4.4(a) presents the contact line data from the smaller scale stationary model experiments, and Figure 4.4(b) presents a summary of the contact line data from the larger scale stationary model experiments. Table 4.1 lists the corresponding flow conditions. In both Figure 4.4(a) and 4.4(b) the leading edge of the deflecting plate was at $r = 0$ and $z = 0$ was the location of the undisturbed free surface.

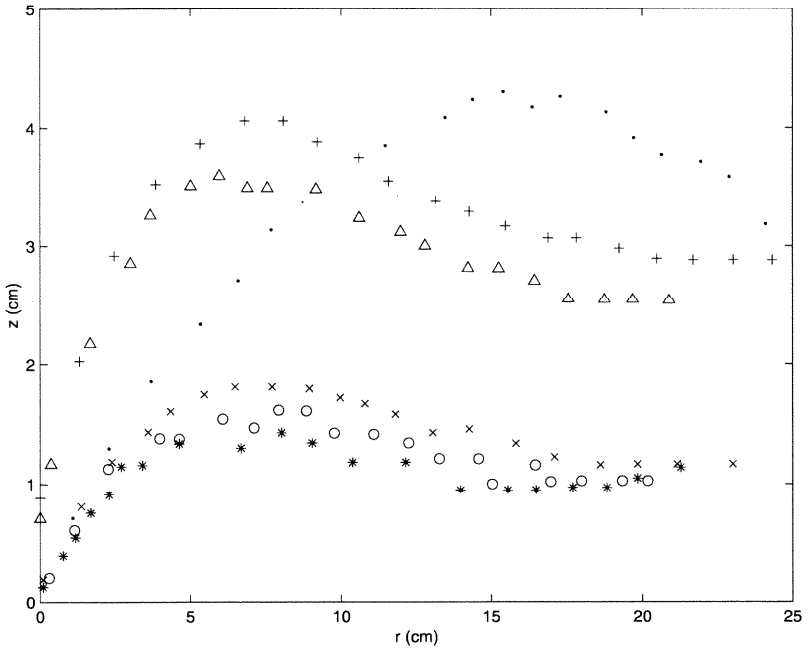

(a) Smaller scale experiments; (×) for run 1s, (○) for run 2s, (∗) for run 3s, (·) for run 4s, (+) for run 5s, and (△) for run 6s.

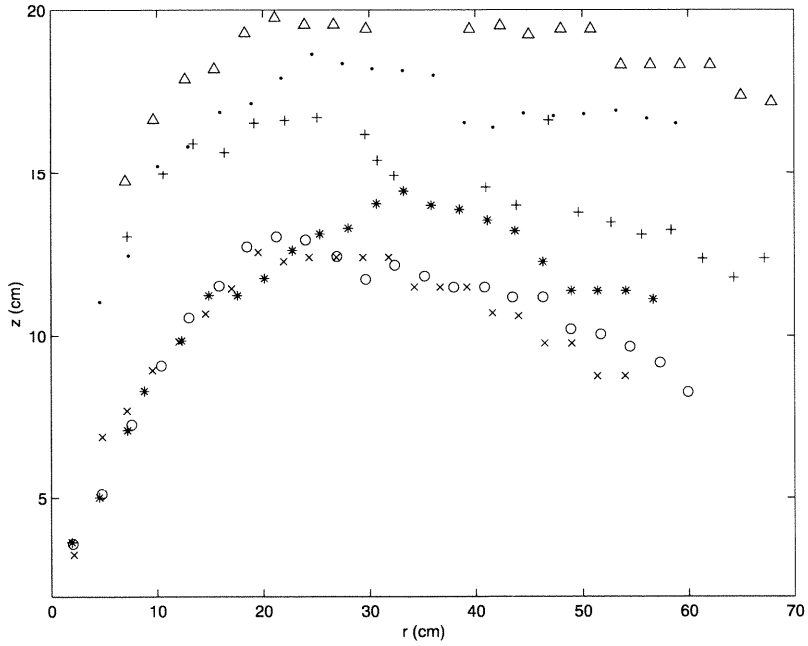

(b) Larger scale experiments; (×) for run 1l, (○) for run 2l, (∗) for run 3l, (·) for run 4l, (+) for run 5l, and (△) for run 6l.

Figure 4.4 Contact line results from the stationary model experiments.

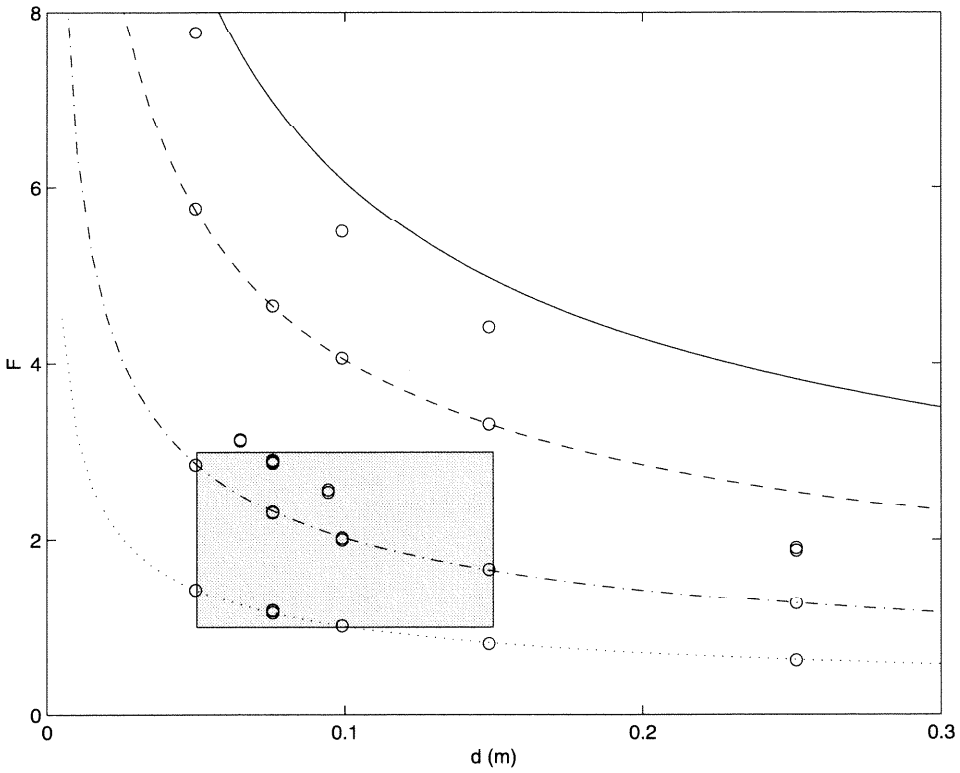

Figure 4.5 Parameter space with (○) for the towed model run conditions. The lines show Froude number, **F**, as a function of draft, d, for constant velocity, U: (—) for $U = 6$ m/s, (- -) for $U = 4$ m/s, (- · - ·) for $U = 2$ m/s, and (· · ·) for $U = 1$ m/s. The shaded region represents those run conditions produced in the larger scale stationary model experiments.

4.3 Bow wave profile results

The wave profile was measured in the towed model and the larger scale stationary model experiments. In the towed model experiments, the $\theta = 26°$ wedge model was used. A summary of the test conditions for this model is shown in a parameter space including Froude number, **F**, and model draft, d, in Figure 4.5. Of particular interest were those conditions which overlapped those in the stationary model experimental conditions, indicated by the shaded region. The other experimental conditions expanded this range to the maximum carriage speed, U, and model draft. The model draft was limited by a maximum allowable drag force, D, of 150 lbs imposed by towing carriage constraints.

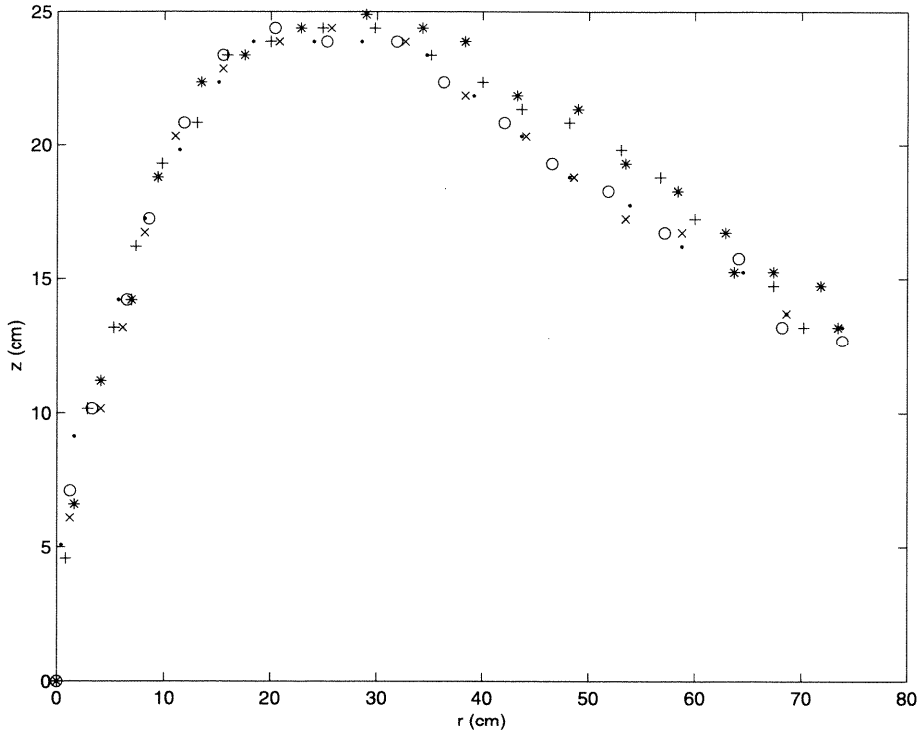

Figure 4.6 Bow wave profiles from the towed model experiments, $d = 7.54$ cm and $\mathbf{F} \approx 2.91$. Each symbol represents a different run, ($\times$) for $U = 2.48$ m/s, ($\circ$) for $U = 2.50$ m/s, ($*$) for $U = 2.50$ m/s, ($\cdot$) for $U = 2.50$ m/s, and ($+$) for $U = 2.50$ m/s.

The bow wave profile in the towed wedge experiments was measured from digitized images of the bow wave. The camera was secured to the carriage and oriented perpendicular to the wedge model side wall; its field of view encompassed this entire wall. Figure 4.6 shows the bow wave profile for five repeated runs having approximately the same velocity, and demonstrates the repeatability of this measurement technique. The leading edge is at $r = 0$ and $z = 0$ is the location of the undisturbed free surface. Figure 4.7 presents a summary of the data from these experiments. Note that for some of the higher velocity runs, the maximum height of the bow wave profile was not in the field of view of the camera. In these runs, the model generated a spray sheet which was quite different from the bow wave shown in Figure 4.3(b). This sheet would often break up into droplets before the maximum height above the undisturbed free surface was achieved.

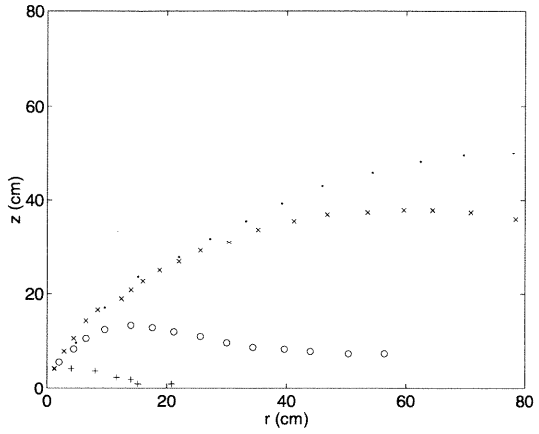

(a) $d = 4.95$ cm; (+) for $U = 1.00$ m/s and $\mathbf{F} = 1.43$, ($\circ$) for $U = 1.99$ m/s and $\mathbf{F} = 2.86$, ($\times$) for $U = 4.01$ m/s and $\mathbf{F} = 5.76$, and ($\cdot$) for $U = 5.41$ m/s and $\mathbf{F} = 7.77$.

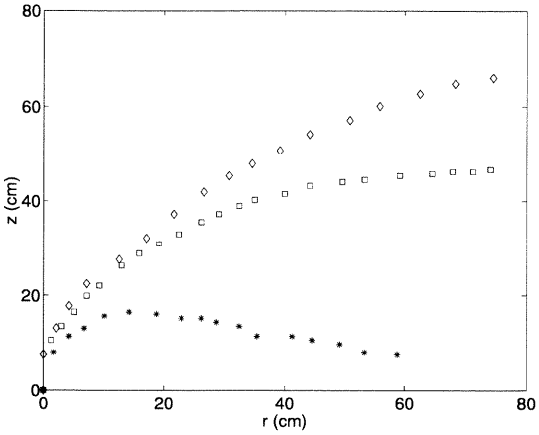

(b) $d = 9.91$ cm; ($*$) for $U = 1.98$ m/s and $\mathbf{F} = 2.01$, ($\square$) for $U = 4.00$ m/s and $\mathbf{F} = 4.06$, and ($\diamond$) for $U = 5.41$ m/s and $\mathbf{F} = 5.49$.

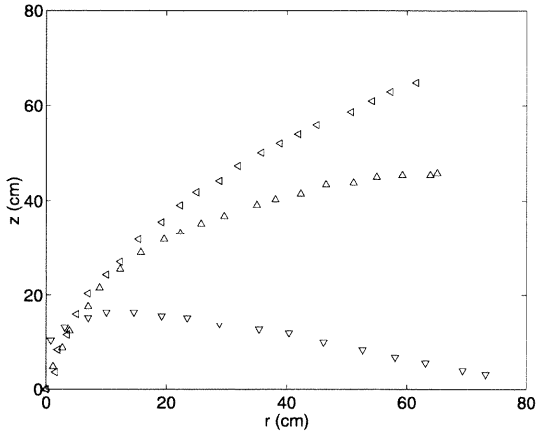

(c) $d = 14.86$ cm; ($\triangledown$) for $U = 2.01$ m/s and $\mathbf{F} = 1.66$, ($\triangle$) for $U = 4.00$ m/s and $\mathbf{F} = 3.31$, and ($\triangleleft$) for $U = 5.33$ m/s and $\mathbf{F} = 4.41$.

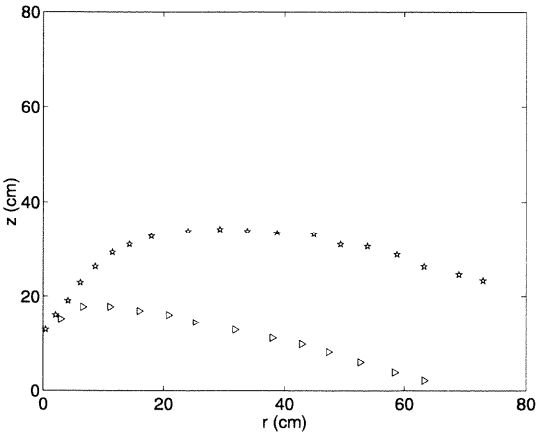

(d) $d = 25.14$ cm; ($\triangleright$) for $U = 2.00$ m/s and $\mathbf{F} = 1.27$, and ($\star$) for $U = 2.94$ m/s and $\mathbf{F} = 1.87$.

Figure 4.7 Summary of bow wave profiles from the towed model experiments, $\theta = 26°$.

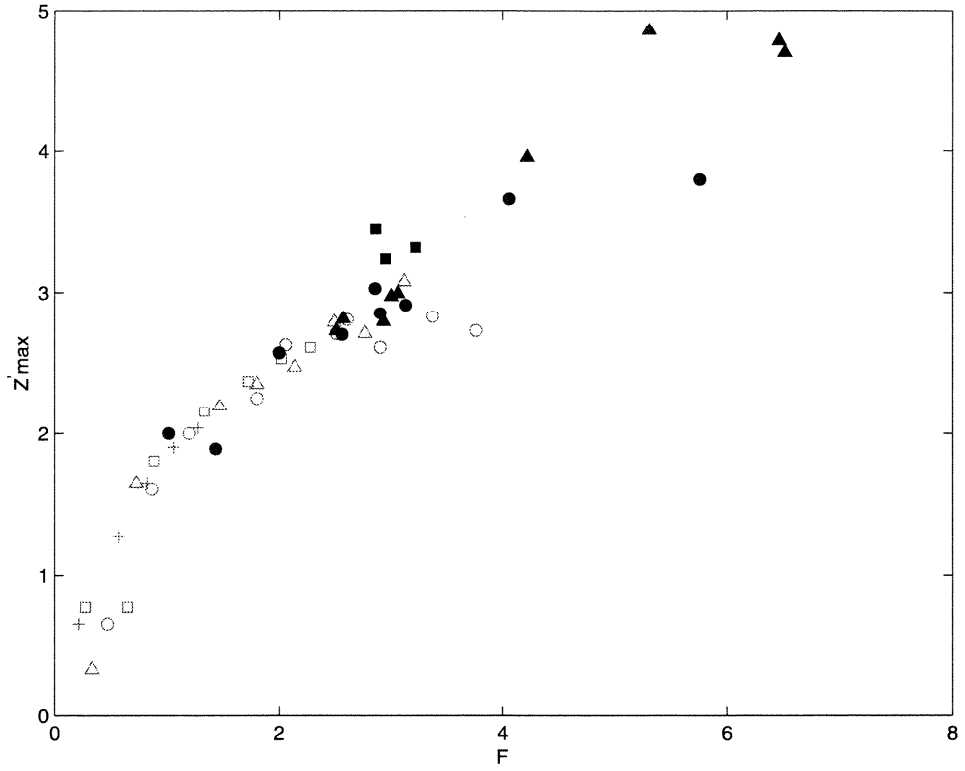

Figure 4.8 Comparison of the non-dimensional maximum wave profile height, Z'_{max}, as a function of Froude number, **F**, between the stationary and towed model experiments. For the stationary model experiments $\theta = 13.4°$ for the smaller scale (▲), and $\theta = 26.8°$ for the larger scale (■). For the towed model experiments (●), $\theta = 26°$. For Ogilvie's towed model experiments, $\theta = 15°$ and (○) for $d = 10.2$ cm, (△) for $d = 20.4$ cm, (□) for $d = 30.5$ cm, and (+) for $d = 40.6$ cm.

4.4 Comparison of stationary and towed model results

Both the smaller and larger scale experiments in the laboratory flumes were conducted using flow which impinged on a stationary model where the draft was equal to the depth. We first address the issue of whether these experiments generated waves similar to those created at the bow of a model towed at a finite draft in much deeper water (note the depth of water in the towing tank was approximately 3.7 m). The maximum height of the wave profiles, Z_{max}, was measured for different Froude numbers for each set of experiments. For the smaller scale stationary model experiments, the maximum height was measured

using an electronic point gage, but for the towed model and larger scale stationary model experiments the free surface height was measured from digitized images of the wave with the focal plane of the camera parallel to the model side wall.

The results are shown in Figure 4.8 together with the results from towed wedge experiments performed by Ogilvie [39] who also made measurements from photographs of the wave. All free surface heights were non-dimensionalized as in Ogilvie:

$$Z'_{max} = \frac{90 Z_{max}}{\mathbf{F} \cdot d \cdot \theta}. \tag{4.1}$$

The location of the undisturbed free surface was the datum level for Z_{max}. The maximum free surface height for the larger scale experiments is slightly greater than for the other experiments, but probably this is due to the experimental error associated with measuring an unsteady free surface. More importantly, Figure 4.8 suggests that the two types of experiments (towed model and stationary model) can yield similar results and that the water depth and model draft to depth ratio does not have a significant effect on the bow wave profiles.

To further validate the experimental simulation of the bow wave using a stationary model, the full wave profiles from the larger scale stationary model experiments and the towed model experiments are compared in Figure 4.9. The data from both types of experiments shows good agreement near the leading edge, demonstrating that the two experiments can yield similar results in that region. Around the maximum profile height, the agreement is certainly not good. This discrepancy could be due, in part, to the alignment of the video camera. If the camera was not oriented exactly perpendicular to the model and parallel with the undisturbed free surface then the view of the wave in the two experiments would be different.

A summary of all the data from the towed model experiments is presented in Figure 4.10. Table 4.2 lists the flow conditions corresponding to each symbol. As in Figure 4.8, the free surface heights were non-dimensionalized according to equation 4.1. The distance along the

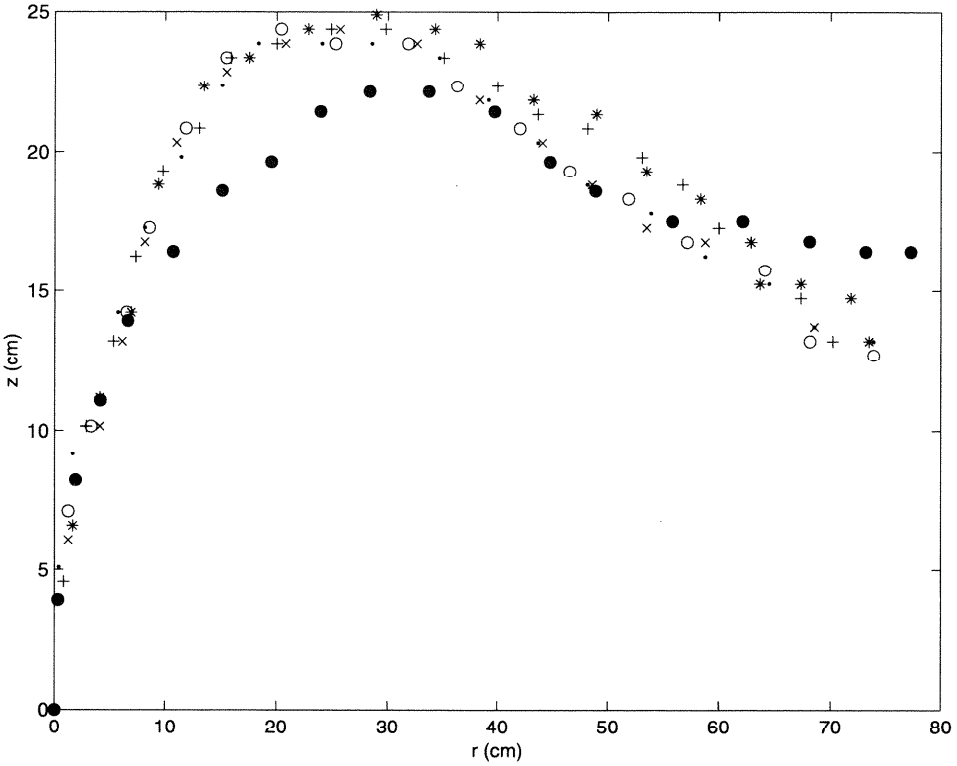

Figure 4.9 Towed model and larger scale stationary model bow wave profiles for $\theta = 26°$. For the towed model profiles: $d = 7.54$ cm and $\mathbf{F} \approx 2.91$ with ($\times$) for $U = 2.48$ m/s, ($\circ$) for $U = 2.50$ m/s, ($*$) for $U = 2.50$ m/s, ($\cdot$) for $U = 2.50$ m/s, and ($+$) for $U = 2.50$ m/s. For the stationary model, ($\bullet$), $d = 7.54$ cm and $U = 2.46$ m/s.

model surface was also non-dimensionalized as in Ogilvie:

$$r' = \frac{r}{\mathbf{F} \cdot d} \tag{4.2}$$

Figure 4.10 demonstrates that $\mathbf{F}d$ is an incorrect scaling for these waves away from the leading edge for both the r and z-directions. Correct scaling would collapse all of the data onto a single curve. Other scaling possibilities will be presented in section 4.6.

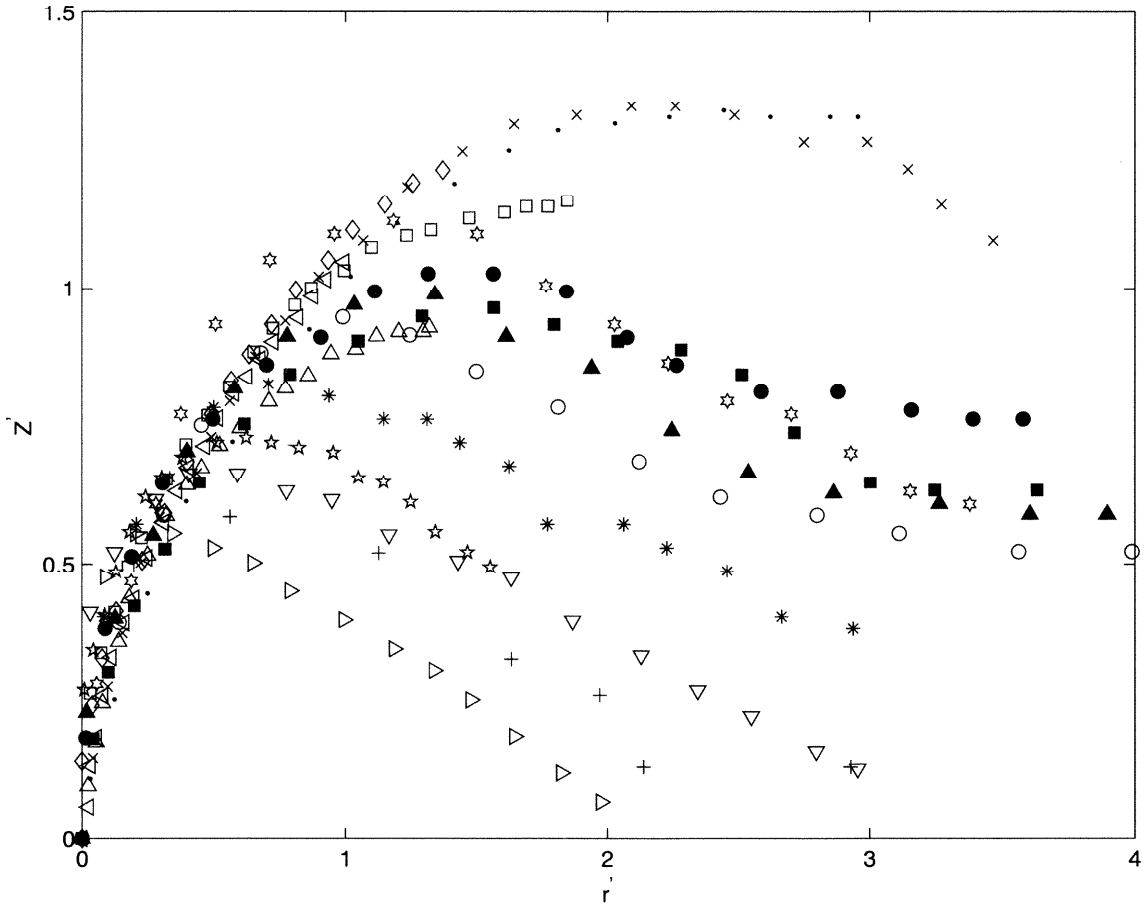

Figure 4.10 Towed model (open symbols) and larger scale stationary model (filled symbols) non-dimensional bow wave profiles for $\theta = 26°$. The flow conditions for the different symbols are listed in Table 4.2.

Symbol	Experiment	U (m/s)	d (cm)	**F**
●	Stationary	2.46	7.54	2.86
■	Stationary	2.39	6.68	2.95
▲	Stationary	2.22	4.86	3.22
+	Towed	1.00	4.95	1.43
○	Towed	1.99	4.95	2.86
x	Towed	4.01	4.95	5.76
·	Towed	5.41	4.95	7.77
✡	Towed	2.50	7.54	2.91
∗	Towed	1.98	9.91	2.01
□	Towed	4.00	9.91	4.06
◇	Towed	5.41	9.91	5.49
▽	Towed	2.01	14.86	1.66
△	Towed	4.00	14.86	3.31
◁	Towed	5.33	14.86	4.41
▷	Towed	2.00	25.14	1.27
⋆	Towed	2.94	25.14	1.87

Table 4.2 Bow wave profile experimental conditions, $\theta = 26°$.

4.5 Plunging jet shape

In the stationary model experiments, the free surface height was measured for different flow cross sections to study the shape of the plunging wave jet. Describing this feature of the bow wave is important not only for understanding the three-dimensional structure of the waves, but for understanding the air entrainment process as well. As described in Chapter 1, many researchers have identified the jet size (thickness or diameter) and jet velocity as key parameters for modeling air entrainment by plunging jets. In these experiments, the jet size was measured directly, and the jet velocity was calculated as described later in this section.

In the larger scale experiments, cross sections were measured using the free surface probe (described in section 2.2.1) at three different streamwise locations for each flow condition. Figures 4.11, 4.12, and 4.13 present some typical results which show both the exterior and interior surfaces of the jet. The undisturbed free surface is $z = 0$ cm and the leading edge of the plate is at $(x, y) = (0, 0)$. The data describing the interior surface is limited by the large amount of splash in this region of the flow which caused incorrect gage readings. However, there were adequate data to define the jet thickness, and the jet thickness was about 4 cm for the jets shown in Figure 4.12.

In the towed model experiments, flow frontal aspects were measured from digitized images of the bow wave. The camera was secured to the carriage and oriented parallel to one side of the wedge so that its field of view encompassed the entire wave cross section. A typical example of an image is shown in Figure 4.14. This measurement technique was more appropriate for towed model experiments than using the free surface probes, and it yielded similar information. Figure 4.15 shows the bow wave frontal aspects for five different run conditions having nearly the same velocity. Note that the y^*-coordinate is perpendicular to the side of the wedge, and the leading edge of the wedge is approximately located at $y^* = 0$. The undisturbed free surface at the leading edge of the wedge is located at $z^* = 0$. These results demonstrate the repeatability of this measurement technique, and also show a jet which is about 2–3 cm thick. Also, there were enough data describing the interior surface of the jet to measure its angle of impingement, β, measured relative to the undisturbed free surface as 58°.

Since the plunging wave jet is in free-fall just before impact, it is possible to calculate

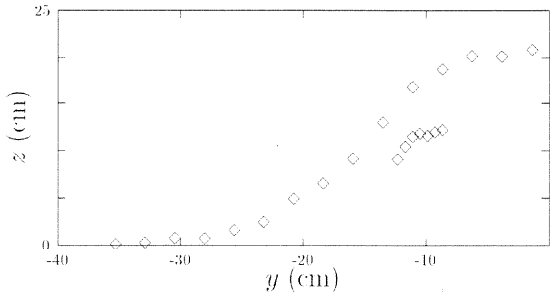

(a) Jet cross section at streamwise coordinate, x = 69.1 cm.

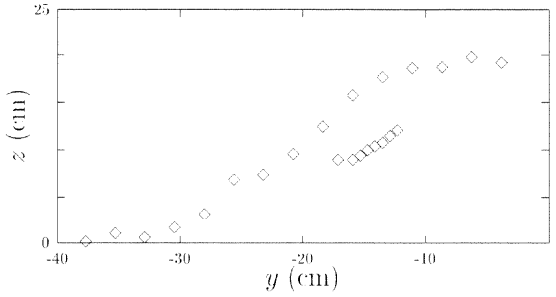

(b) Jet cross section at streamwise coordinate, x = 64.0 cm.

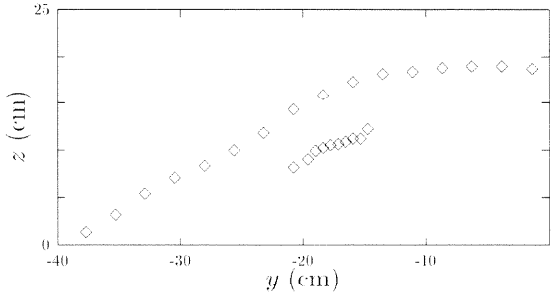

(c) Jet cross section at streamwise coordinate, x = 58.9 cm.

Figure 4.11 Cross sections of the plunging wave jet in the larger scale stationary wedge experiments ($\theta = 25.4°$) for different distances downstream of the deflecting plate leading edge; U = 2.39 m/s, d = 9.47 cm, and $\mathbf{F}$ = 2.48.

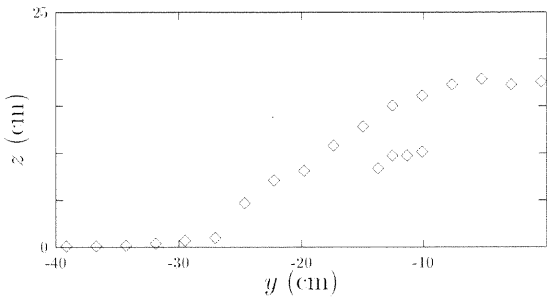

(a) Jet cross section at streamwise coordinate, x = 69.1 cm.

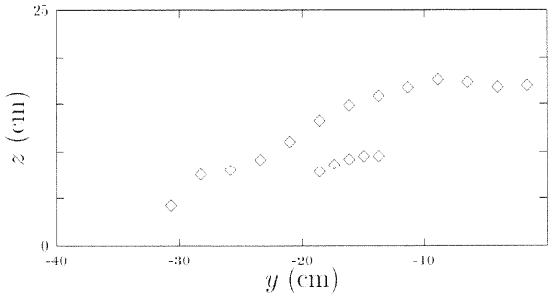

(b) Jet cross section at streamwise coordinate, x = 64.0 cm.

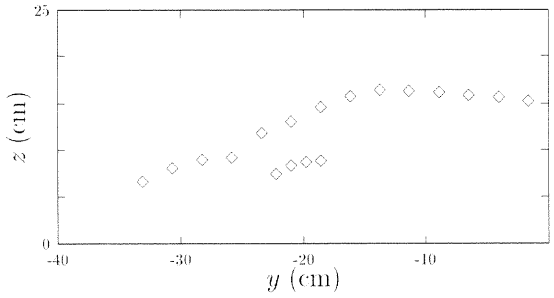

(c) Jet cross section at streamwise coordinate, x = 58.9 cm.

Figure 4.12 Cross sections of the plunging wave jet in the larger scale stationary wedge experiments ($\theta = 25.4°$) for different distances downstream of the deflecting plate leading edge; U = 2.41 m/s, d = 6.72 cm, and $\mathbf{F}$ = 2.97.

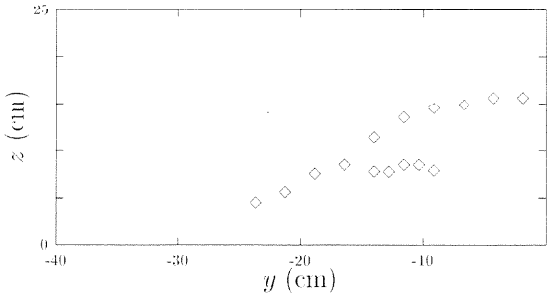

(a) Jet cross section at streamwise coordinate, x = 69.1 cm.

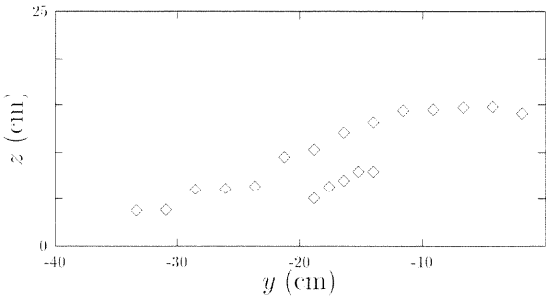

(b) Jet cross section at streamwise coordinate, x = 64.0 cm.

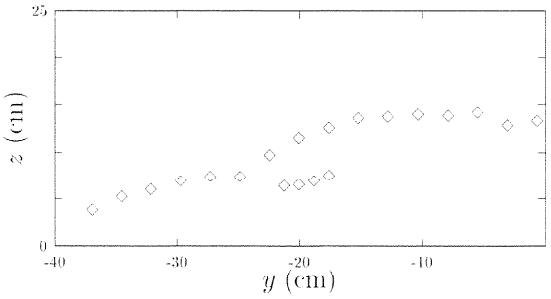

(c) Jet cross section at streamwise coordinate, x = 58.9 cm.

Figure 4.13 Cross sections of the plunging wave jet in the larger scale stationary wedge experiments ($\theta = 25.4°$) for different distances downstream of the deflecting plate leading edge; U = 2.70 m/s, d = 6.11 cm, and $\mathbf{F}$ = 3.48.

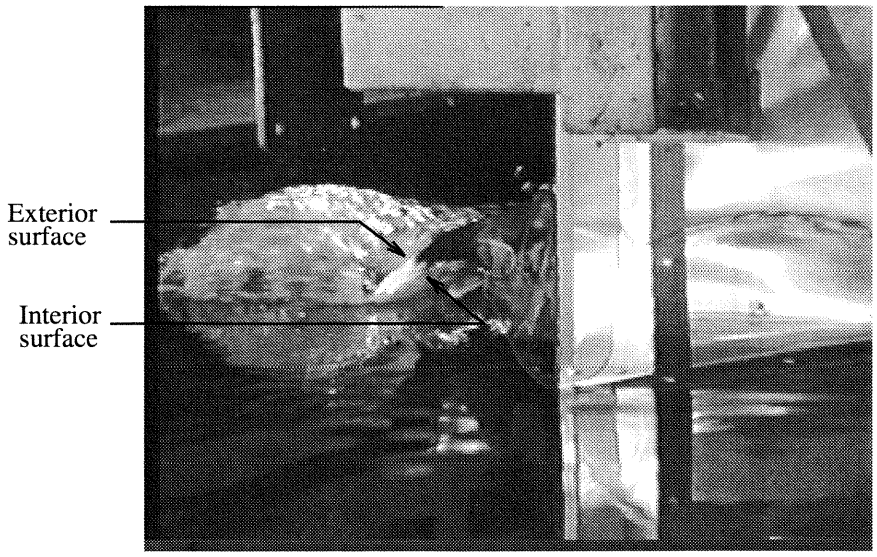

Figure 4.14 Video of the plunging jet in the towed model experiments for $\theta = 26°$, $U = 2.50$ m/s, and $d = 7.54$ cm. The camera is looking at the bow of the model parallel to the starboard side.

the horizontal water particle velocity at the crest of the plunging breaker, U_b, using the angle of impingement, β, and the free-fall height, h_f, determined from Figure 4.15 and the equation

$$tan(\beta) = \frac{\sqrt{2gh_f}}{U_b}. \tag{4.3}$$

The jet velocity at impact, U_i, also can be calculated from

$$U_i = \sqrt{U_b^2 + 2gh_f}. \tag{4.4}$$

For $\beta = 58°$ and $h_f = 20$ cm, equations 4.3 and 4.4 give $U_b = 1.2$ m/s and $U_i = 2.3$ m/s, reasonable values since the towing speed was 2.5 m/s.

The plunging jet thickness was similar for the towed and stationary model experiments. Figures 4.12 and 4.15 have approximately the same flow conditions, and the plunging jet was 4 cm thick in Figure 4.12 and 2–3 cm thick in Figure 4.15. Additional comparisons were not made because of the limited number of interior jet surface data for the stationary

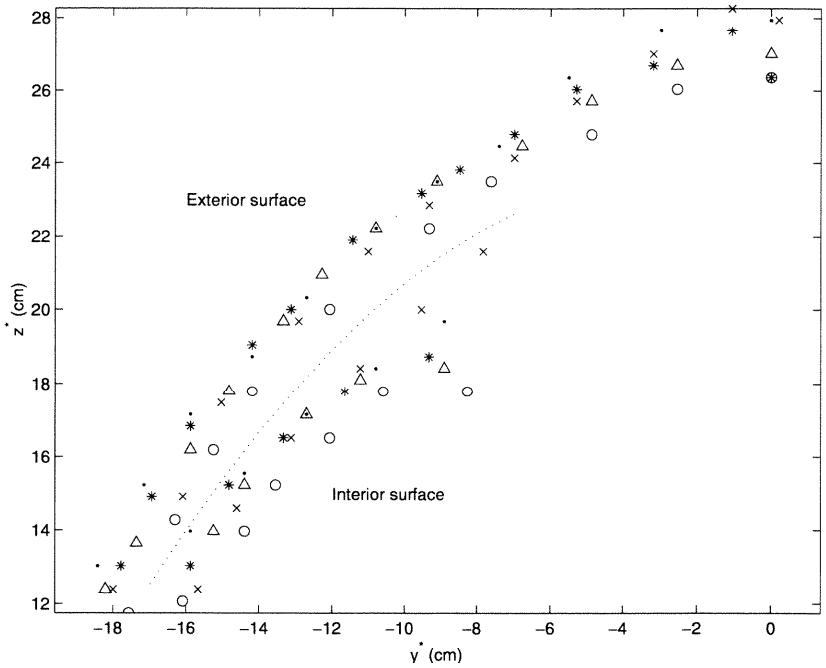

Figure 4.15 Frontal aspects of the plunging wave jet in the towed model experiments for $d = 7.54$ cm and $\theta = 26°$. The symbols indicate the velocity ($\times$) for $U = 2.48$ m/s, ($\circ$) for $U = 2.50$ m/s, ($*$) for $U = 2.50$ m/s, ($\cdot$) for $U = 2.50$ m/s, and ($\triangle$) for $U = 2.50$ m/s. The dotted line separates the exterior jet surface data from the interior jet surface data.

model experiments and because the measurement cross sections were different for the two experiments.

4.6 Scaling discussion

Understanding the manner in which these waves scale is necessary in order to extend laboratory experiments to flows for ship hulls of various shapes operating at different speeds and drafts. The scaling of distances in both the r and z-directions are considered separately. The free surface height, Z, is a function of the following parameters:

$$Z = f(U, d, \theta, \phi, g, \rho, \mu)$$

where ρ is the water density and μ is the dynamic viscosity. Likewise, the location of the maximum height in the r-direction, l_{max}, can be expressed as:

$$l_{max} = f(U, d, \theta, \phi, g, \rho, \mu).$$

Surface tension, σ, is neglected since the Weber number, $We = \rho U^2 d/\sigma$, is much greater than one for these flows. By the Buckingham Pi theorem, these functional relationships must be of the equivalent forms

$$\frac{Z}{d} = f(\mathbf{F}, Re, \theta, \phi) \tag{4.5}$$

and

$$\frac{l_{max}}{d} = f(\mathbf{F}, Re, \theta, \phi) \tag{4.6}$$

where $Re = (Ud\rho)/\mu$, the upstream Reynolds number. In this section, the scaling with the velocity, U, and draft, d, is discussed. The scaling with the geometric parameters, namely the bow half angle, θ, and the dihedral angle, ϕ, is also discussed. This information is then used to obtain the form of the functions in equations 4.5 and 4.6.

4.6.1 Flow parameters

The bow wave profile data discussed in this section are from the towed model experiments since the towed model experiments encompassed a wider range of flow conditions (velocities, U, and drafts, d) than the stationary model experiments. To investigate the scaling in the z-direction, the maximum height of the bow wave profile, Z_{max}, is plotted against velocity in Figure 4.16(a). Note that these are the same data as presented in Figure 4.8. Figure 4.16(a) demonstrates quite convincingly that $Z_{max} \propto U^{1.5}$; the linear curve fit was $Z_{max} = 5.64U^{1.49}$ using the method of least squares. Thus, Z_{max} was scaled by $U^{1.5}$ and $Z_{max}/U^{1.5}$ was plotted against draft in Figure 4.16(b). This plot then suggests that $Z_{max}/U^{1.5} \propto d^{0.25}$; the linear curve fit was $Z_{max}/U^{1.5} = 3.67d^{0.189}$. These results together

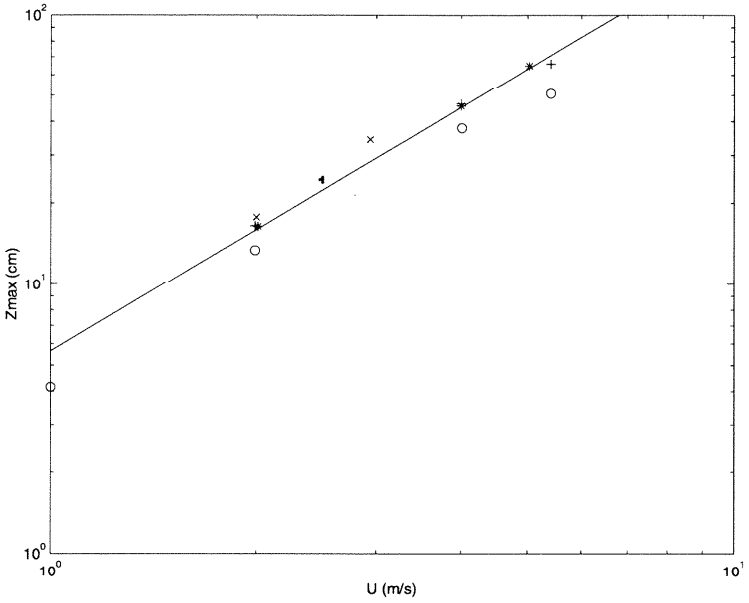

(a) Z_{max} as a function of U; ($\circ$) for $d = 4.95$ cm, ($\cdot$) for $d = 7.54$ cm, ($+$) for $d = 9.91$ cm, ($*$) for $d = 14.86$ cm, and ($\times$) for $d = 25.14$ cm. The equation of the line shown is $Z_{max} = 5.64U^{1.50}$.

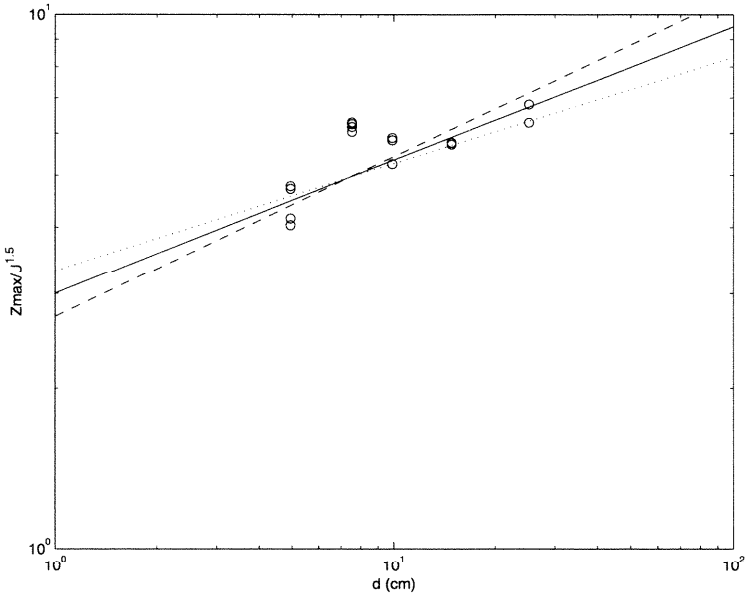

(b) $Z_{max}/U^{1.5}$ as a function of d; the lines are ($\cdots$) for $Z_{max}/U^{1.5} = 3.32d^{0.20}$, (—) for $Z_{max}/U^{1.5} = 3.00d^{0.25}$, and (--) for $Z_{max}/U^{1.5} = 2.72d^{0.30}$.

Figure 4.16 Scaling of the maximum wave heights for the towed model experiments with velocity and draft shown on logarithmic scales.

indicate that

$$\frac{Z_{max}}{d} \propto U^{1.5} d^{-0.75}$$

and equation 4.5 becomes

$$\frac{Z_{max}}{d} = \mathbf{F}^{1.5} \cdot f(\theta, \phi). \tag{4.7}$$

Thus, it appears that the normalized maximum is independent of the upstream Reynolds number.

To investigate the scaling in the r-direction, a similar procedure was followed. First the location of the maximum height, l_{max}, was plotted against velocity as shown in Figure 4.17(a). Figure 4.17(a) demonstrates that $l_{max} \propto U^2$; the linear curve fit was $l_{max} = 3.46U^{1.96}$ using the method of least squares. The location of the maximum height was then scaled by U^2 and l_{max}/U^2 was plotted against draft as shown in Figure 4.17(b). Figure 4.17(b) suggests $l_{max}/U^2 \propto d^{-0.5}$; the linear curve fit was $l_{max}/U^2 = 7.03d^{-0.311}$. These results together indicate that

$$\frac{l_{max}}{d} \propto U^2 d^{-1.5}$$

and to assure this behavior with U and d, equation 4.6 becomes

$$\frac{l_{max}}{d} = \mathbf{F}^{7/3} Re^{-1/3} \cdot f(\theta, \phi). \tag{4.8}$$

The results from this scaling investigation were somewhat disappointing since they did not agree with the scaling suggested by Ogilvie, nor with the scaling suggested by the equations presented in section 3.1.3. Recall that in the z-direction, Ogilvie suggested a non-dimensionalization of $Z' = Z/\mathbf{F}d$ and the equations in section 3.1.3 suggested a non-dimensionalization of $Z' = z/d$ for a given θ. The equations in section 3.2 did not give any additional insight regarding the scaling since the solution is for flows where $\mathbf{F} < 1$. Intuitively, it seems that distances in the z-direction should scale with some combination of the velocity head, $U^2/2g$, and the draft, though it is unclear which length would be more

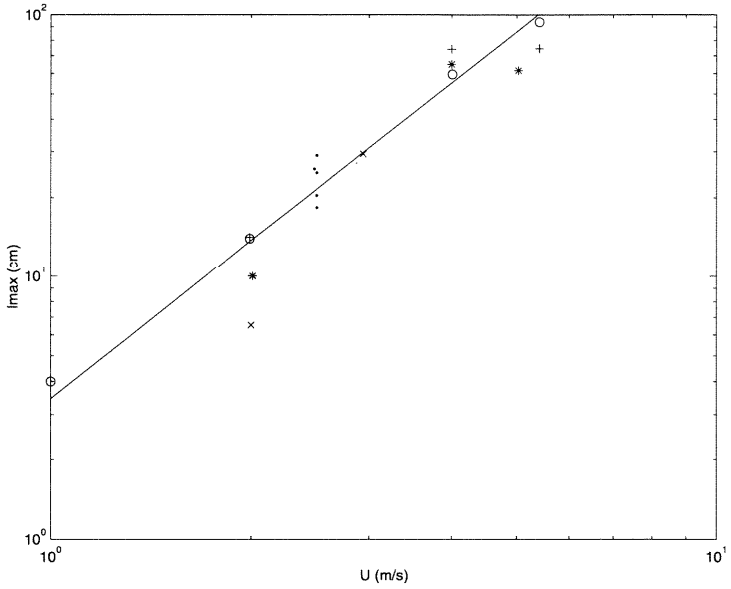

(a) l_{max} as a function of U: (o) for $d = 4.95$ cm, (·) for $d = 7.54$ cm, (+) for $d = 9.91$ cm, (*) for $d = 14.86$ cm, and (×) for $d = 25.14$ cm. The equation of the line shown is $l_{max} = 3.46U^{2.00}$.

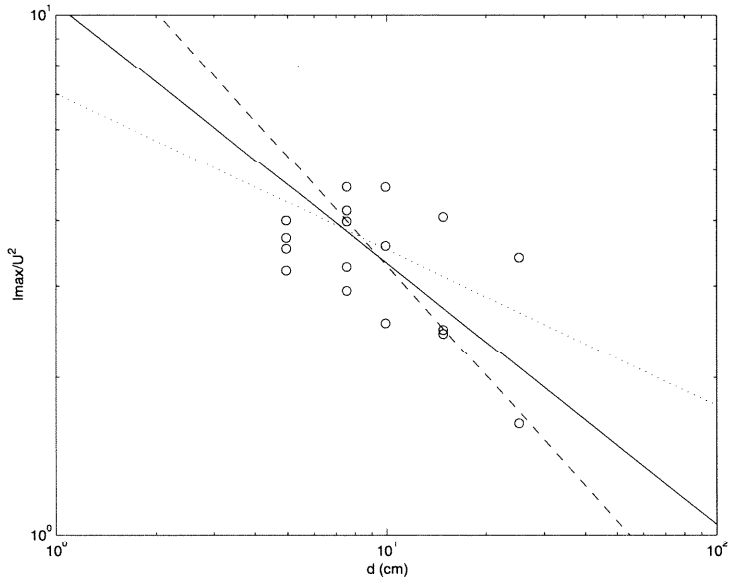

(b) l_{max}/U^2 as a function of d; the lines are (· · ·) for $l_{max}/U^2 = 7.03d^{-0.30}$, (—) for $l_{max}/U^2 = 10.5d^{-0.50}$, and (--) for $l_{max}/U^2 = 16.4d^{-0.70}$.

Figure 4.17 Scaling of the location of maximum wave heights for the towed experiments with velocity and draft shown on logarithmic scales.

important. The scaling extrapolated from the experimental data reflects this idea, and perhaps both Ogilvie's analysis and the analysis presented in section 3.1 include assumptions which mask the true scaling seen in the experiments.

In the r-direction, recall that Ogilvie suggested a non-dimensionalization of $r' = r/\mathbf{F}d$, and while the equations presented in section 3.1.3 did not suggest a specific scaling in the r-direction, they did suggest $x' = x/\mathbf{F}d$, and perhaps this can be applied to other horizontal distances. The scaling relation extrapolated from the experiments includes a Reynolds number and is different from both of these ideas. The Reynolds number provides the apparent and appropriate scaling with velocity and draft, but it is not clear that it has physical meaning. We speculate, however, that viscous effects could influence the location of the maximum height. For example if ν increased, the Reynolds number would decrease, and according to the scaling relation l_{max} would move downstream from the leading edge. This seems correct because an increase in ν would also cause an increase in the shear stress along the plate. Then, the flow would lose energy in overcoming this shear stress and take longer to achieve its maximum.

The scaling described in the preceding paragraphs was then applied to all of the data from the bow wave profile experiments, and the scaled data from the $\theta = 26°$ models are presented in Figure 4.18. Theoretically, all of the data should collapse onto a single profile. Figure 4.18 demonstrates remarkable agreement of the wave profiles near the leading edge; however, the profiles deviate soon thereafter, particularly those for $d = 4.95$ cm and for $d = 7.54$ cm. For the $d = 4.95$ cm profiles, the deviation is in the r-direction, but for the $d = 7.54$ cm profiles, the deviation is in the z-direction. Deviations such as these were expected because the scaling was empirically determined using curve fitting techniques. In summary, this scaling is certainly an improvement from that used in Figure 4.10 though it does not completely collapse the data.

The contact line data from the stationary model experiments was also scaled. Figure 4.19 presents the non-dimensional contact lines using the z-direction scaling described in the preceding paragraphs, and Table 4.1 lists the corresponding flow conditions. The scaling appears to work quite well for the smaller scale experiments where the run conditions are almost the same. The slight rise in most of the profiles occurring at $r/(\mathbf{F}^{7/3}R\epsilon^{-1/3}d) \approx 65$ is

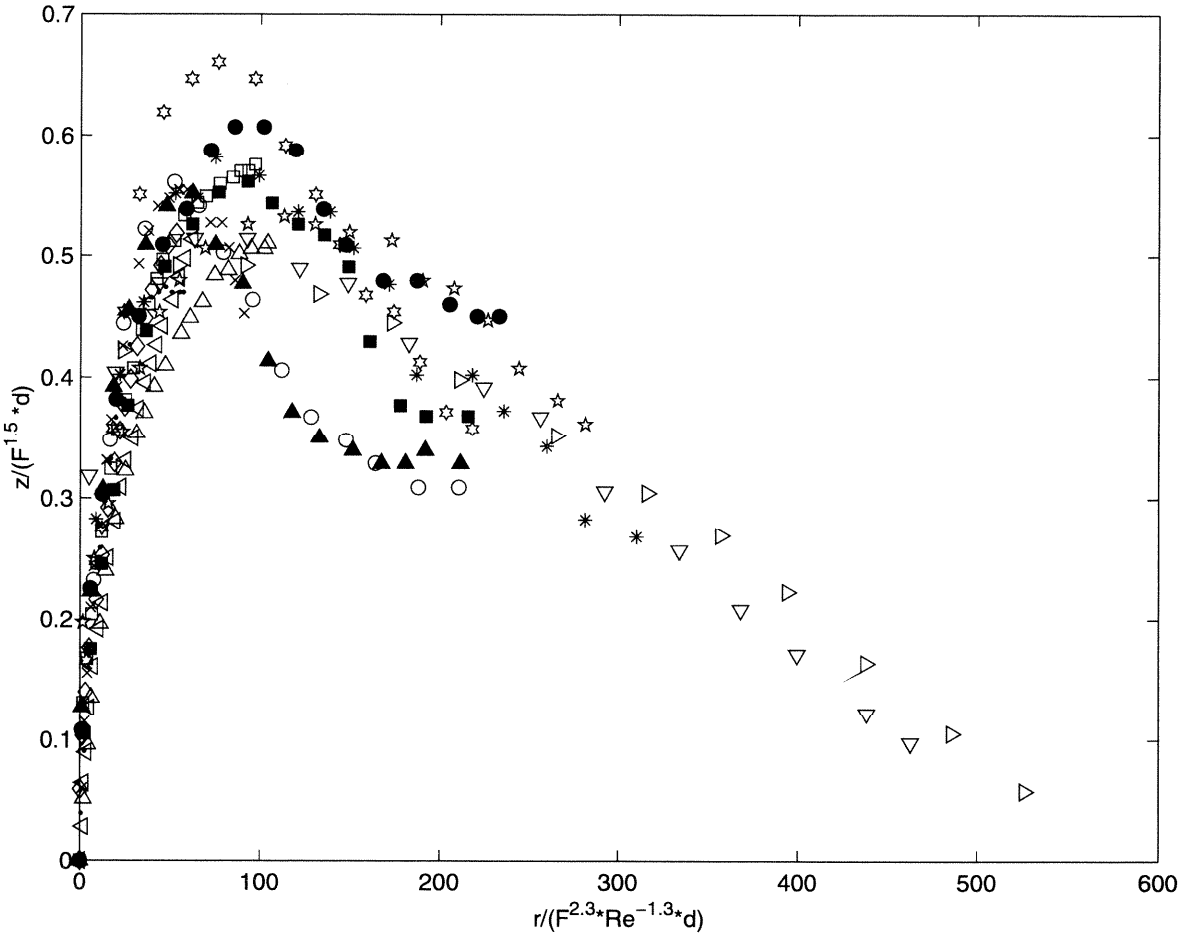

Figure 4.18 Non-dimensional bow wave profile data for $\theta = 26°$ shown as $z/(\mathbf{F}^{1.5}d)$ plotted against $r/(\mathbf{F}^{2.3} \cdot Re^{-0.3} \cdot d)$. The open symbols represent the towed model experiments and the filled symbols represent the stationary model experiments. The flow conditions for all of the different symbols are listed in Table 4.2.

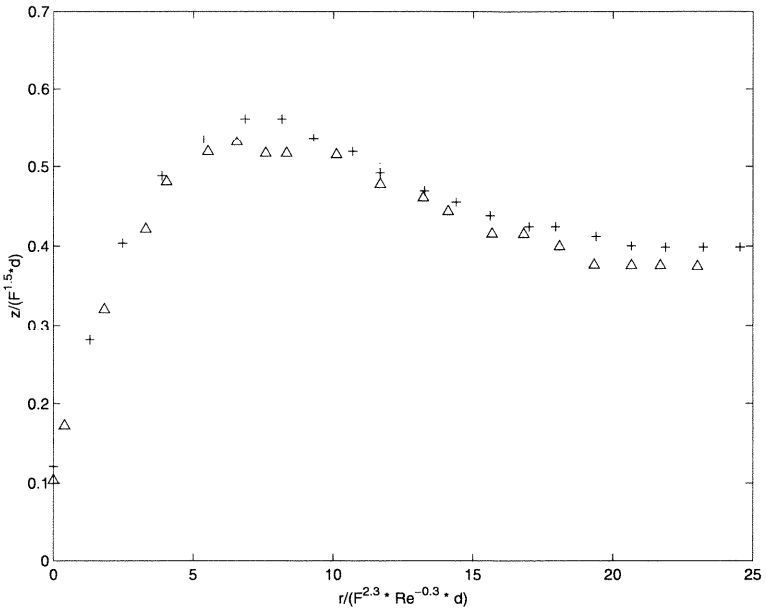

(a) Smaller scale $\theta = 26.3°$ experiments; (+) for run 5s, and ($\triangle$) for run 6s.

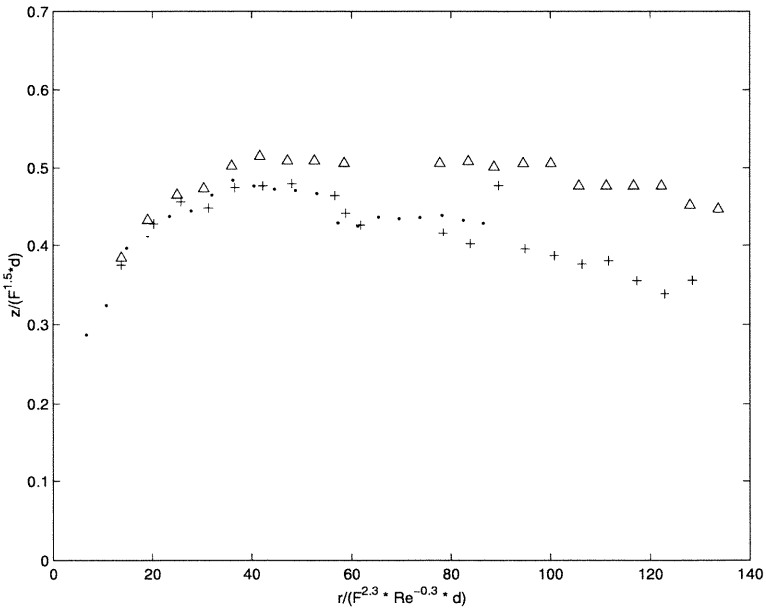

(b) Larger scale $\theta = 26.6°$ experiments; ($\cdot$) for run 4l, (+) for run 5l, and ($\triangle$) for run 6l.

Figure 4.19 Non-dimensional contact lines from the stationary model experiments.

caused by end effects associated with the deflecting plate. For the larger scale experiments, the scaling does not appear to be as effective. The difference in the profiles may be due to nonlinear effects.

In summary, the experimental data suggest a scaling with flow parameters which is not explained by the existing theoretical analyses but makes some intuitive physical sense.

4.6.2 Geometric parameters

The contact line data discussed in this section are from the stationary model experiments since the bow half angle, θ, and dihedral angle, ϕ, of the deflecting plate could be easily changed.

We first examine the effects of the model bow half angle, θ, on the contact lines of the waves from the stationary model experiments. Recall that Ogilvie suggested the free surface height scaled linearly with bow half angle as in equation 4.1. Using this idea along with the flow parameter scaling from section 4.6.1, the free surface height was non-dimensionalized according to

$$z^* = \frac{90z}{\mathbf{F}^{1.5} \cdot d \cdot \theta}$$

and the distance in the r-direction was non-dimensionalized by l_{max}. The results are presented in Figure 4.20, and Table 4.1 lists the corresponding flow conditions. For the smaller scale experiments, the scaling appears to work quite well. For the larger scale experiments, the scaling seemed to over-compensate for the larger bow half angle. This might be due simply to experimental error in measuring the contact line which was very unsteady in those experiments. (Recall that the scaling used on this same data in Figure 4.19(b) also did not seem to work as well as in the other experiments.) However, it is also possible that the bow wave profile height does not scale linearly with angle θ as suggested by Ogilvie and that a more complicated non-linear relationship exists.

We now examine the effect of the model dihedral angle, ϕ, on the waves using results from the smaller scale stationary model experiments. The dihedral angle, the angle between the deflecting plate and the free surface in the vertical plane, varied between 0° and 15°.

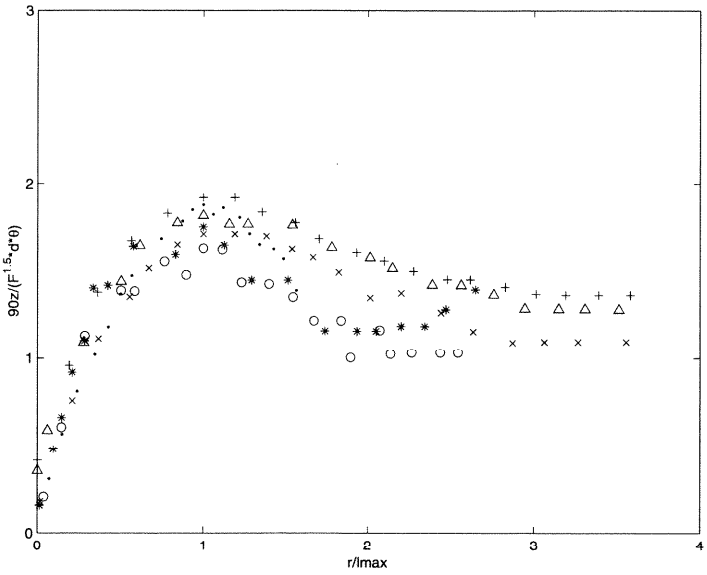

(a) Smaller scale experiments; ($\times$) for run 1s where $\theta = 13.2°$, ($\circ$) for run 2s where $\theta = 13.2°$, ($*$) for run 3s where $\theta = 13.2°$, ($\cdot$) for run 4s where $\theta = 13.2°$, ($+$) for run 5s where $\theta = 26.3°$, and ($\triangle$) for run 6s where $\theta = 26.3°$.

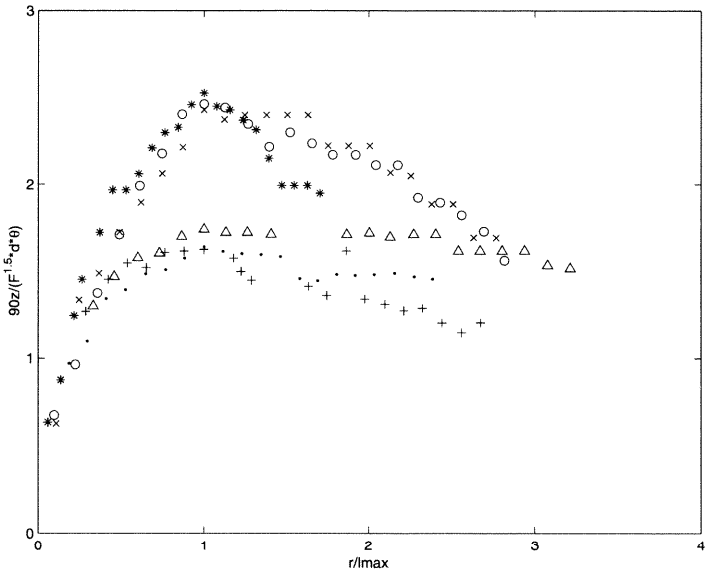

(b) Larger scale experiments; ($\times$) for run 1l where $\theta = 13.4°$, ($\circ$) for run 2l where $\theta = 13.4°$, ($*$) for run 3l where $\theta = 13.4°$, ($\cdot$) for run 4l where $\theta = 26.6°$, ($+$) for run 5l where $\theta = 26.6°$, and ($\triangle$) for run 6l where $\theta = 26.6°$.

Figure 4.20 Non-dimensional contact lines from the stationary wedge experiments for different bow half angles.

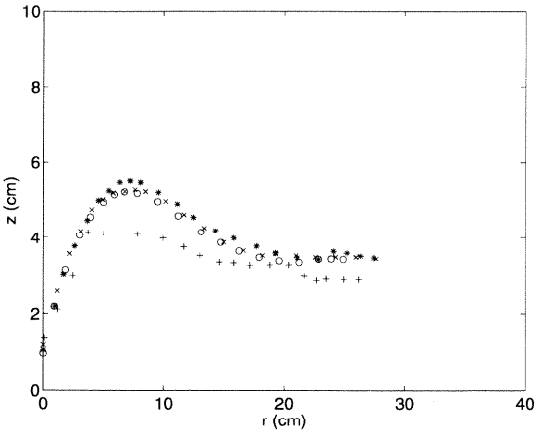

(a) $\mathbf{F} \approx 3$; (+) for $\mathbf{F} = 3.28$, (∗) for $\mathbf{F} = 2.98$, (○) for $\mathbf{F} = 3.02$, and (×) for $\mathbf{F} = 3.08$.

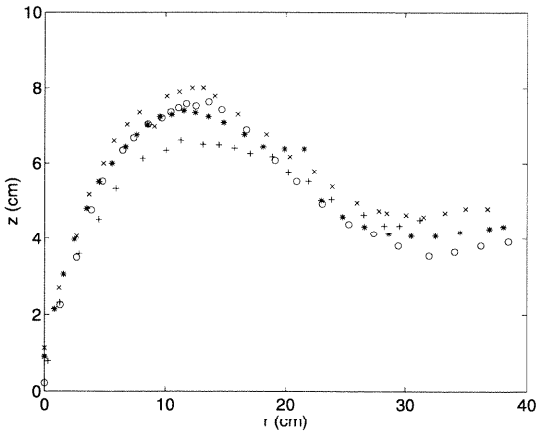

(b) $\mathbf{F} \approx 4$; (+) for $\mathbf{F} = 4.18$, (∗) for $\mathbf{F} = 4.06$, (○) for $\mathbf{F} = 4.30$, and (×) for $\mathbf{F} = 4.16$.

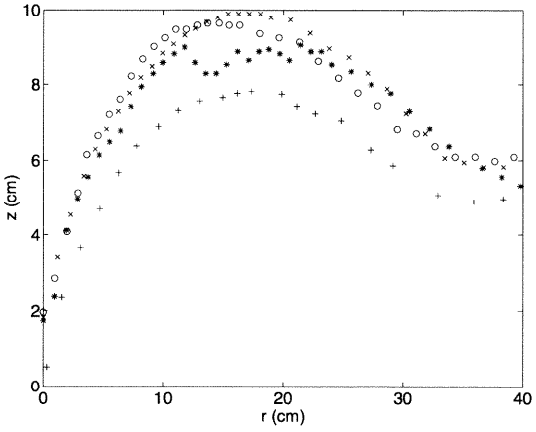

(c) $\mathbf{F} \approx 5$; (+) for $\mathbf{F} = 5.37$, (∗) for $\mathbf{F} = 5.22$, (○) $\mathbf{F} = 4.70$, and (×) $\mathbf{F} = 5.40$.

Figure 4.21 Effect of dihedral angle on the contact line for the smaller scale stationary model experiments; (+) for $\phi = 0°$, (∗) for $\phi = 5°$, (○) for $\phi = 10°$, and (×) for $\phi = 15°$.

The contact line was measured by moving the electronic point gage manually and averaging out the unsteadiness in the vertical direction for a set immersion percentage. The results of these tests are presented in Figure 4.21; for Figure 4.21(a) $\mathbf{F} \approx 3$, for Figure 4.21(b) $\mathbf{F} \approx 4$, and for Figure 4.21(c) $\mathbf{F} \approx 5$. It was impossible to achieve the same $\mathbf{F}$ for each dihedral angle tested since fine adjustment of the flow conditions was difficult; therefore, both the dihedral angle and $\mathbf{F}$ is noted for each contact line measured.

The data in Figure 4.21 show that the contact line is only weakly dependent on the dihedral angle; however, the elevation of the contact line does appear to increase as the dihedral angle increases. One hypothesis could be that $Z \propto 1/cos(\phi)$. These experiments were insufficient for proving or disproving this or other hypotheses for two reasons. First, only a small range of ϕ was explored, and second, the variation in $\mathbf{F}$ made it impossible to isolate the effects of ϕ. Additional tests including greater values of ϕ in a facility with more carefully controlled flow conditions are suggested. Also, the effects of ϕ on the contact line might be exaggerated in tests on a larger scale.

In summary, the experimental data indicate that the free surface heights may scale linearly with the bow half angle, θ, and are only weakly dependent on the dihedral angle, ϕ.

4.7 Surface disturbances

Surface disturbances were observed on the plunging face of the simulated bow wave in both the stationary and towed model experiments, and were recorded using various photographic techniques. In addition, these disturbances were manifest in signals from three wave gages flush-mounted on the deflecting plate (described in section 2.2.2) in the larger scale stationary model experiments. This section qualitatively and quantitatively describes the surface disturbances.

4.7.1 Observations of surface disturbances

The surface disturbances, first observed in the larger scale stationary model experiments, were sometimes difficult to isolate with the naked eye unless a strobe light was used. They subsequently were observed in the smaller scale stationary model experiments and

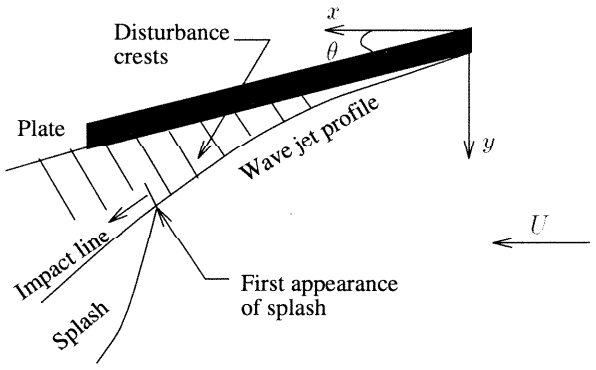

Figure 4.22 Schematic diagram of the top view of the bow wave with the crests of the surface disturbances.

in the towed model experiments. In all of the experiments, the disturbances appeared as "finger-like" structures on the plunging face of the wave. The "fingers," or the crests of the disturbances, were aligned perpendicular to the wave jet profile and the spacing between successive "fingers" seemed regular as shown schematically in Figure 4.22. The disturbances were barely visible near the leading edge of the plate and grew in amplitude as they convected downstream. They also grew in length, stretching as the liquid sheet fell away from the plate to form the plunging face of the wave.

The upstream flow conditions significantly affected the appearance of the surface disturbances. In the larger scale stationary model experiments, the surface of the wave was visibly rough due to the upstream flow conditions and this obscured the surface disturbances. The photograph in Figure 4.3(a) demonstrates this point. The upstream conditions could be more carefully controlled in the smaller scale stationary model experiments and the disturbances on the wave can be seen in Figure 2.6. The waves in the towed model experiments had the smoothest surface; therefore, it was easier to distinguish the surface disturbances. Frames of a video from these experiments are included in Figure 4.23.

4.7.2 High speed video results

High speed videos were used to quantify these observations. Figure 4.24 shows a sequence of frames from one of the high speed videos of the larger scale stationary model experiments.

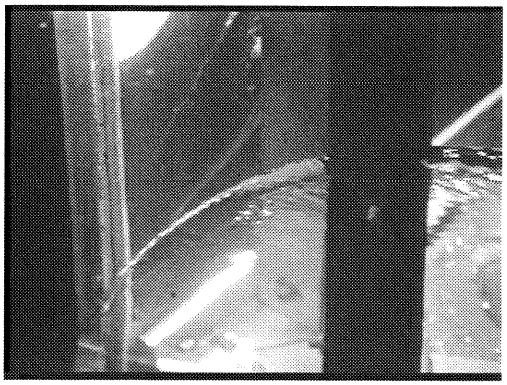

(a) Leading edge.

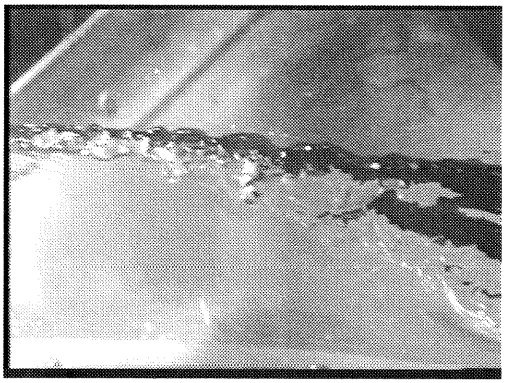

(b) Mid-wedge.

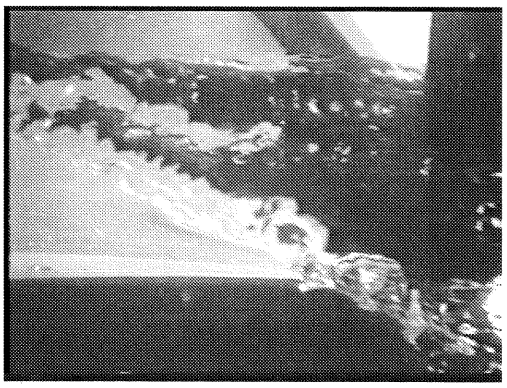

(c) Trailing edge.

Figure 4.23 Video of the surface disturbances observed in the towed wedge tests. The wedge is moving to the left and $\theta = 26°$, $\phi = 0°$, $U = 2.49$ m/s, $d = 7.54$ cm, and $\mathbf{F} = 2.90$.

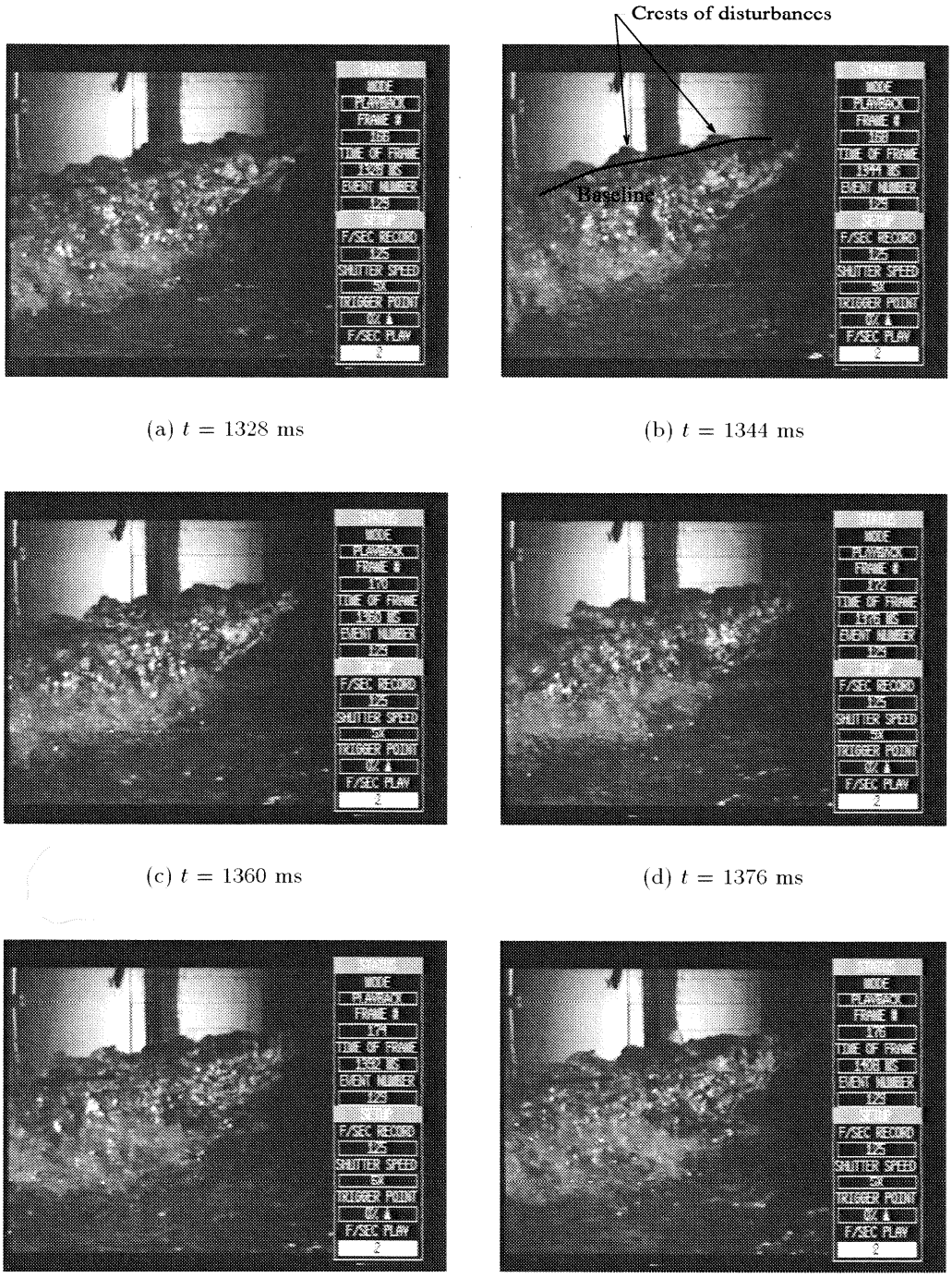

(a) t = 1328 ms

(b) t = 1344 ms

(c) t = 1360 ms

(d) t = 1376 ms

(e) t = 1392 ms

(f) t = 1408 ms

Figure 4.24 A sequence of frames from a high speed video of the surface disturbances at the trailing edge of the deflecting plate. The flow is from the right to the left, and the time is noted beneath each frame.

The trailing edge of the deflecting plate is visible in this view. The focal plane of the camera was the deflecting plate and the 5 cm square grid lines on the plate provided a length scale for the images. These videos were used to manually produce tracings of the movement of the surface disturbance crests along the wave profile baseline illustrated in Figure 4.24. Figure 4.25 is a typical tracing used to measure the characteristic length and velocity of the surface disturbances. The characteristic length was defined as the length of the surface disturbance at the wave profile baseline and is shown graphically in Figure 4.25. For flow conditions of $\mathbf{F} = 3.18$, $U = 2.64$ m/s, and $d = 7.1$ cm, the characteristic length ranged from 7 cm to 16 cm with a mean of 11 cm. The velocity was measured by dividing the distance traveled by a disturbance along the wave profile baseline by the time difference between two high speed video images. The average velocity of these disturbances was 2.42 m/s, approximately the velocity in the direction of the deflecting plate, namely 2.64cos(25°). Dividing the average velocity by the average characteristic length yields a characteristic frequency for these disturbances of 22 Hz.

The same high speed videos also were used to produce water surface time histories at two locations along the wave crest, and an example is shown in Figure 4.26. Although the resolution of these time histories is poor, both a lower frequency component and a higher frequency component can be observed. The lower frequency is approximately 1 Hz, though a longer sampling time is clearly needed to more accurately define this. It is possible that this lower frequency originates from the flow conditions in the 40 m flume. For example, the oscillation of the water in the upstream reservoir, the free over-fall into the downstream reservoir, and slug flow through the pump are all possible sources of this frequency. It is not caused by a "manometer" oscillation of the water in the flume because the "manometer" frequency, f, would be much lower. In fact, using

$$f = \frac{1}{2\pi}\sqrt{\frac{2g}{l}}$$

where l is the total length of the water column (about 40 m), f is 0.11 Hz. The higher frequency component, estimated by counting local maxima within fixed time intervals, was between 15 Hz and 20 Hz. This higher frequency appears to arise from the surface distur-

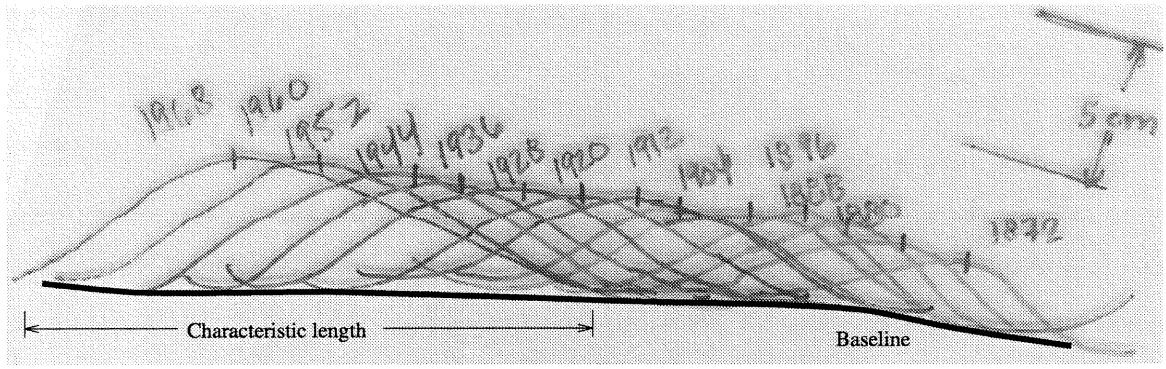

Figure 4.25 Tracing of a surface disturbance crest. The numbers correspond to the time (in ms) visible on each frame from the high speed video camera. The characteristic length for the disturbance at t = 1968 ms is indicated.

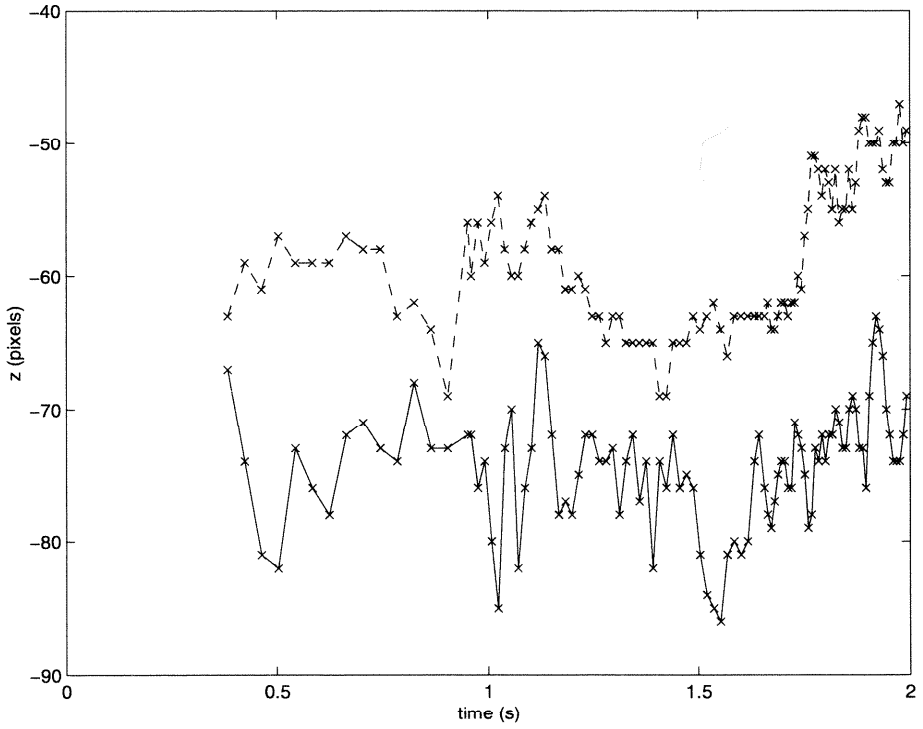

Figure 4.26 Water surface time histories for two locations along the surface of the deflecting plate; (- -) for r = 53.2 cm and (—) for r = 75.0 cm. The flow conditions were U = 2.64 m/s, d = 7.03 cm, $\mathbf{F}$ = 3.18, and $\theta = 25°$.

bances since it is similar to the frequency measured from the tracings such as in Figure 4.25.

4.7.3 Wave gage results

Three wave gages flush mounted on the surface of the deflecting plate were used to produce time histories of the free surface height at the plate surface; one wire pair wave gage was located in the upstream reservoir as well. The wave gage voltage signals were sampled at a rate of 100 Hz for 164 seconds, and post-processed using a fourth order Butterworth filter with a cutoff frequency of 50 Hz. Examples of the filtered voltage signals are shown in Figure 4.27. For this series of tests, the average flow velocity, U, was 2.69 m/s, and 2.44 m/s in the direction of the deflecting plate. However, since the liquid sheet is approximately 6 to 16 cm above the undisturbed free surface height, slightly lower velocities would be expected along the contact line and the wave crest. The steady Bernoulli's equation,

$$U_{contactline} = \sqrt{U^2 - 2gh_{contactline}},$$

predicts velocities which are lower by 10–25% (2.0 to 2.5 m/s) at the elevation of the contact line and the wave crest.

Autocorrelations of the signals show that they are periodic. The signals used for the autocorrelations were sampled at 2 kHz for eight seconds. For a length N vector, the auto-correlation c_{xx} was computed using MATLAB as follows:

$$c_{xx}(m) = \begin{cases} \sum_{n=0}^{N-|m|-1} x_{n+1} x^*_{n+m+1} & m \geq 0 \\ c^*_{xx}(-m) & m < 0. \end{cases}$$

Then $c(m) = c_{xx}(m - N)$ where $m = 1, ..., 2N - 1$ was plotted against the lag time in seconds. The time difference between the peaks in the autocorrelation function corresponds to the period of the major frequency contained in the signal. Figure 4.28 shows a typical autocorrelation result. The reservoir signal appears strongly periodic with a frequency of 1 Hz; a similar frequency is seen in the other signals. This supports the hypothesis that a flume induced frequency existed and contributed to the unsteadiness of the contact line.

Cross-correlations of signals from wave gage pairs were also computed. For a length N

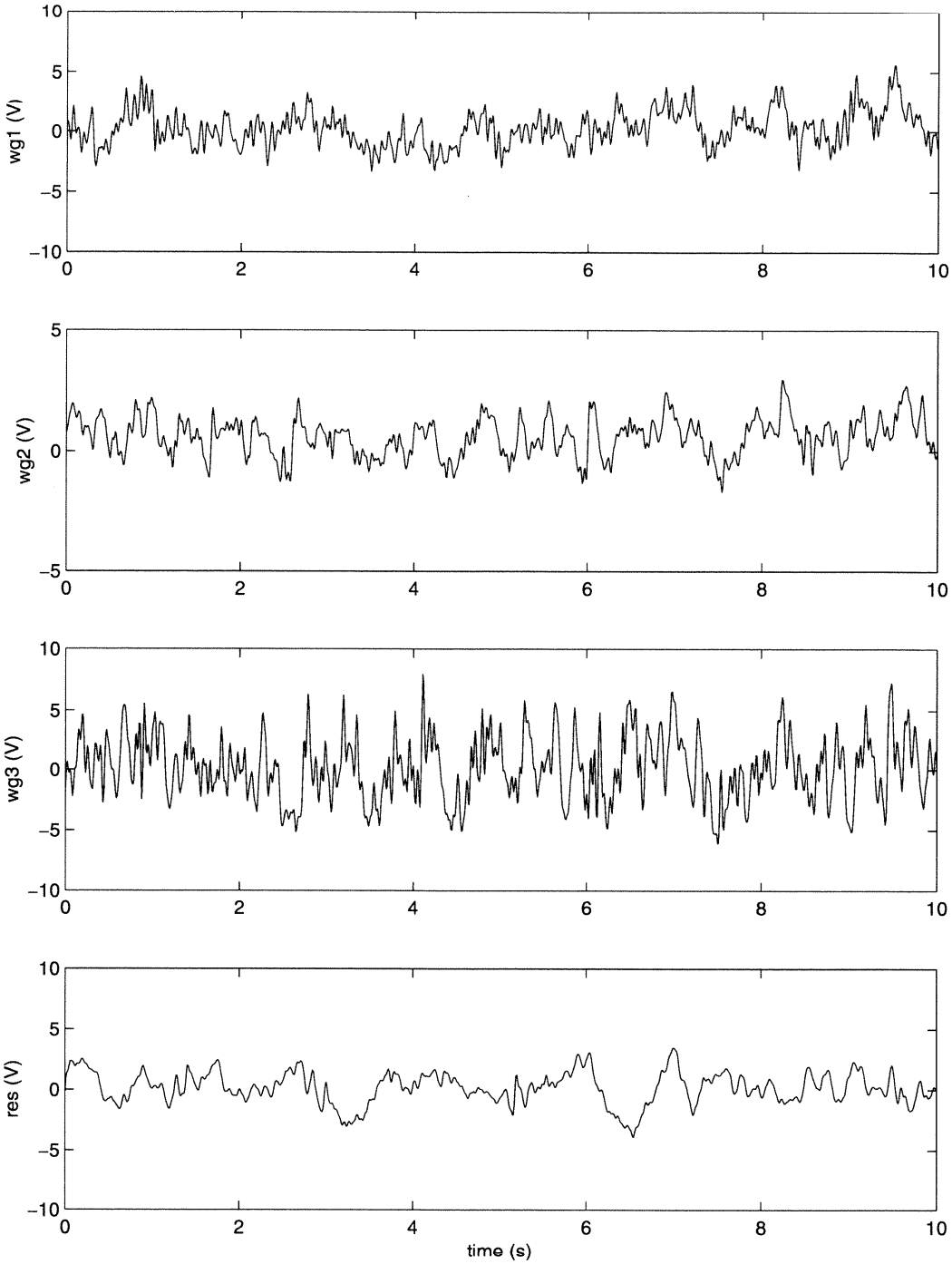

Figure 4.27 Typical wave gage signals from three wave gages flush mounted on the deflecting plate. Wave gage 1 (wg1) is 2.5 cm downstream of the leading edge, wave gage 2 (wg2) is 20 cm downstream of the leading edge, and wave gage 3 (wg3) is 40 cm downstream of the leading edge. The reservoir wave gage (res) is located in the upstream reservoir of the 40 m flume. For these tests: $\theta \approx 26°$, $\phi = 0°$, $U = 2.69$ m/s, $d = 7.18$ cm, and $\mathbf{F} = 3.21$.

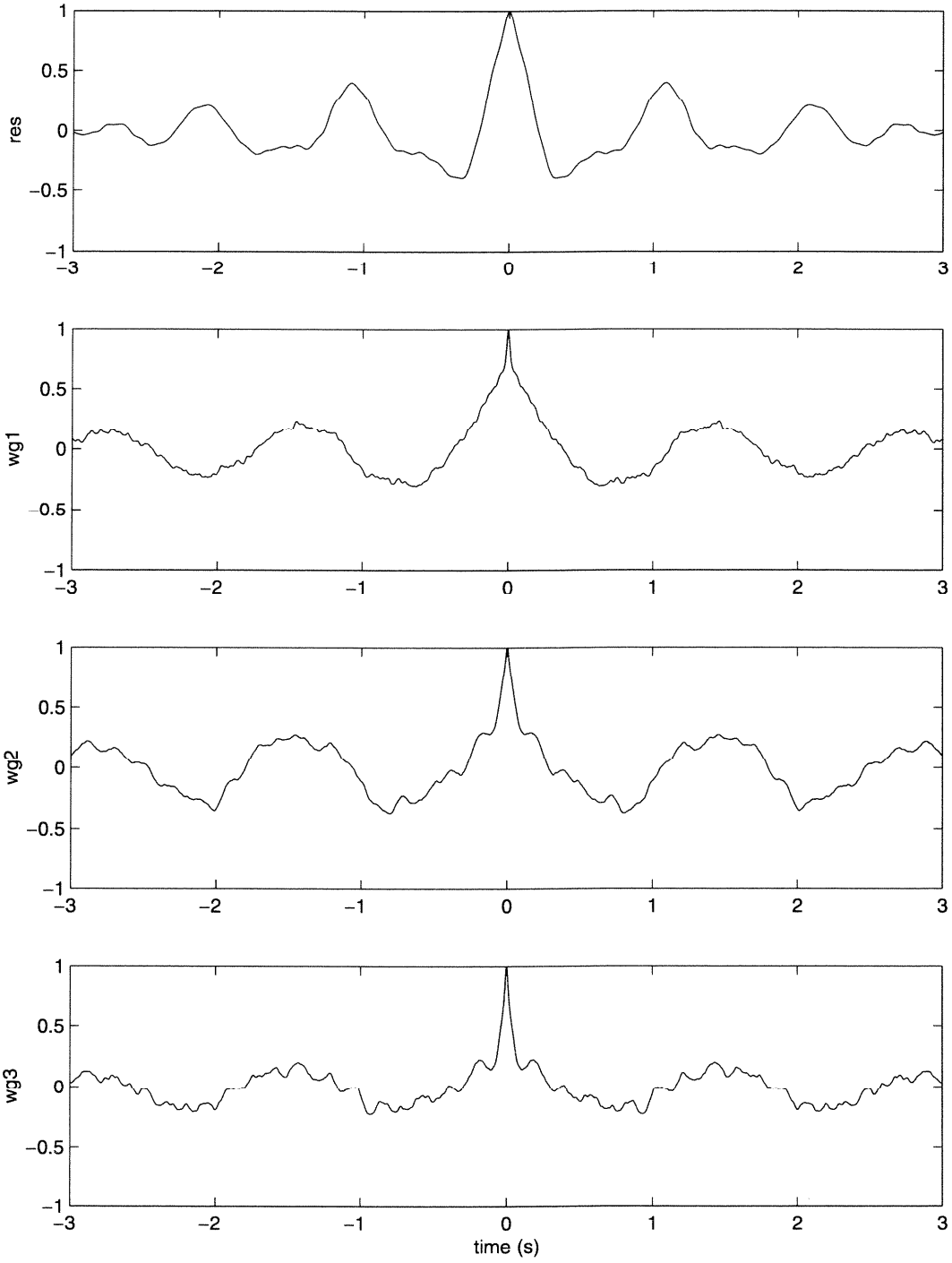

Figure 4.28 Typical autocorrelations from three wave gages flush mounted on the deflecting plate (wg1, wg2, wg3) and the reservoir wave gage (res). For these tests: $\theta \approx 26°$, $\phi = 0°$, $U = 2.55$ m/s, $d = 7.37$ cm, and $\mathbf{F} = 3.00$.

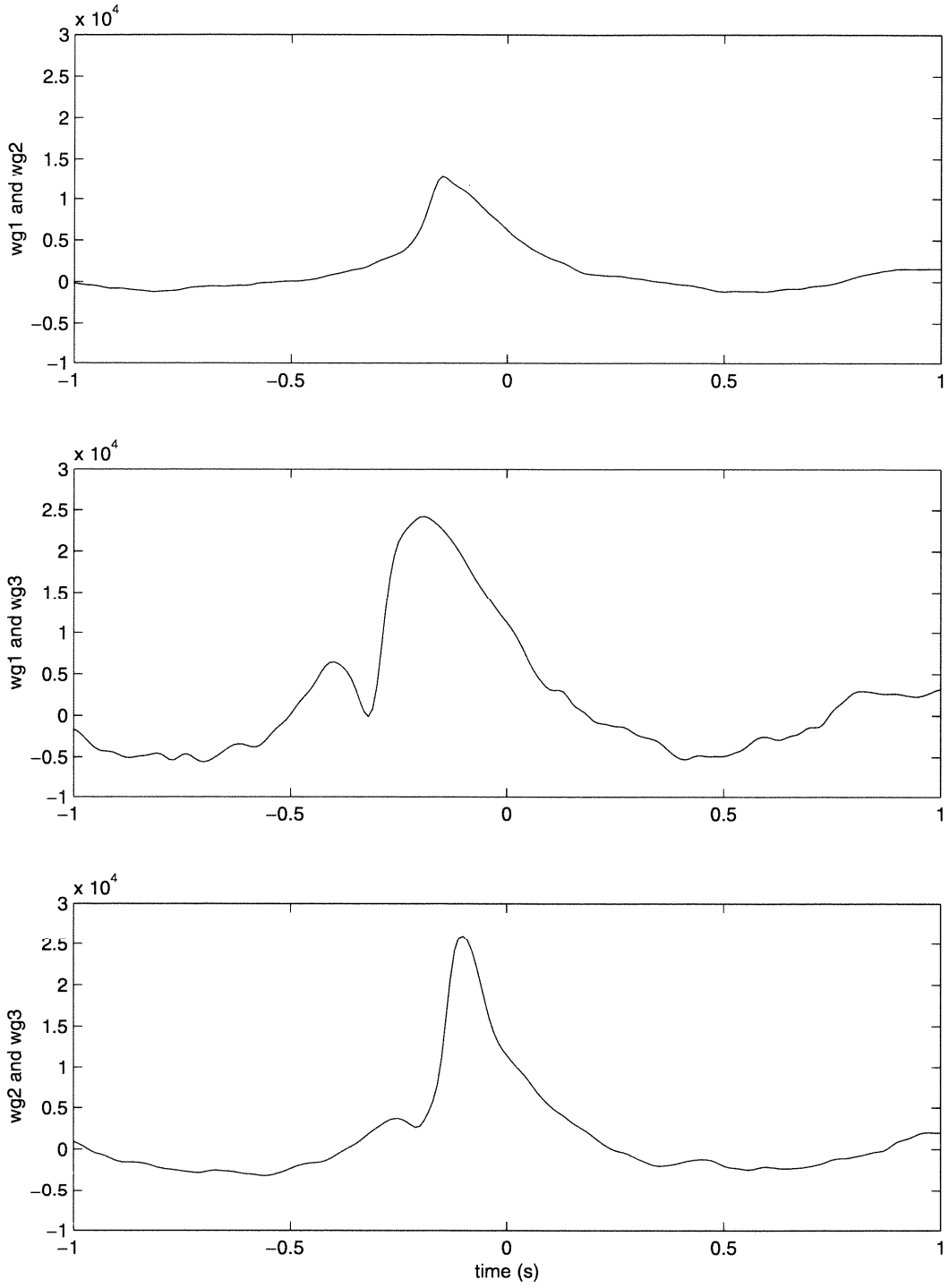

Figure 4.29 Cross-correlations for the signals from three wave gages flush mounted on the deflecting plate (wg1, wg2, and wg3) shown in Figure 4.27.

vector, the cross-correlation c_{xy} was computed using MATLAB as follows:

$$c_{xy} = \begin{cases} \sum_{n=0}^{N-|m|-1} x_{n+1} y^*_{n+m+1} & m \geq 0 \\ c^*_{xx}(-m) & m < 0. \end{cases}$$

Figure 4.29 shows $c(m) = c_{xy}(m - N)$ where $m = 1, ..., 2N - 1$ plotted against the lag time in seconds for the signals shown in Figure 4.27. The cross-correlations between gages 1 and 3 were the strongest. Most correlations showed two peaks; the first peak was occurred at an average of 0.186 sec and the second peak at about 0.4 sec. Using the distance between gages 1 and 3, namely 37.5 cm, this time lag corresponds to a velocity of 2.0 m/s. This velocity falls within the range expected in the earlier discussion, implying that the disturbances move along the face of the plunging wave at the flow velocity. Gages 2 and 3 also showed strong correlation with peaks at 0.10 sec. The distance between gages 2 and 3 is 20 cm which also yields a velocity of 2.0 m/s. The correlation between gages 1 and 3 is not as strong as would be expected since greater wave dispersion would occur over the larger distance.

The fast Fourier transforms (FFTs) of the signals were also calculated in MATLAB using:

$$X(k+1) = \sum_{n=0}^{N-1} x(n+1) e^{-j(2\pi/N)kn}$$

where $X(k+1)$ is a vector of complex numbers. Both the real and imaginary parts were scaled by the root mean squared value of the signal, V_{rms}, where

$$V_{rms} = \sqrt{\frac{\sum_{i=1}^{N} (x_i - \overline{x})}{N}}.$$

The real and imaginary parts were averaged separately over a number of data runs and then the number of frequencies represented on the FFT was reduced by a factor of eight to obtain a smoother curve. Figure 4.30 presents the averaged, smoothed FFTs for five samples taken with the same flow conditions.

Figure 4.30(b) shows a peak common to the three wave gage signals and the reservoir signal around 1 Hz. As previously discussed, it is believed that this frequency is caused by

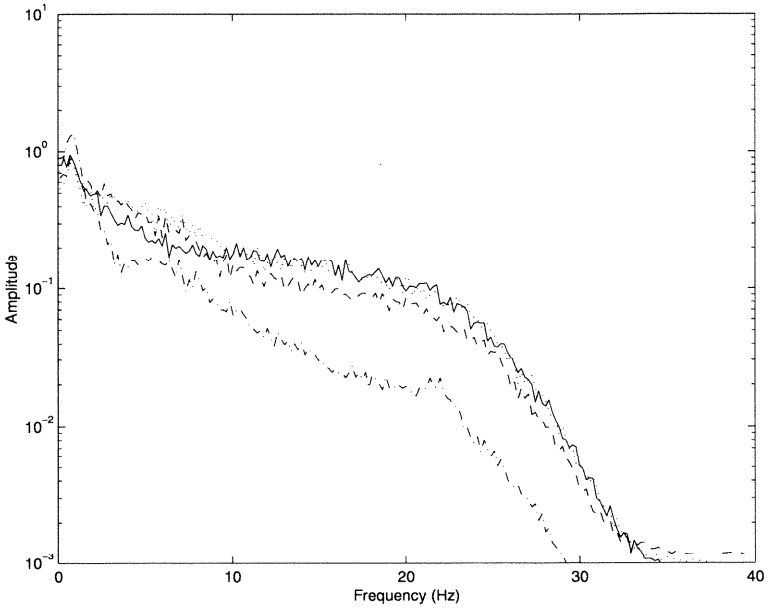

(a) Entire frequency range.

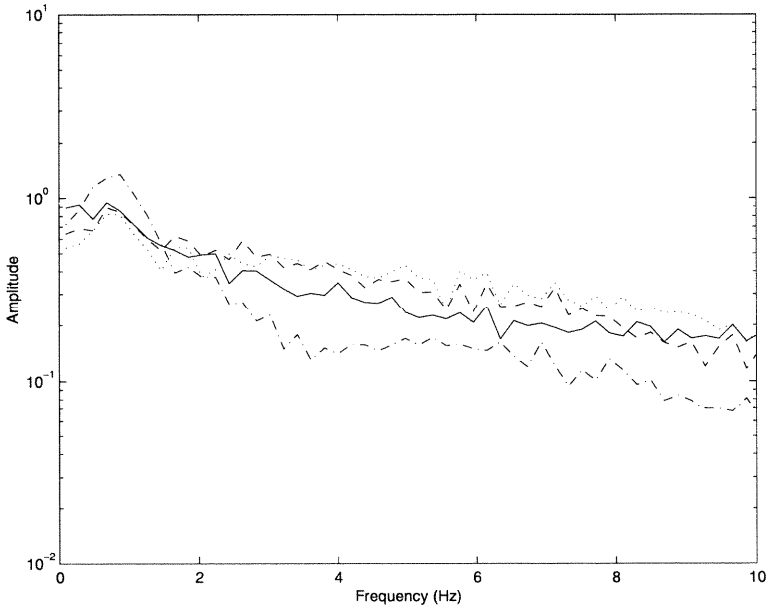

(b) Reduced frequency (and amplitude) range.

Figure 4.30 Averaged fast Fourier transform over five data runs for the flow conditions listed in Figure 4.27. Each line represents data from a different gage: (- -) for wg1, (–) for wg2, (· · ·) for wg3, and (- ·) for res.

Measurement technique	From high speed video camera?	Measurement location	Frequency (Hz)	Velocity (m/s)	Characteristic length (cm)
Tracings of disturbances	Yes	Bow wave	22	2.42	7–16
Water surface time histories	Yes	Bow wave	1, 15–20	N/A	N/A
Electronic wave gages	No	Deflecting plate	1, 10–25	2.0	8–20

Table 4.3 Summary of results from the different measurement techniques used to study the surface disturbances observed on the bow wave.

the flow conditions and is present throughout the 40 m flume. Additionally, Figure 4.30(a) clearly shows a difference in the frequency content of the signals from the reservoir and the three wave gages on the plate. The spectra from the wave gages show greater energy and a more uniform distribution of energy between 10 and 25 Hz than the spectrum from the reservoir gage. It is believed that this frequency range corresponds to the surface disturbances. Using this frequency range and the velocity calculated from the wave gage correlations, a range of characteristic lengths for the disturbances was found to be 8 cm to 20 cm.

4.7.4 Comparison of high speed video and wave gage results

Table 4.3 summarizes the measurements of frequency, velocity, and characteristic length for the surface disturbances using the two techniques on the bow wave and using the wave gages on the plate. All techniques yielded similar results, a 1 Hz frequency induced by flow conditions and higher frequencies from the surface disturbances. The agreement between the results from the tracings of the surface disturbances and the results from the wave gages is strong, suggesting the periodicity in the contact line elevation recorded by the wave gages reflects the periodicity of the surface disturbances. Furthermore, since the 20 Hz surface disturbance frequency was an order of magnitude greater than the 1 Hz flow induced frequency, the flow induced frequency probably did not interfere with or distort these periodic flow structures.

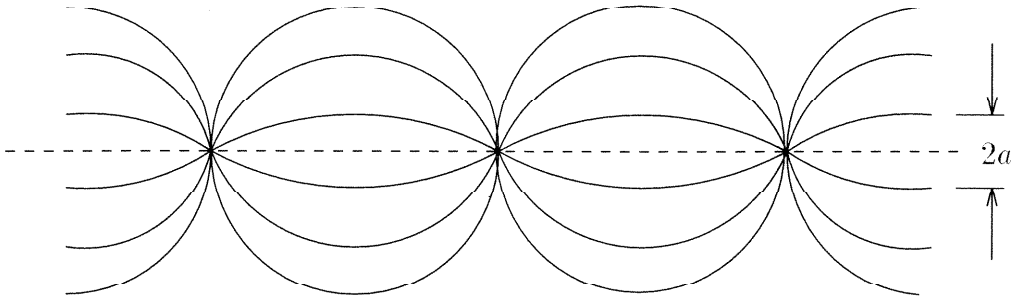

Figure 4.31 Schematic diagram of a plunging wave jet cross section disintegrating into "cylindrical drops". Reproduced from Longuet-Higgins (1995).

4.7.5 Discussion of surface disturbances

Similar surface disturbances were also observed in the towed model experiments; therefore, they must originate from an instability in the flow as it passes over the deflecting plate rather than from the upstream flow in the stationary model experiments, and we would expect to see them on "real" bow waves. Observations of instabilities developing in flows moving across a solid surface are not unique. For example, Shroff and Liepmann [44] reported two-dimensional instabilities on a water sheet which developed as the sheet moved over a curved solid surface and persisted even after the sheet left the surface.

We postulate that the crests of the surface disturbances are simply crests of gravity waves which propagate across the bow wave oriented as shown in Figure 4.22. Longuet-Higgens [29] analytically describes a similar situation in his discussion of the disintegration of the jet in a plunging breaker. He begins by assuming a perturbation in the form of short surface waves, or gravity waves, which propagate across the jet surface perpendicular to the plunging jet direction. As the wave breaks and the jet stretches, the pressure gradient in the jet direction decreases and the fluid is in a state of free-fall. This causes the perturbation waves to transition from gravity to capillary waves, and this transition increases their amplitude by a factor of 1.23–3.40. In the case of perturbations symmetric on both sides of the jet, Longuet-Higgins found that they will grow again (relative to the jet thickness) as the jet is

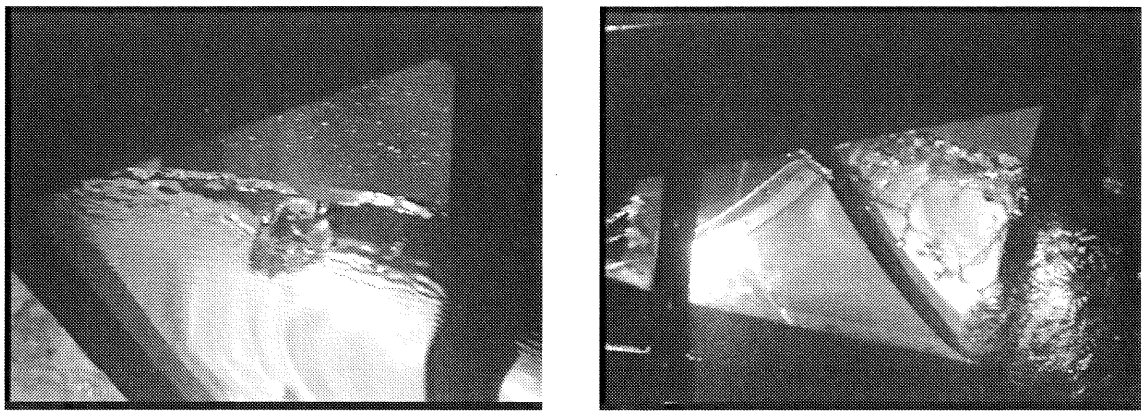

(a) Formation of a single drop.

(b) Formation of several strings of droplets.

Figure 4.32 Video of the breakup of the plunging wave jet into drops in the towed model experiments. The wedge is moving to the left and $\theta = 26°$, $\phi = 0°$, $U = 2.99$ m/s, $d = 25.14$ cm, and $\mathbf{F} = 1.91$. Note the extreme surface disturbances.

stretched even further according to

$$\frac{a}{h} \propto h^{-1/4}$$

where a is the perturbation amplitude and h is the jet thickness. Finally, he assumes that these perturbations will grow large enough to pinch the sheet into "cylindrical drops" and notes that the sheet would not pinch off in the same way for anti-symmetric perturbations. This disintegration is shown in Figure 4.31, though in actuality the jet represented by a dashed line in the figure would have some finite thickness.

This hypothesis and discussion are a plausible explanation for the breakup of the plunging wave jet by the surface disturbances, though further investigation clearly is required. In the present experiments, strings of droplets similiar to Longuet-Higgins' "cylindrical drops" were seen to form on the edge of the plunging wave jet as in the photographs in Figure 4.3(a) and Figure 4.32. It seems that the size and spacing of the strings of droplets could be controlled by the size of the surface disturbances.

Chapter 5

Air Entrainment

The primary mechanisms for air entrainment in the present bow wave experiments were the plunging wave jet and the entry of individual droplets from the splash region after the initial impact of the plunging wave jet. Since the plunging wave jet entrained much greater quantities of air than the splash droplets, only the plunging wave jet was studied. A discussion of air entrainment by the impact of drops on liquid surfaces may be found in Prosperetti and Oguz [42]. This chapter presents a qualitative description of this air entrainment process followed by experimental void fraction and bubble size measurements. Because of the shallow depth in these experiments, the data describes the initial stages of air entrainment only.

5.1 Experimental observations

The air entrainment process for the simulated bow wave could be observed best in a darkened room using a stroboscope which provided a high intensity and short duration (0.5 μs) light pulse. The lamp had a parabolic reflector which directed a 7.6 cm diameter beam of light through the window in the bottom of the test section shown in Figure 2.3. Observations of the bubbles were made through the glass sidewall of the flume. The most obvious feature was that the plunging wave jet entrained air in "bursts" forming approximately spherical clouds of bubbles visible beneath the free surface. This observation seems similar to an observation by Chanson and Cummings [13] regarding air entrained by a planar supported jet. For high jet impact velocities (4–8 m/s) they reported a thin layer of air entering the flow

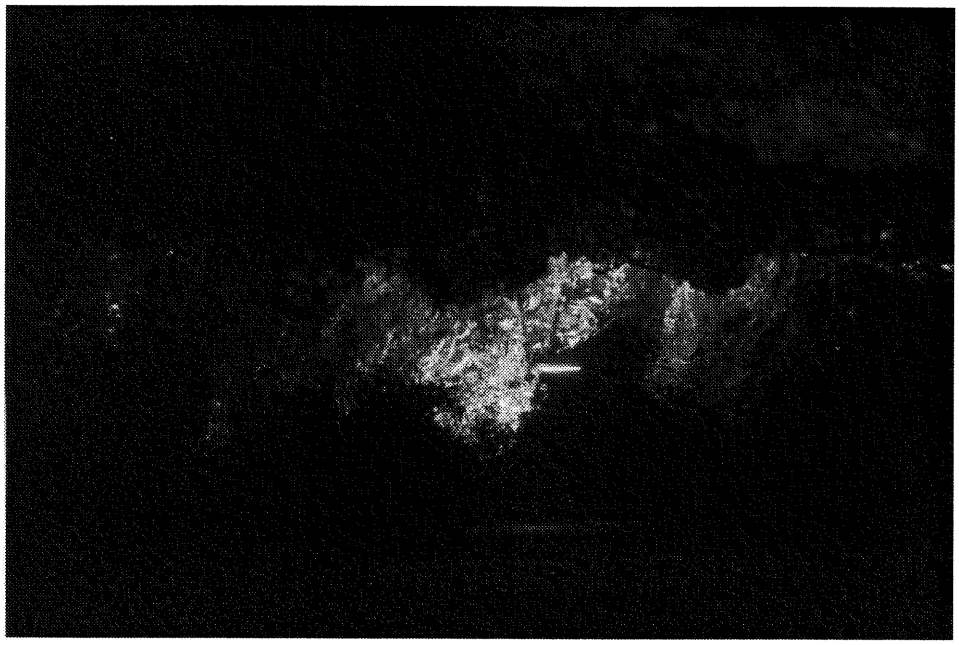

(a) IVFM probe tip with bubble clouds.

(b) Several bubble clouds. The splash above the free surface is also visible.

Figure 5.1 Photographs of bubble clouds passing by the IVFM probe. The flow is from right to left and the probe is located beneath the impacting wave jet; $\theta = 25°$, $\phi = 0°$, $U = 2.47$ m/s, $d = 7.39$ cm, and $\mathbf{F} = 2.90$.

at the impact point, adding that the "air pockets are entrained by discontinuous gusts at the lower end of the air layer." In the present experiments, the bubble clouds had a diameter of about 5 to 10 cm and were comprised of bubbles which were more tightly packed at the center of the cloud than at the edges. Moreover, the formation of these clouds was periodic in a spatial sense, i.e., a chain of bubble clouds could be observed beneath the free surface at any particular moment in time. Typical photographs of bubble clouds are shown in Figure 5.1. Photographs of individual bubbles within the bubble clouds were obtained using a telephoto lens, and though most of the bubbles appeared to be 1 to 5 mm in diameter, large finger-like pockets of air also were observed. Finally, in the experimental configuration used in this research, the clouds seemed to grow in size as they were convected downstream. This growth proceeded at a steady rate until the clouds encountered the bottom and/or opposite wall of the flume. If the flume depth were unlimited, the depth of bubble entrainment might well approach the wave height observed by Cipriano and Blanchard [15] in their plunging wave experiments.

5.2 Experimental measurements

The observations described in the preceding section were quantified using the impedance based void fraction meter (IVFM) described in section 2.2.3. For measurements in the simulated bow wave, the IVFM probe was mounted on the carriage as shown in Figure 2.4. Samples were taken at different cross sections in the impact line region of the flow; one section where measurements were made is illustrated in Figure 5.2. A typical example is given in Figure 5.3.

A preliminary series of experiments was performed to verify the IVFM signal. The IVFM signal was sampled at 2 kHz, and simultaneous images using a high speed video (500 fps) of the bubble clouds were obtained. The stroboscope described in section 5.1 was triggered by the video camera, and illuminated the field of view of the camera. The resulting IVFM signals were compared carefully with the high speed video, and typical correlations for two different void fractions are shown in Figures 5.4(a) and (b). In each of the two graphs, the lower signal is from the IVFM. The upper signal was created from the high speed video

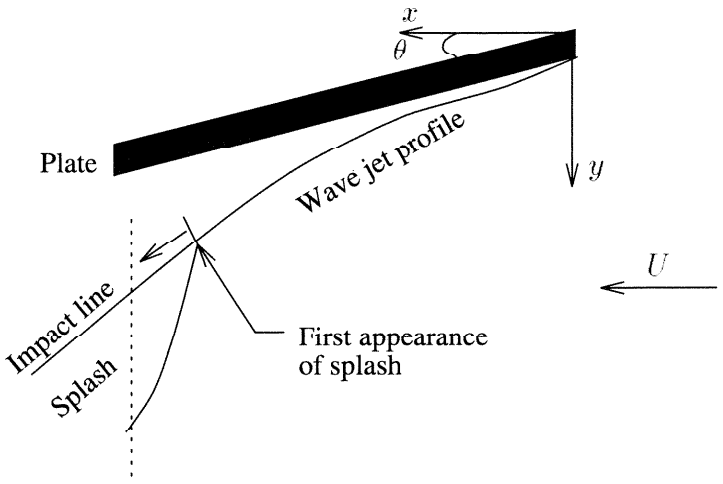

Figure 5.2 Schematic diagram of the planform of the flow with a typical flow cross section $(\cdots)$ indicated where measurements were made.

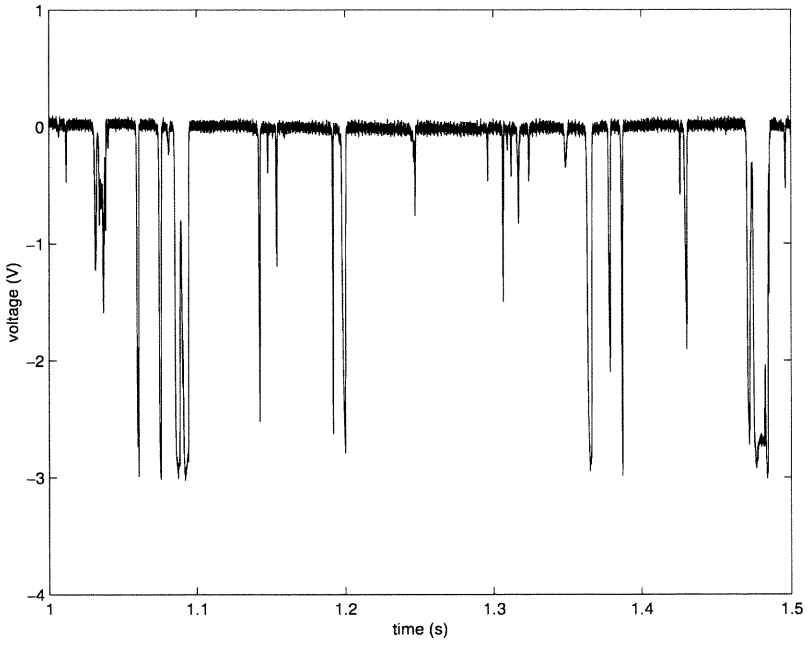

Figure 5.3 A portion of a typical signal from the IVFM located several centimeters beneath the bow wave jet; $\theta = 26°$, $U = 2.39$ m/s, $d = 6.47$ cm, and $\mathbf{F} = 3.00$. Using the calibration curve, the time averaged void fraction, $\alpha = 6.5\%$.

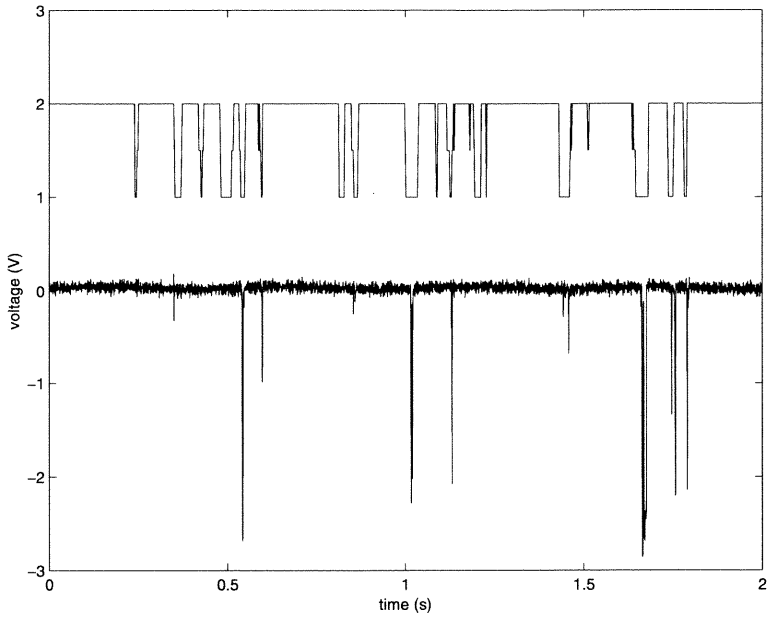

(a) Signals for z = -3.5 cm.

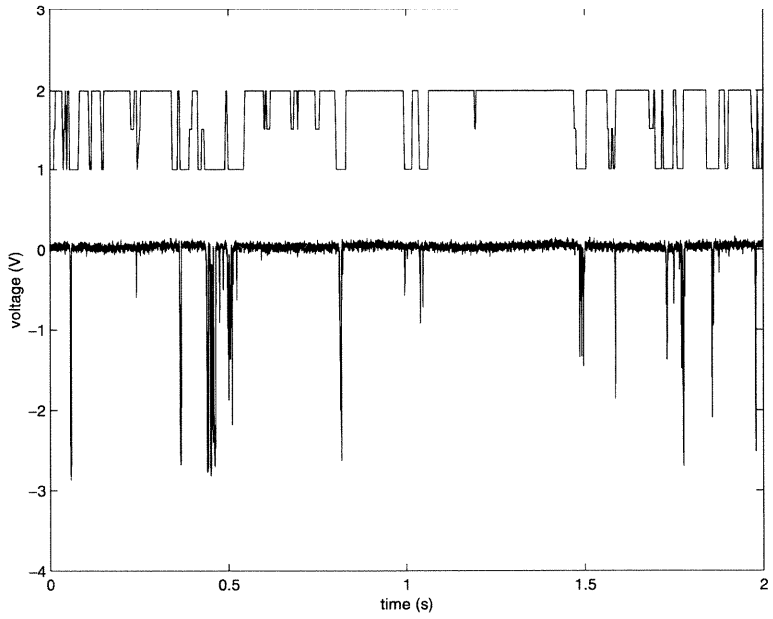

(b) Signals for z = -4.5 cm.

Figure 5.4 Correlation of IVFM signal with high speed video of bubble clouds for two different locations beneath the free surface at the same position. The lower signal is from the IVFM, and the upper signal was created from high speed video observations.

observations by assigning a value of two when no bubbles were seen on the probe tip and a value of one when bubbles were observed to be touching the probe tip.

The correlation between the two signals was as follows. Every spike in the IVFM signal corresponded to a bubble impacting the probe tip; however, the signal generated from the high speed video shows additional spikes that are not present in the IVFM signal. This discrepancy is attributed to a combination of several effects. First, since a beam of light illuminated the probe, some bubbles in the video appeared to be contacting the probe but were not, in fact, in the plane of the probe. This resulted in excess spikes in the high speed video signal. Second, the sampling rate of 2 kHz was low enough to miss spikes created by bubbles striking the probe. A direct collision with a 1 mm diameter bubble moving at 2.39 m/s would produce a spike of 0.0024 sec in duration. Sampling at 2 kHz, every 0.0005 sec, would give a maximum of four samples per spike. This rate would not be high enough for indirect collisions and collisions with smaller bubbles. Third, since the void fraction of the clouds was low, there was a possibility that a cloud could pass by the probe without a single bubble impacting the tip. For example, consider a 3.5 cm diameter bubble cloud with a void fraction of 5% comprised of uniformly distributed 1 mm diameter bubbles. If the center of this cloud passed by the probe, only ten bubbles would be expected to impact the probe tip. If the edge of the cloud passed the probe or if the cloud void fraction was lower, even fewer impacts would be expected to occur. In summary, the discrepancy between the IVFM and the high speed video signals was somewhat expected; however, there is confidence that the IVFM responds to impacts with individual bubbles in the flow.

5.2.1 Bubble cloud void fraction measurements

For void fraction measurements in the simulated bow wave, the IVFM signals were sampled at 20 kHz for 3.2 sec. Note that this higher sampling rate was used to avoid the problems described in the previous section. The signals were then processed as described in section 2.2.3. The calibration shown in Figure 2.22 with a threshold of -0.75 V was applied to obtain the local, time-averaged void fraction. A set of nine IVFM signals from the same location beneath the bow wave had a mean void fraction of 3.2% and a standard deviation of 0.8%. This indicated that the results were repeatable; therefore, for the rest of

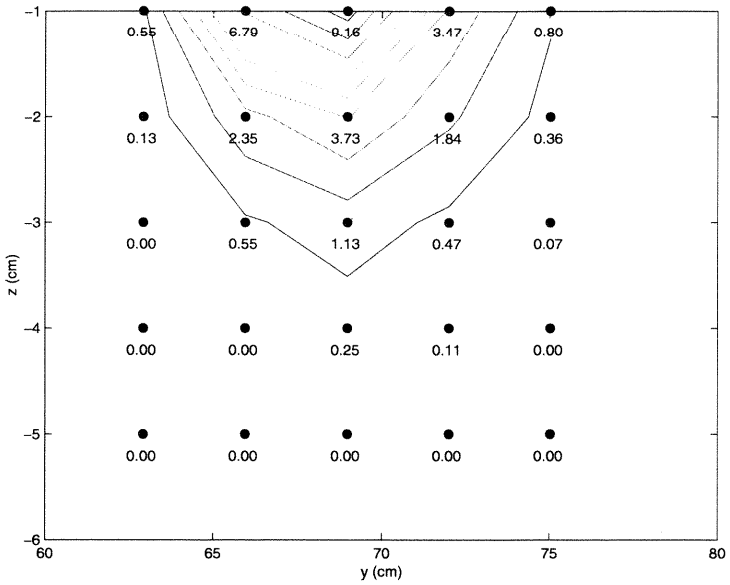

Figure 5.5 Local time averaged void fraction cross section for $x = 91.2$ cm as viewed from downstream beneath the breaking wave; $\theta = 26°$, $\phi = 0°$, $U = 2.48$ m/s, $d = 7.89$ cm, and $\mathbf{F} = 2.82$. The IVFM measurement locations are marked (•) and labeled with the void fraction %. Nine equally spaced contour levels between $\alpha = 1\%$ and $\alpha = 9\%$ are shown, with $\alpha = 1\%$ on the outer edge of the bubble cloud.

the experiments the measurement was repeated three times for each location and the mean reported.

An example of time averaged, ensemble averaged, void fraction data for a flow cross section in the impact region of the plunging wave jet is shown in Figure 5.5. The leading edge of the deflecting plate is located at $(x, y) = (0, 0)$ and the upstream free surface is located at $z = 0$. Void fraction contours calculated from the data highlight the trends in void fraction. Because the free surface was unsteady, it was not possible to estimate void fractions at locations above z = -1 cm without the free surface dipping below the probe or the probe entraining air when near the free surface. In addition to these problems, there is typically a surface effect on the impedance for this type of void fraction instrumentation. Lamarre and Melville [26] reported that when the free surface was too close (about 2 cm) to the measuring volume, the void fraction measured by their instrument was electrically biased by the free surface. In the present experiments, however, the surface effect problem was less significant than the physical problems of air entrainment.

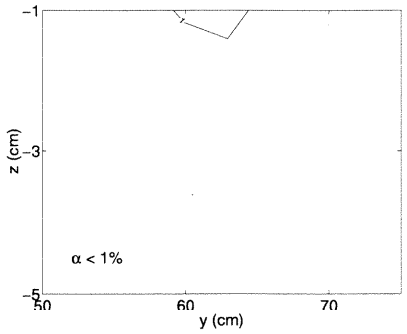

(a) $x = 73.4$ cm; plunging wave jet impacts at $y \approx 63$ cm.

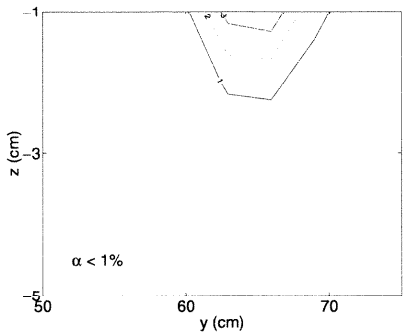

(b) $x = 81.0$ cm; plunging wave jet impacts at $y \approx 65$ cm.

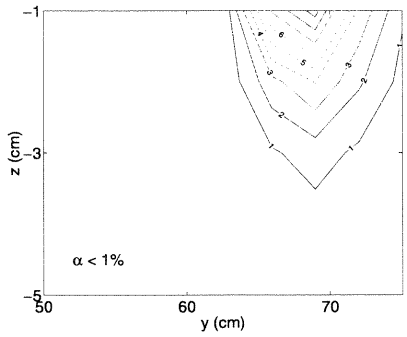

(c) $x = 91.2$ cm; plunging wave jet impacts at $y \approx 69$ cm.

Figure 5.6 Local time averaged void fraction for three different flow cross sections as viewed from downstream beneath the breaking wave for the flow conditions specified in Figure 5.5. Ten equally spaced contour levels between $\alpha = 1\%$ and $\alpha = 10\%$ are shown, with $\alpha = 1\%$ on the outer edge of the bubble cloud.

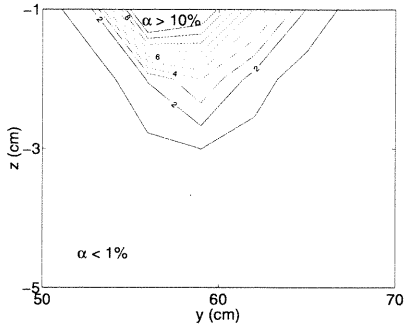

(a) $x = 70.8$ cm; plunging wave jet impacts at $y \approx 56$ cm.

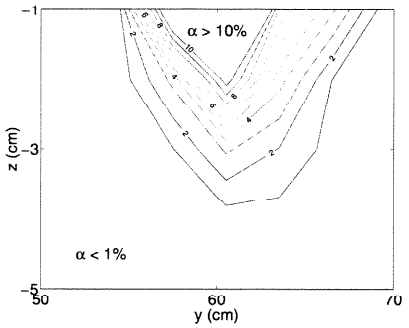

(b) $x = 75.9$ cm; plunging wave jet impacts at $y \approx 60$ cm.

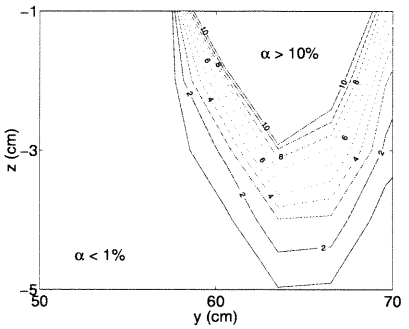

(c) $x = 84.2$ cm; plunging wave jet impacts at $y \approx 64$ cm.

Figure 5.7 Local time averaged void fraction for three different flow cross sections as viewed from downstream beneath the breaking wave, for $\theta = 26°$, $\phi = 0°$, $U = 2.39$ m/s, $d = 6.47$ cm, and $\mathbf{F} = 3.00$. Ten equally spaced contour levels between $\alpha = 1\%$ and $\alpha = 10\%$ are shown, with $\alpha = 1\%$ on the outer edge of the bubble cloud.

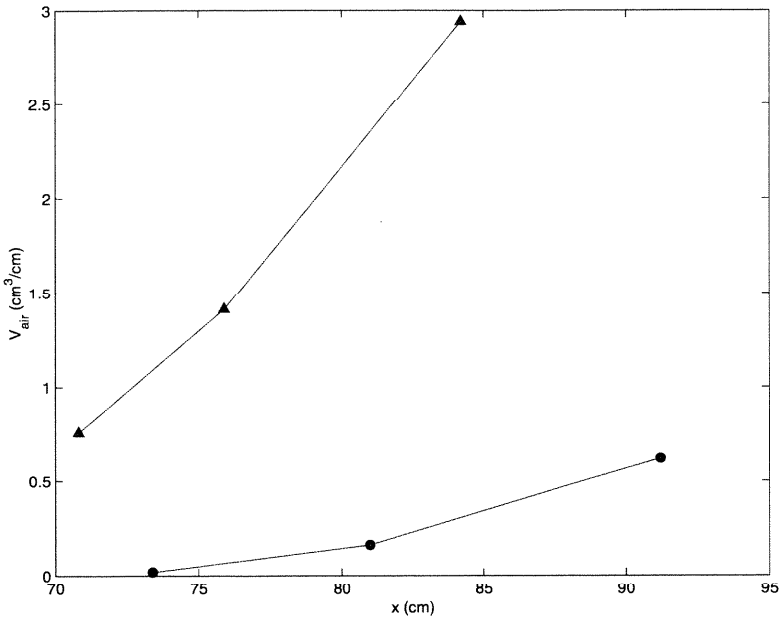

Figure 5.8 Total volume of air entrained per unit length as a function of streamwise location; (●) for the flow cross sections shown in Figure 5.6 and (▲) for the flow cross sections shown in Figure 5.7.

Figures 5.6 and 5.7 show the void fraction contours for sets of flow cross sections. On average, the sampling grids for the cross sections shown in these figures contained 20 locations and the individual void fraction measurements are included in Appendix C. Figures 5.6 and 5.7 confirm observations from the high speed video. First, the bubble clouds are shown to be roughly circular in cross section and grow as they convect downstream. Second, the greater void fractions at the center of the cloud support the observation that the bubbles are more tightly packed at the cloud center than at the edges.

The void fraction mappings also were used to calculate the total volume of air entrained at particular streamwise locations. The areas between pairs of consecutive void fraction contours, $A_{i+1} - A_i$, were calculated and multiplied by the void fraction in those regions. The summation of these terms gave the total volume of air per unit length, V_{air}, where

$$V_{air} = \sum_{i=1}^{n} \frac{1}{2}(\alpha_i + \alpha_{i+1})(A_{i+1} - A_i)$$

and n was the number of void fraction contours. Note that this calculation yields a con-

servative estimate of the amount of air entrained, since the void fraction was greater than 10% for some regions of the cloud and could not be measured. The results for the mappings shown in Figures 5.6 and 5.7 are included in Figure 5.8.

The data clearly shows that the quantity of air contained in the bubble clouds increases with the distance downstream for both flow conditions; however, since the location of the impact line changes with flow conditions, V_{air} was very different for a given streamwise position, x. In Figure 5.8, the data points marked by circles were taken in a higher velocity flow and the location of the impact line was further downstream. Therefore, the volume of air entrained in this flow was much less even though the measurements were made at similar streamwise locations. It would be possible to shift these curves by plotting V_{air} as a function of the distance from the impact line origin, but the location of the impact line origin unfortunately was not recorded in these experiments. If void fraction mappings were produced for the entire length of the impact line, the void fraction could be expressed as a function of distance along the impact line and the total volume of air entrained by the wave could be calculated by integration of this function.

5.2.2 Bubble cloud bubble size distributions

The same IVFM signals were used to produce bubble size distributions for the bubbles which comprised the bubble clouds. The typical dimension of the individual bubbles was represented by a quantity called the bubble chord, l. Bubble chords were calculated by multiplying the individual spike base widths, ΔT, from the IVFM signals by the mean flow velocity, or $l = U\Delta T$. Note that for very small bubbles this chord should be close to the bubble diameter since they will remain spherical. This calculation is similar to bubble chord calculations for a dual tip conductivity probe described by Chanson [11]. Figure 5.9 shows three separate measurements of the bubble chord distributions at the same location beneath the bow wave. The bin size was 2 mm, for example, the count rate for bubble chords between 10 and 12 mm is represented by the group of bars centered about 10 on the abscissa. These results demonstrate the repeatability of this measurement technique.

Figures 5.10, 5.11, and 5.12 include averaged size distributions for bubble clouds that passed through the cross section shown in Figure 5.7(b) for the same flow conditions. The

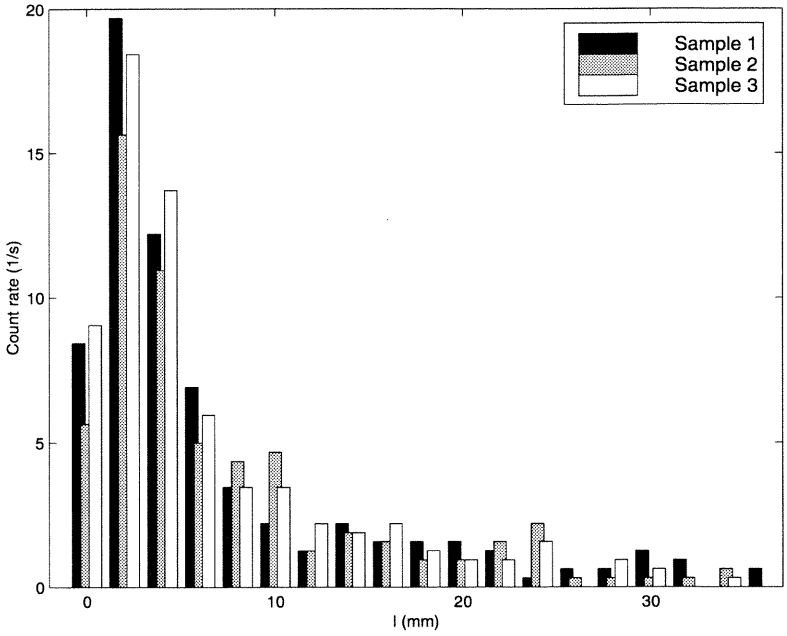

Figure 5.9 Bubble chord distributions from bubble clouds observed beneath the breaking wave at x = 75.9 cm, y = 66.6 cm, and z = -1.0 cm. The bin size is 2 mm, and the flow conditions are the same as those listed in Figure 5.7.

bin size is 2 mm, and the plunging wave jet impacts at $y \approx 60$ cm. As mentioned earlier, these distribution data were limited by the depth of water in the flume; distributions at depths greater than z = -4 cm were affected by the bottom. For this reason, the distribution data are confined to locations nearer to the free surface. These figures show that most bubble chords were 1 to 7 mm (consistent with high speed video observations of the size of the individual bubbles), and the number of bubbles in this size range increased from the edge to the center of the cloud and from the bottom to the top of the cloud. In addition, larger pockets of air existed in the center of the cloud near the free surface, giving rise to the larger bubble chords registered at those locations. The larger pockets of air did not persist in the clouds; they were either broken up into smaller bubbles by the turbulent flow or rose to the free surface. The center of the cloud, the region with greatest void fraction, was located directly beneath the impacting plunging wave jet.

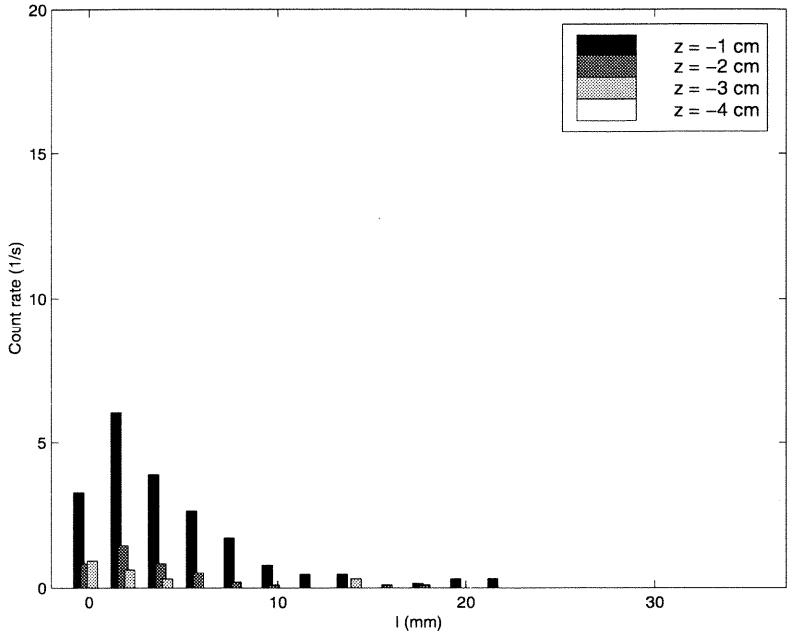

Figure 5.10 Bubble chord distributions from bubble clouds observed beneath the breaking wave at $x = 75.9$ cm and $y = 66.6$ cm for different depths.

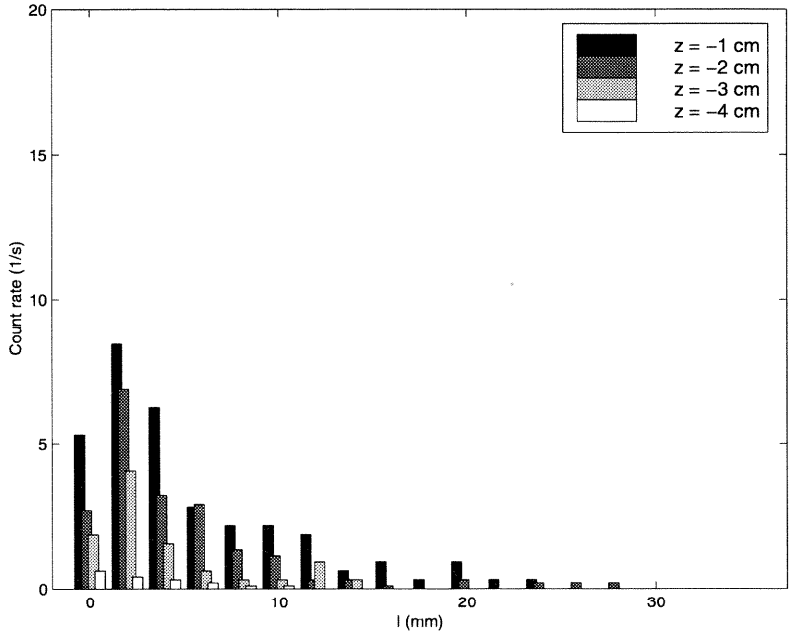

Figure 5.11 Bubble chord distributions from bubble clouds observed beneath the breaking wave at $x = 75.9$ cm and $y = 63.5$ cm for different depths.

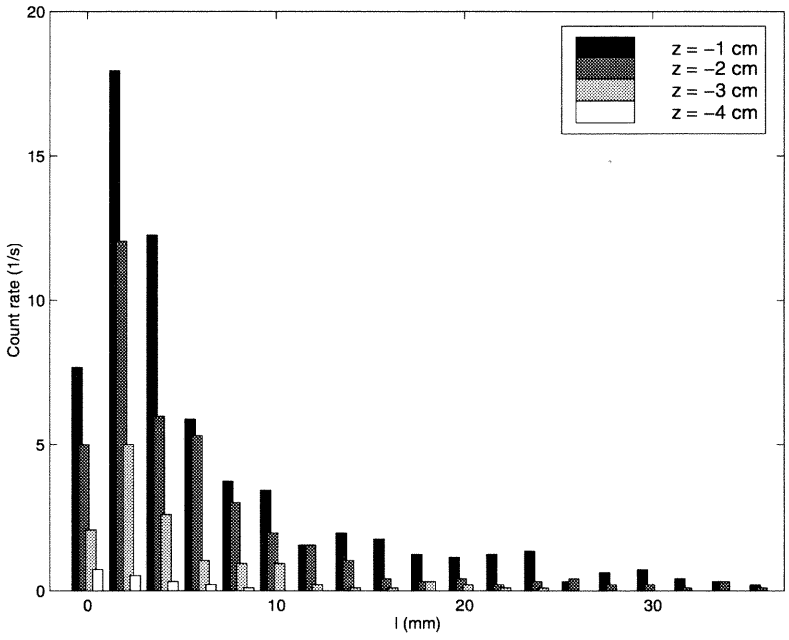

Figure 5.12 Bubble chord distributions from bubble clouds observed beneath the breaking wave at $x = 75.9$ cm and $y = 60.5$ cm for different depths.

5.2.3 Frequency of bubble cloud encounters

As described in section 5.1, the formation of the bubble clouds was observed to be spatially periodic. Since the clouds convect downstream with the mean flow velocity, they would pass a particular location at some rate or frequency. Initially, high speed video of the bubble clouds was used to estimate the frequency of cloud encounters with the IVFM probe which was located a few centimeters beneath the plunging wave jet. Each frame of the video was examined, and it was noted whether or not a bubble cloud was present at the probe tip. This method was somewhat subjective, i.e., are a few bubbles near the probe tip considered a bubble cloud? Frequencies of cloud encounters for videos of flow conditions similar to those in Figure 5.3 were between 7 and 14 Hz.

A signal processing technique was implemented to extract the same information from the IVFM signals, namely the frequency of bubble cloud encounters with the void fraction probe. The technique was implemented as follows. First, it was assumed that two bubbles located 1 cm or less apart belong to the same bubble cloud since the cloud cross sections were about 10 cm in diameter. If the two bubbles are separated by 1 cm in the streamwise direction and they move at the mean flow velocity, U, then there would be a time delay of $0.01/U$ seconds between the two bubbles as they impacted the IVFM probe tip. The IVFM signal was processed using an algorithm which searched for successive spikes caused by individual bubble impacts occurring within this time delay. Figure 5.13 shows the result of this cloud detection algorithm for a typical IVFM signal. The lower graph shows the reciprocal of the time delay, or frequency of individual bubble impacts with the IVFM probe, as a function of time. To count the clouds, a particular individual bubble impact frequency was chosen as a threshold. Since the mean flow velocity was 2.39 m/s, a threshold of 200 s^{-1} implied that two bubbles belonging to the same cloud could have had a maximum separation distance of 1.2 cm. This threshold is also shown in the lower graph, and a cloud was counted for each local maximum greater than 200. Note that this technique does not count bubble clouds for which only a single bubble impacted the probe tip; therefore, it gives a conservative estimate for the frequency of bubble cloud encounters.

Figure 5.14 plots the frequency of bubble cloud encounters as a function of depth using three samples for each location. The signal processing technique is responsible for the

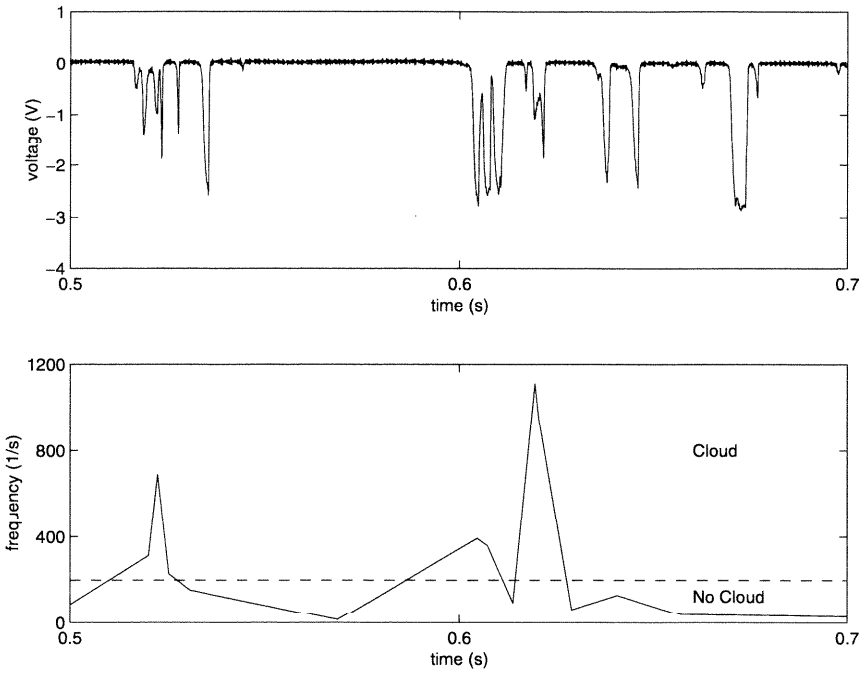

Figure 5.13 Detail of signal processing technique; top: raw IVFM signal, bottom: cloud detection algorithm output (frequency of individual bubble impacts) from the IVFM signal shown here.

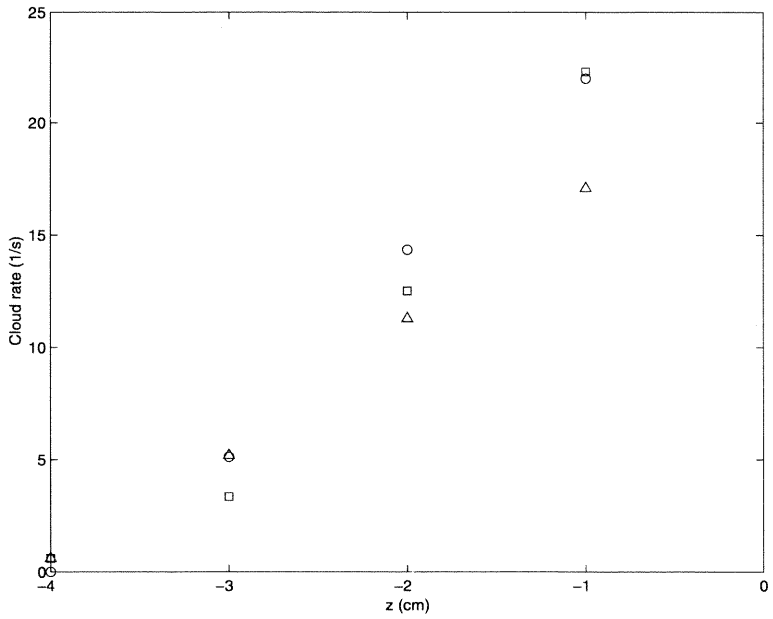

Figure 5.14 Variation in the bubble cloud encounter frequency at location $x = 75.9$ cm and $y = 60.5$ cm for the flow conditions in Figure 5.3.

apparent decrease in the frequency of bubble cloud encounters with depth. Since the bottom edge of the bubble clouds was lower in void fraction, there was a greater chance at larger depths that only a single bubble would impact the IVFM probe and the algorithm would not count the cloud (especially because the threshold remained constant for all locations). Figure 5.14 shows that the scatter in the data increases in regions of the flow with higher void fractions, but otherwise gives fairly repeatable results. These frequencies of bubble cloud encounters are similar to those mentioned earlier from the high speed video. When compared with the frequency of impact by individual bubbles on the IVFM probe, the number of individual bubble impacts per cloud was calculated to be between three and five for each depth. In summary, this signal processing technique works quite well as a method of bubble cloud detection particularly for regions nearer the free surface where the number of bubble impacts with the IVFM is the greatest.

5.3 Cross-correlation of IVFM and wave gage signals

Observations of the air entrained by the bow wave created in the larger scale stationary model experiments and the roughness of the free surface of the wave led to the hypothesis that the periodicity of the bubble clouds was related to the periodicity of the surface disturbances on the plunging face of the wave. Ideally, to test this hypothesis, a signal from the disturbances immediately before impact would be correlated with a signal which represented the formation of a bubble cloud; however, the wave gage voltage signals on the deflecting plate were correlated with the IVFM voltage signals instead. Recall from Table 4.3 that the signals obtained using flush-mounted wave gages on the deflecting plate appear to reflect the surface disturbance characteristics measured using high speed video.

Figure 5.15 shows a typical set of raw signals from the larger scale stationary model experiments sampled at 2 kHz. The location of wave gage 2 (wg2) was: x = 18.1 cm and y = 8.45 cm or r = 20.0 cm, the location of wave gage 3 (wg3) was: x = 36.3 cm and y = 16.9 cm or r = 40.0 cm, and the IVFM probe was located at: x = 107 cm, y = 52 cm, and z = -2.5 cm. The time-averaged void fraction in this region was 7.92%. The fast Fourier transforms (FFTs) of the signals are shown in Figure 5.16. Figure 5.17 plots the normalized

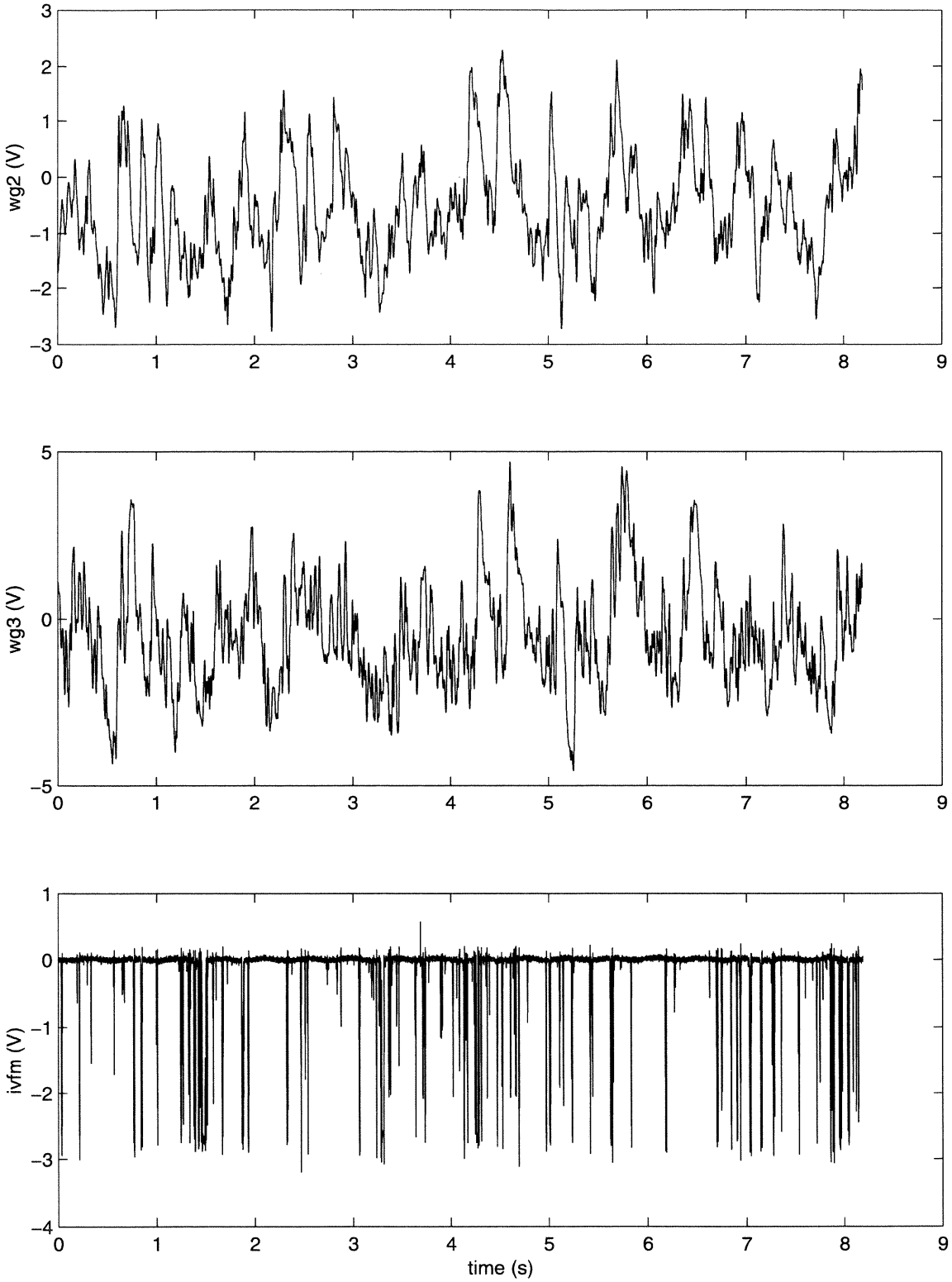

Figure 5.15 Raw voltage signals from the wave gages and the IVFM. The flow conditions were: $\theta = 25°$, $\phi = 0°$, $U = 2.56$ m/s, $d = 7.65$ cm, and $\mathbf{F} = 2.96$.

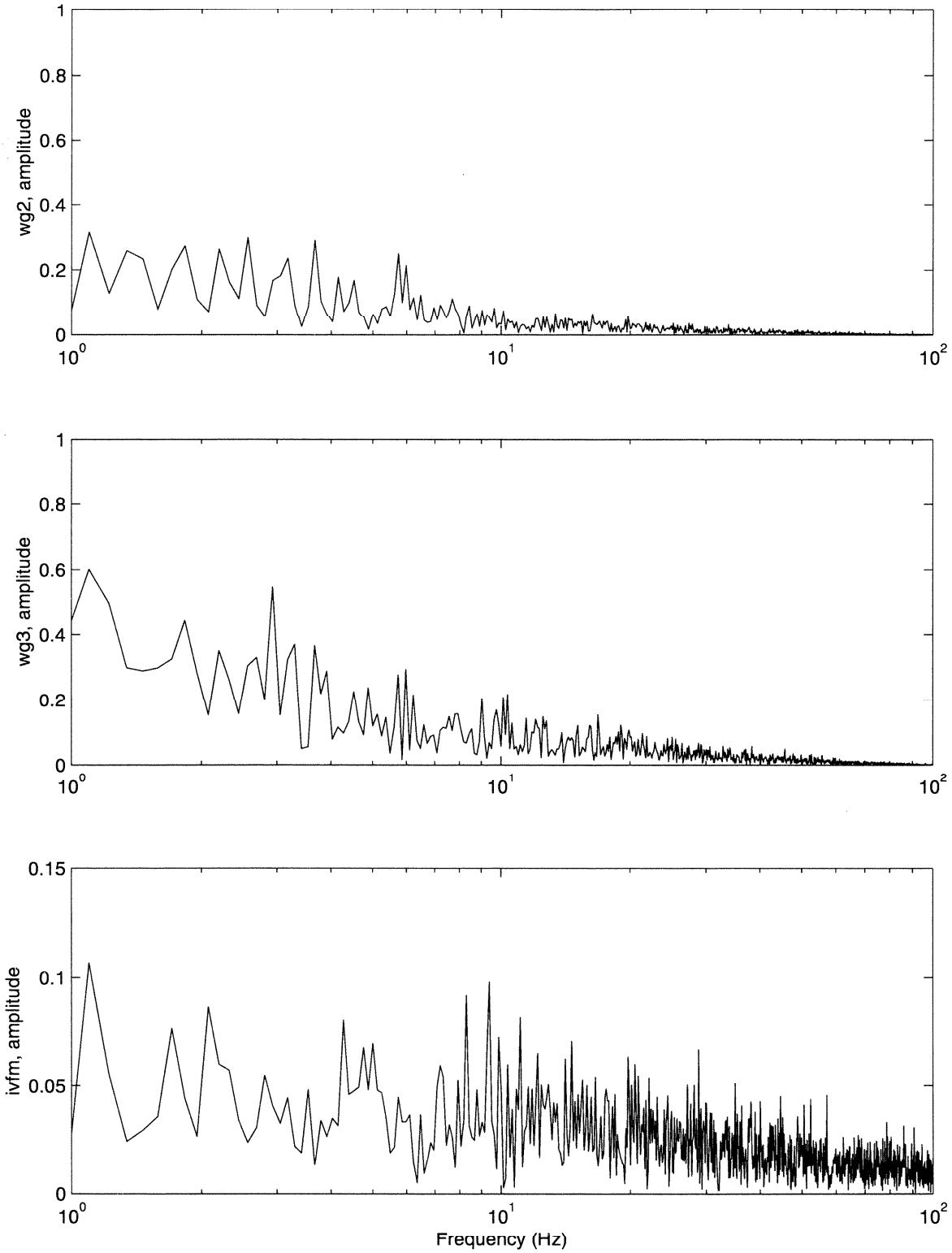

Figure 5.16 Normalized fast Fourier transforms of the filtered and detrended signals shown in Figure 5.15.

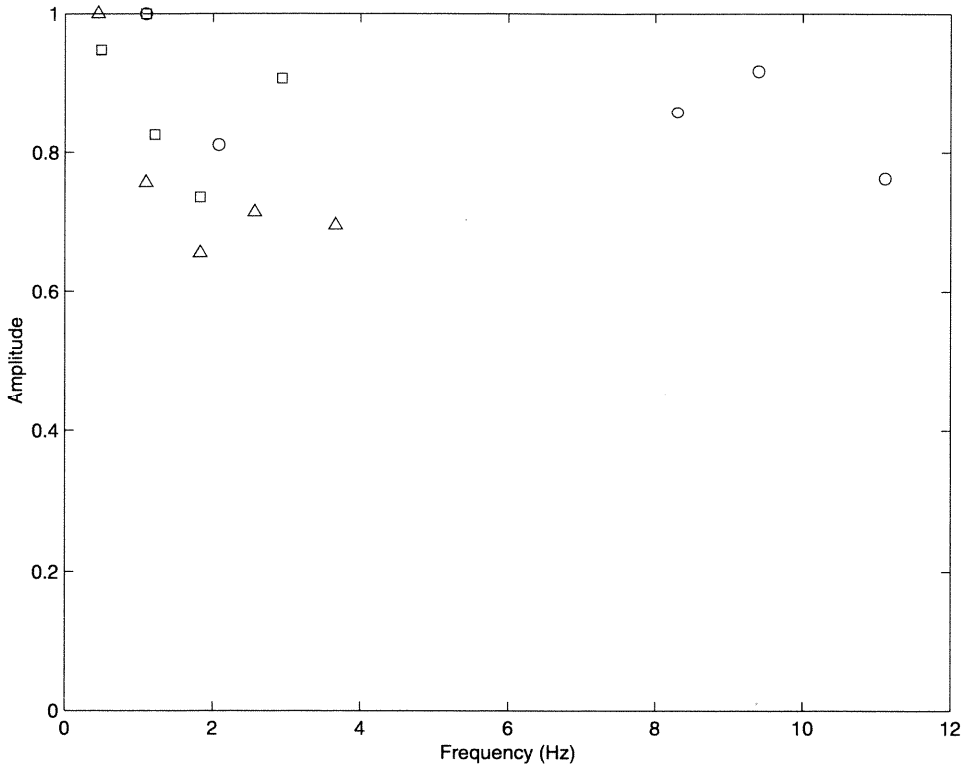

Figure 5.17 Dominant frequencies in signals shown in Figure 5.15; (○) for IVFM, (△) for wg2, and (□) for wg3.

amplitude for five dominant frequencies for each signal.

Figure 5.18 shows the cross-correlations for these same signals, and Figure 5.18 shows the same cross-correlations with a reduced abscissal range. The first positive cross-correlation peak occurred at 0.166 sec for wave gage 2 and the IVFM, and the first positive cross-correlation peak occurred at 0.055 sec for wave gage 3 and the IVFM. To understand the reason for these cross-correlation peaks, a velocity was calculated using the straight line distance between a wave gage and the IVFM and dividing by the time of the cross-correlation peak. For example, wave gage 2 and the IVFM were 96 cm apart and had a cross-correlation peak at 0.166 sec giving a velocity of 5.78 m/s. At first this velocity may seem alarmingly high; however, recall that the surface disturbances exist along the entire plunging face of the wave. These disturbances do not *travel* from the deflecting plate to the impact location, and calculating a velocity in this direction is incorrect.

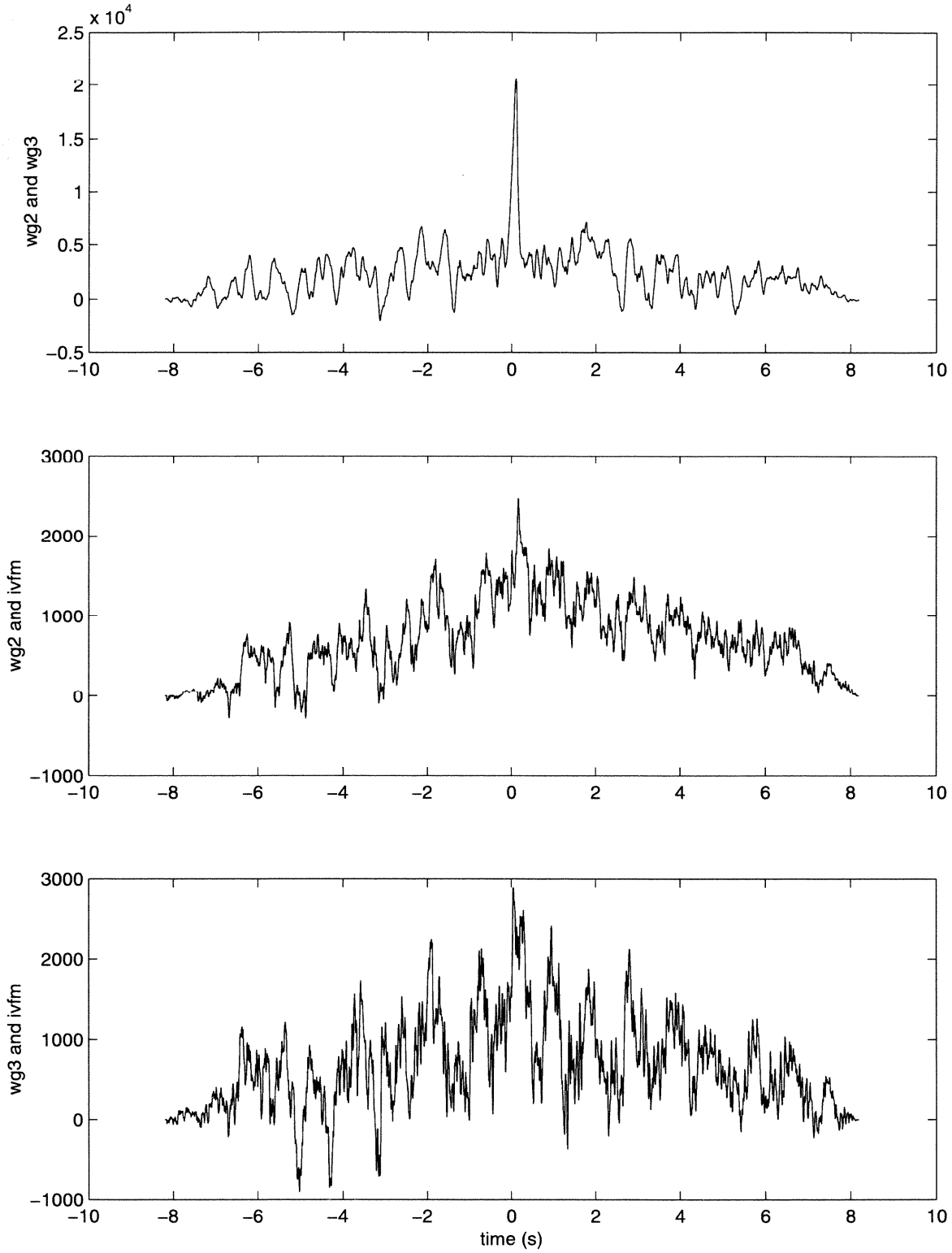

Figure 5.18 Cross-correlation results for the signals shown in Figure 5.15.

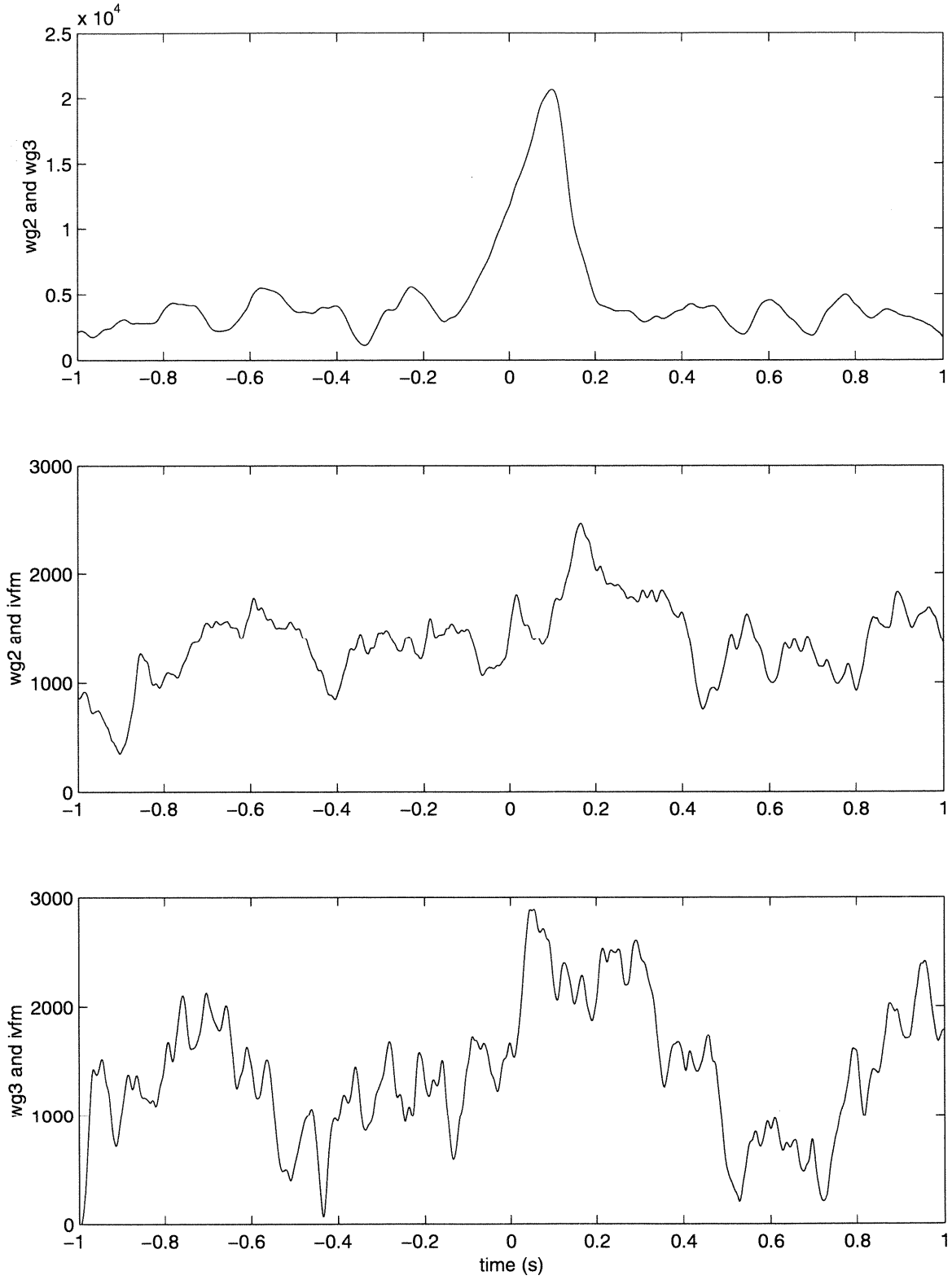

Figure 5.19 Cross-correlation results shown in Figure 5.18 with a reduced abscissal range.

Instead, we examine the structure apparent in the correlations presented in Figure 5.18. Local maxima occur at regular intervals; for example, in the cross-correlation for wave gage 3 and the IVFM there are 22 local maxima in the range 0–2 seconds. This indicates that the two signals have a common frequency component of 11 Hz which could be the frequency of the disturbances and bubble clouds. In conclusion, the cross-correlations show some positive indications of a relationship between the disturbances measured on the deflecting plate and the bubble clouds.

5.4 Discussion of bubble cloud formation

Surface disturbances exist on the plunging face of the breaking wave because of a flow instability, and each surface disturbance observed on the plunging face of the bow wave appears similar to an individual plunging jet. It is possible for the surface disturbance amplitude to grow to the point where it breaks the jet into strings of droplets before impact. As discussed in section 4.7, this series of individual plunging wave jets convects downstream with the mean flow velocity and each plunging wave jet entrains air at the point where it impacts the free surface. Observations of the bubble clouds beneath the free surface show small bubble clouds formed at the first location where the plunging wave jet impacts the free surface. These clouds grow in size (observed in high speed video and measured by IVFM) and increase in void fraction (measured by IVFM) as they convect downstream in a direction which follows the impact line of the wave.

On the basis of these observations, a mechanism for air entrainment is proposed and shown schematically in Figure 5.20. Each of the individual plunging wave jets entrains air into its own bubble cloud. These jet-cloud pairs convect downstream with the mean flow velocity; therefore, the distance between successive surface disturbances determines the distance between bubble clouds. It follows that dividing the mean flow velocity by the spacing between the disturbances (or bubble clouds) would give the same frequency, about 20 Hz for the present experiments. In addition, the void fraction increases with downstream distance since over a longer distance a jet would have more time to entrain air. Furthermore, the increase in cloud size with downstream distance could be explained either by diffusion

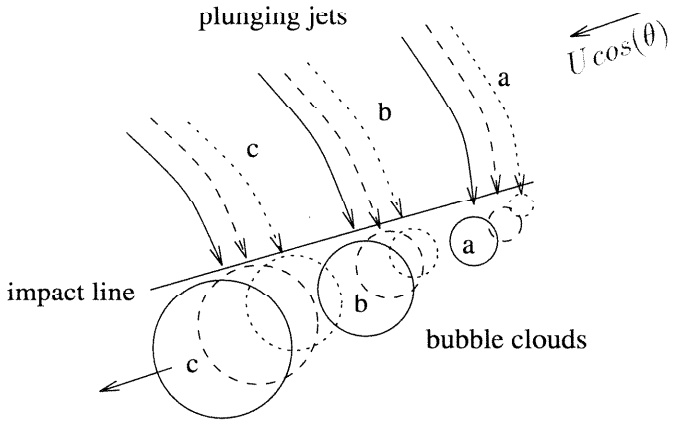

Figure 5.20 Schematic diagram of the proposed air entrainment mechanism. A time series of plunging jets and bubble clouds is depicted; $(\cdots)$ for $t = 0$, (- -) for $t = \Delta t$, and (—) for $t = 2\Delta t$.

or turbulent mixing of the bubbles in the flow, and/or by the growth in wavelength and amplitude of the surface disturbances with downstream distance.

It is very difficult to quantitatively correlate the surface disturbances with the bubble clouds, as demonstrated in the preceding section. Above the free surface, it is difficult to trace a surface disturbance to its exact impact location because the impact location is usually obscured by splash, and sometimes the jet breaks up into a string of droplets before it impacts. Below the free surface, the single IVFM probe could not track the movement of the bubble cloud. Multiple IVFM probes also would not be able to do this, because the downstream probe would not be able determine if it had seen the same cloud which had convected downstream a different cloud which had just formed in that location.

5.5 Two-phase flow models

As discussed in Chapter 1, more accurate models of the air entrainment process are needed to improve two-phase flow computations around surface ships. The air entrainment process enters into these problems in the form of a free surface boundary condition. For example, Carrica et al. [7] assumed that for an arbitrary area near the bow, a mixture of water and air with a void fraction of 10% entered the flow with a constant velocity directed vertically

downward. They further assumed the a bubble size distribution measured by Cartmill and Su [8] for bubbles created by a plunging jet in salt water.

It would be possible to use a more precise air entrainment boundary condition in modeling the two-phase flow for the present experiments. The location of the air entrainment would be along the impact line only, and the impact line could be measured using the free surface probes. Then, void fraction as a function of the distance along the impact line would be obtained from the IVFM data. A constant bubble size distribution from an average of experimental measurements would be used. Even though the size distributions were seen to vary with location in the experimental measurements, most of the bubble chords were between 1 and 7 mm. The velocity of these bubbles entering the flow at the free surface would be the same as that calculated for the plunging wave jet as described in section 4.5. As the model evolved, the periodicity observed in the bubble clouds also could be included.

Further study of scaling effects would be required before using these results in full scale two-phase flow computations. In addition, not all of the experimental results could be used since the full scale flows occur in salt water.

Chapter 6

Conclusions

This study of air entrainment by bow waves was motivated by the need for ship signature estimation in the field of naval hydrodynamics. Although there are many studies related to air entrainment in the literature, they concern different types of waves or simple plunging jets and there are no records of void fraction measurements beneath breaking bow waves. Since the air entrainment process is closely coupled with breaking wave dynamics [26], this study included both air entrainment and free surface measurements which described the features of the wave. The main conclusions of this work and ideas for future research are presented in this chapter.

6.1 Summary of thesis work

6.1.1 Free surface

Experimental measurements of the free surface were obtained from three-dimensional simulated bow waves in stationary model experiments at two scales and also from the bow wave created by a towed wedge model. The following major conclusions can be drawn regarding the free surface of the bow waves:

- *The contact line of the bow wave is highly non-linear.*
  Two different theoretical analyses of the contact line were performed and discussed in Chapter 3. The first approach was an extension of Ogilvie's [39] slender body theory in which there is a finite depth equal to the draft. This approach essentially linearized

in the y-direction, and it underestimated wave height by an order of magnitude. A second approach considering perturbations of planar potential flow around a finite hull body was pursued instead, and it essentially linearized in the z-direction. It resulted in an expression for the contact line which was a power series in $\mathbf{F}^2$; therefore, the series required Froude number, $\mathbf{F} < 1$ to converge. Since bow waves occur under supercritical flow conditions, this solution is inappropriate. Also note that any linear theory would fail to predict the plunging wave jet. Other researchers [9, 47] have used a "2D+t", or two dimensions plus time, numerical approach for similar flows which may be suitable for the present problem.

- *Stationary model experiments with a depth equal to the draft produce bow waves similar to towed model experiments with finite draft and infinite depth for a given* $\mathbf{F}$.
  The contact line was measured using free surface probes in the smaller and larger scale stationary model experiments, and the bow wave profile was measured in the towed model and larger scale stationary model experiments. These experimental results and experimental results from towed wedge tests by Ogilvie [39] were compared and showed that the two types of experiments can produce similar waves.

- *The experimental data describing the bow wave shape scales with* $U^2 d^{1/2}$ *in the* z*-direction and with* $U^2 d^{-1.5}$ *in the* r*-direction.*
  Furthermore, dimensional analysis expressed these relationships by $\mathbf{F}^{1.5}d$ in the z-direction, and $\mathbf{F}^{7/3}Re^{-1/3}d$ in the r-direction. As discussed in Chapter 4, this scaling does not agree with any theoretical scaling reported in the literature and it is not clear that the upstream Reynolds number in the second expression is physically meaningful. Scaling with geometric parameters such as bow half angle and dihedral angle were investigated using contact line data, and it was found that the wave is only weakly dependent on dihedral angle and depends on the bow half angle according to a non-linear relationship.

- *Surface disturbances with crests oriented in the cross-stream direction exit on the plunging face of the bow wave.*
  The disturbances were observed in the smaller and larger scale stationary model ex-

periments and the towed model experiments, and we would expect to observe them in full scale flows as well. They were recorded using high speed video and appear to be related to measurements from wave gages flush-mounted on the deflecting plate in the larger scale stationary model experiments. These techniques showed that the disturbances had wavelengths which ranged from 7 to 16 cm, convected downstream with the flow velocity in the direction of the deflecting plate, and had a frequency of about 22 Hz. The disturbances are likely gravity waves on the surface of the bow wave. These symmetric perturbations grow as the plunging jet stretches toward the free surface (impact line) and seem ultimately responsible for the breakup of the jet into strings of droplets before impact.

6.1.2 Air entrainment

The primary mechanisms for air entrainment in the present bow wave experiments were the plunging wave jet and the entry of individual droplets from the splash region. Observations of the air entrainment process were made in the larger scale stationary model experiments using a high speed video camera with a synchronized strobe lamp. Due to the shallow depth in the experiments, measurements of the larger bubbles in only the initial stages of air entrainment were studied, though it is well known that smaller bubbles persist in ship wakes for large distances. An impedance based void fraction meter (IVFM) was developed specifically to measure void fraction and bubble size distributions beneath this wave. The following major conclusions can be drawn regarding air entrainment by the bow waves:

- *The air is entrained in spatially periodic bubble clouds.*

  In the larger scale experiments, the bubble clouds were 5 to 10 cm in diameter. The IVFM signals were processed using a cloud detection algorithm to find the rate of bubble cloud encounters. For depths between 1 and 3 cm beneath the free surface, the bubble cloud rates varied from 5 to 20 Hz. To our knowledge, these were the first observations and measurements of this periodic flow structure.

- *In the larger scale stationary model experiments, the bubble cloud void fraction could exceed 10% in the center of the cloud, and the bubble chords for the bubbles comprising*

the clouds were between 1 and 7 mm.

To our knowledge, these are the first experimental measurements which quantify the amount of air entrained by a bow wave. Void fraction mappings for different flow cross sections beneath the wave were produced, and the bubble chord distributions also were calculated for these locations.

- *For a given flow condition, the void fraction increases with the distance traveled along the impact line in the downstream direction.*

  The void fraction mappings were used to estimate the quantity of air entrained at different streamwise locations. If a larger number flow cross sections were measured, the total amount of air entrained by the wave could be calculated.

- *The frequency of the surface disturbances controls the frequency of the bubble clouds.* Further investigation of this hypothesis is necessary; however, a frequency of 11 Hz in the cross-correlations of the IVFM and wave gage signals indicated that it could be true. It appears that the surface disturbances divide the plunging liquid jet sheet into a series of individual plunging wave jets, and each jet entrains air into its own bubble cloud beneath the free surface.

6.2 Future work

This study is the first attempt to measure directly the quantity of air entrained by breaking bow waves and the main results are summarized in the preceding paragraphs. Many areas for improvement remain as well as other areas which could be interesting to explore. A few ideas are listed below:

- Exploration of "2D+t" numerical approach for bow flows around a wedge.
- More detailed investigation of scaling with geometric parameters.
- Development of an improved method of correlating the surface disturbances with the rate of bubble cloud formation.
- Development of dual-tipped conductivity probe or feature tracking software for bubble velocity measurements.

- Towed model or larger depth stationary model air entrainment experiments to investigate smaller bubble distributions and the bubble population dynamics.

In summary, bow flows are of continuing importance in the field of naval hydrodynamics and are quite complex. The need for experimental results in developing models for air entrainment by these waves and the associated bubble population dynamics is critical for advancing the understanding of these flows.

Appendix A

Electrical schematics

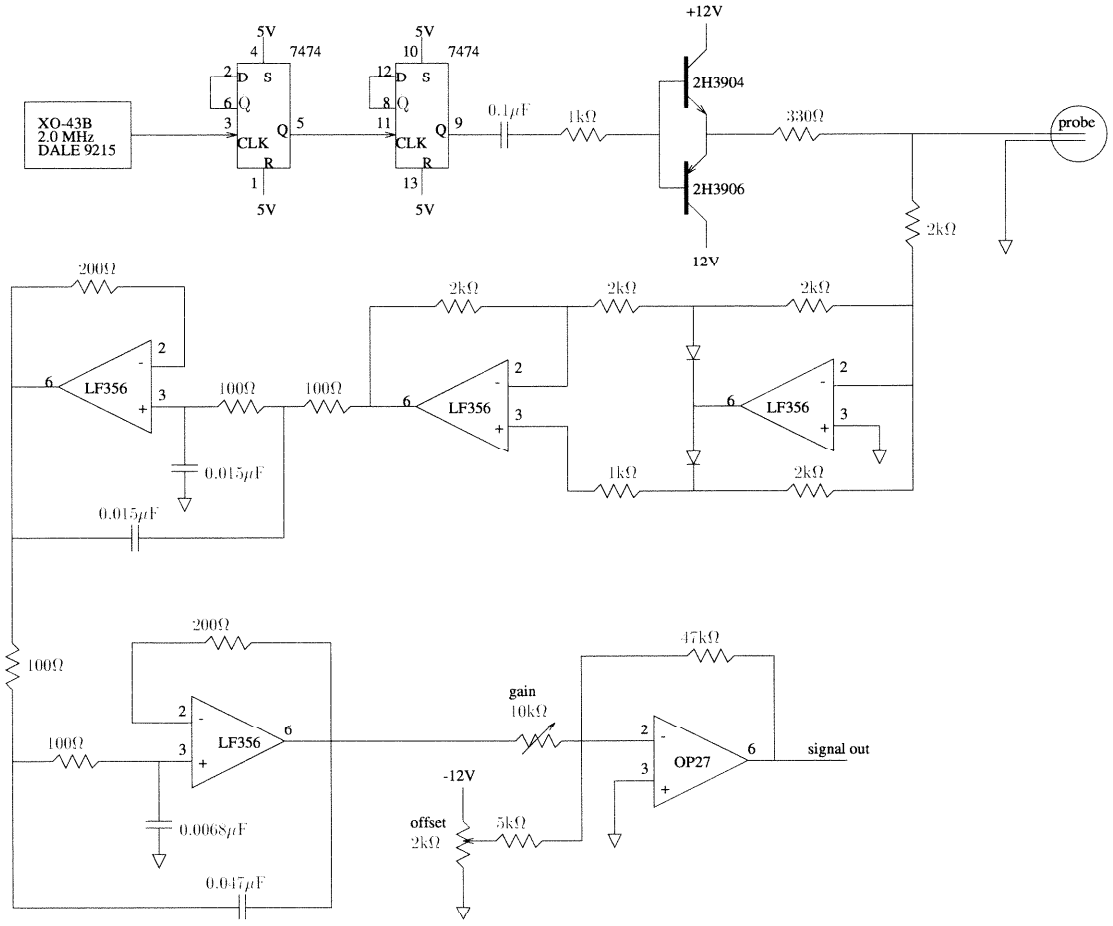

Figure A.1 Electrical schematic diagram of the impedance based void fraction meter (IVFM).

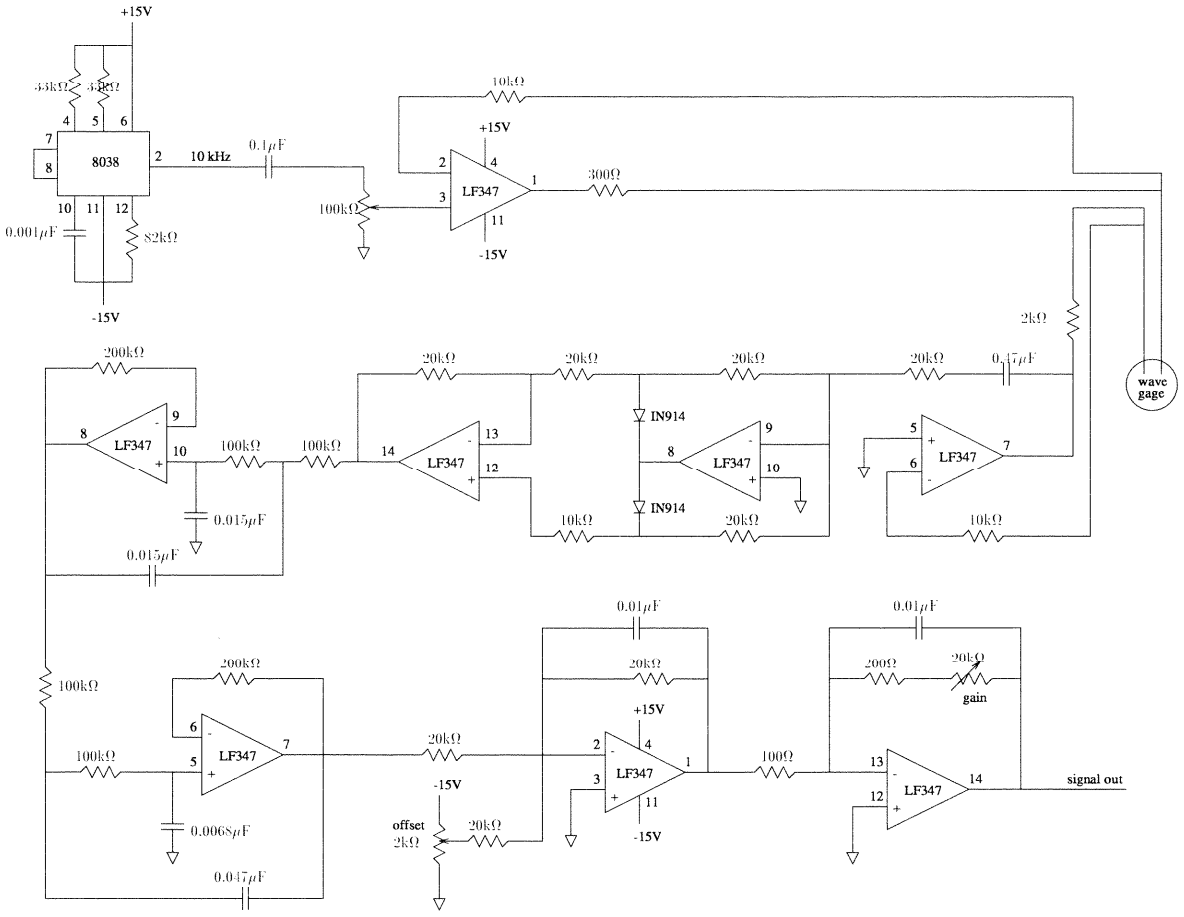

Figure A.2 Electrical schematic diagram of the linear wave gage.

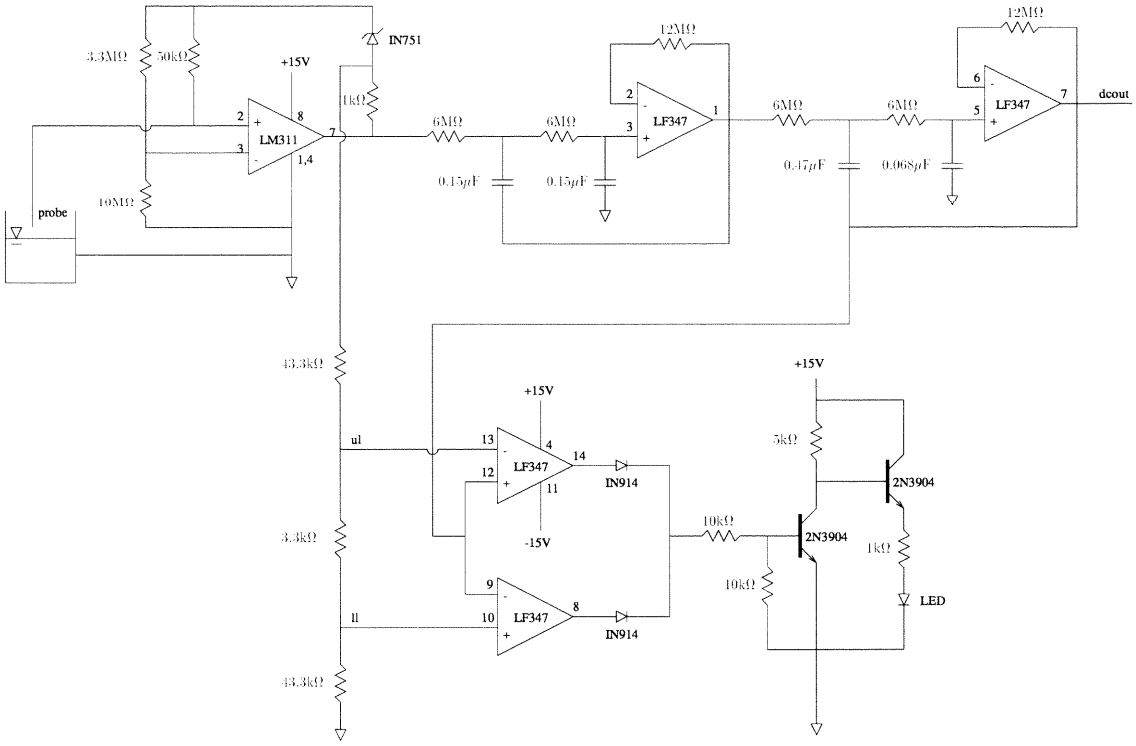

Figure A.3 Electrical schematic diagram of the free surface finder.

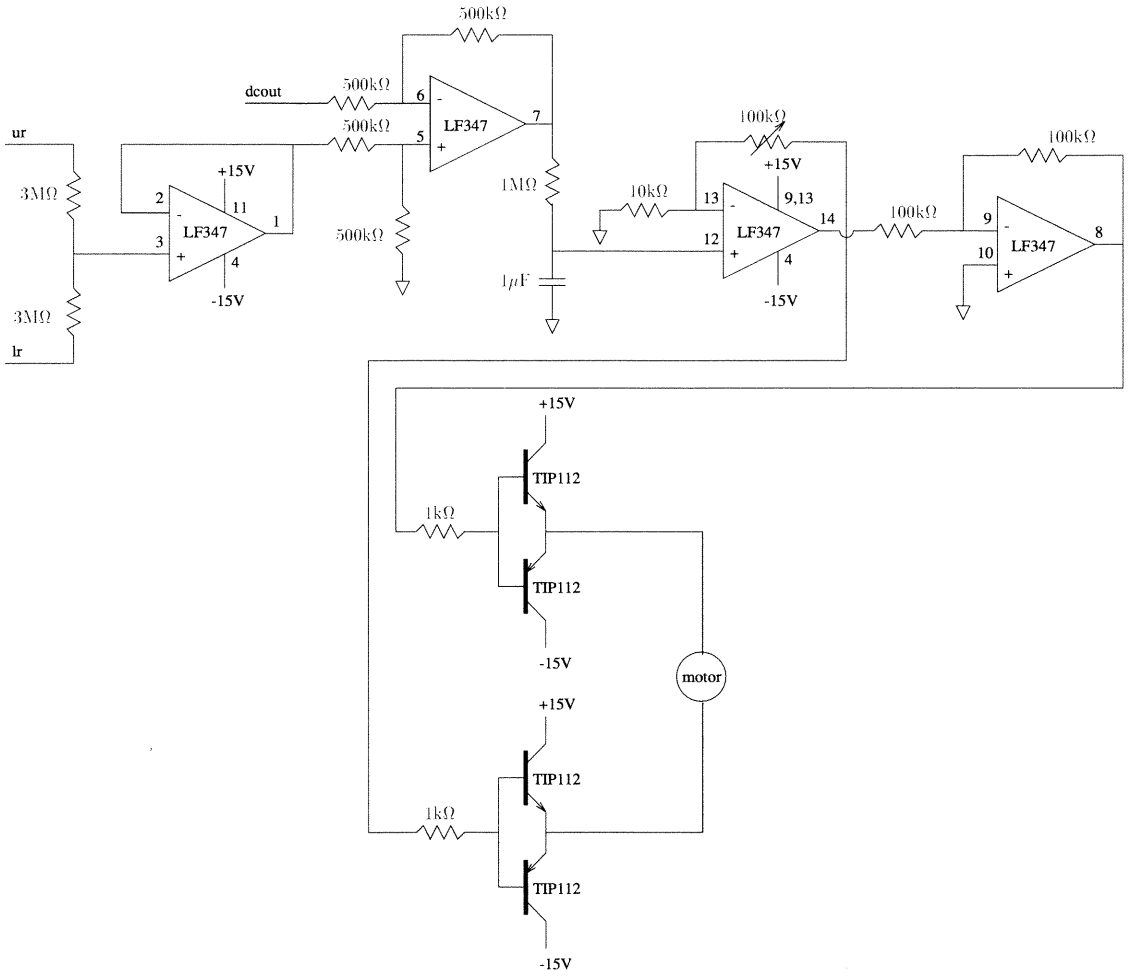

Figure A.4 Electrical schematic diagram of the servo motor driver. The labels "ur," "lr," and "dcout" connect to the free surface finder in Figure A.3.

Appendix B

Force measurements

For the towed model tests, the forces acting on the $\theta = 26°$ wedge were measured using two force cells which coupled it to the towing carriage. Data from the force cells was sampled at 200 Hz, and later low-pass filtered using a fourth order Butterworth filter with a 100 Hz cutoff frequency. Typical traces are shown in Figure B.1. Both the drag and the side force oscillate around some mean value. The average force was negative for the side force, indicating that the wedge was towed a few degrees toward port from its centerline. The data was detrended and FFT algorithms were used to examine the frequency content. The results corresponding to the signals in Figure B.1 are shown in Figure B.2. Both of the spectra have three sets of peaks. The largest peaks occur at 7 Hz for drag force and 10 Hz for side force, and are likely due to the mounting configuration of the wedge. The second largest peak in both spectra occurs at 3 Hz, the natural frequency of the carriage. A third peak occurs at 30 Hz, clearly aliased 60 Hz electrical line noise.

The mean value of the drag and side force was calculated for each run. Using

$$C_D = \frac{D}{\frac{1}{2}\rho U^2 A_p} \tag{B.1}$$

where A_p is the projected area, the drag coefficients for the $\theta = 26°$ wedge were calculated. Figure B.3 shows how these drag coefficients decreased with Froude number, $\mathbf{F}$.

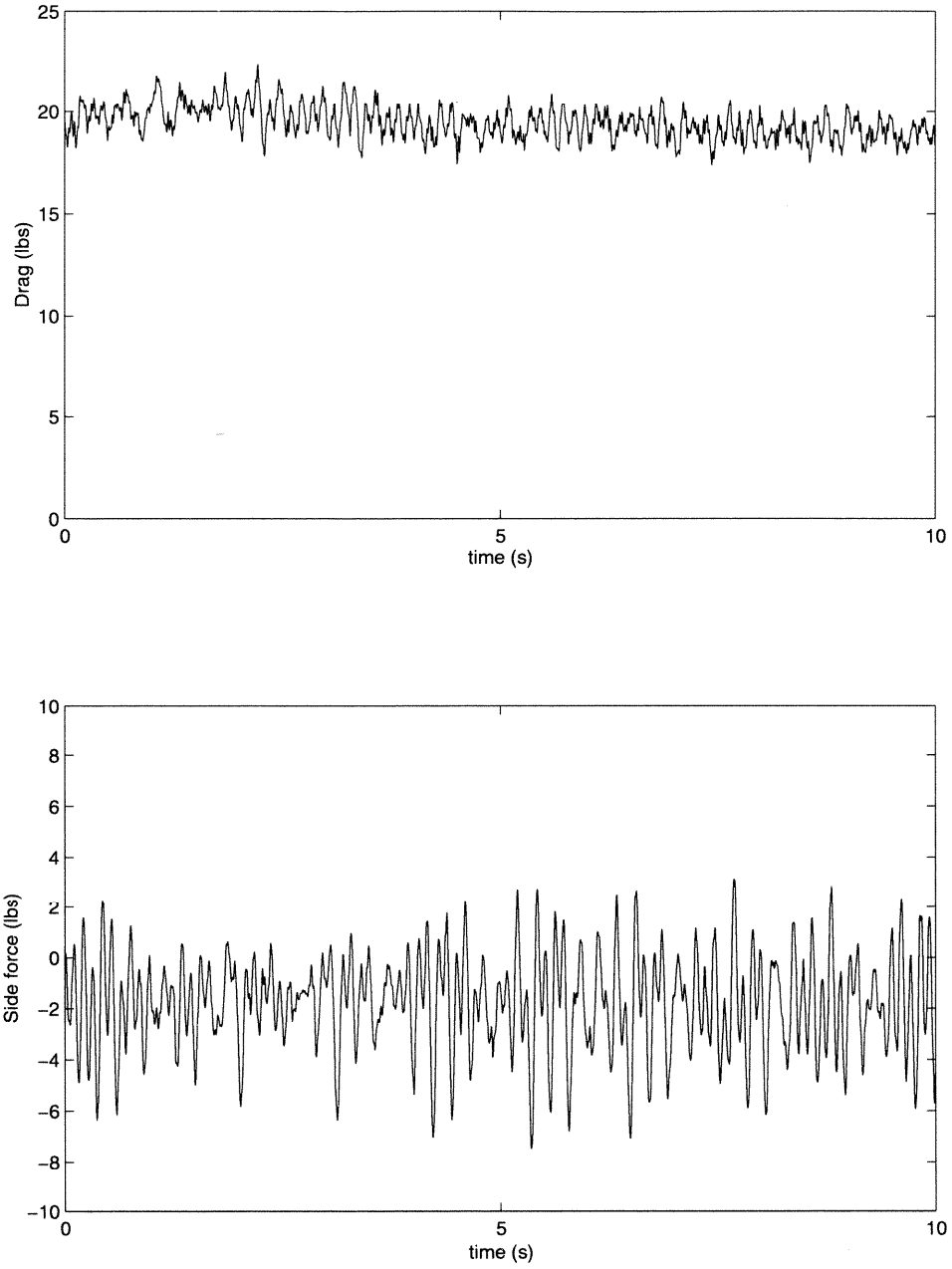

Figure B.1 Typical force cell data from the towed model experiments.

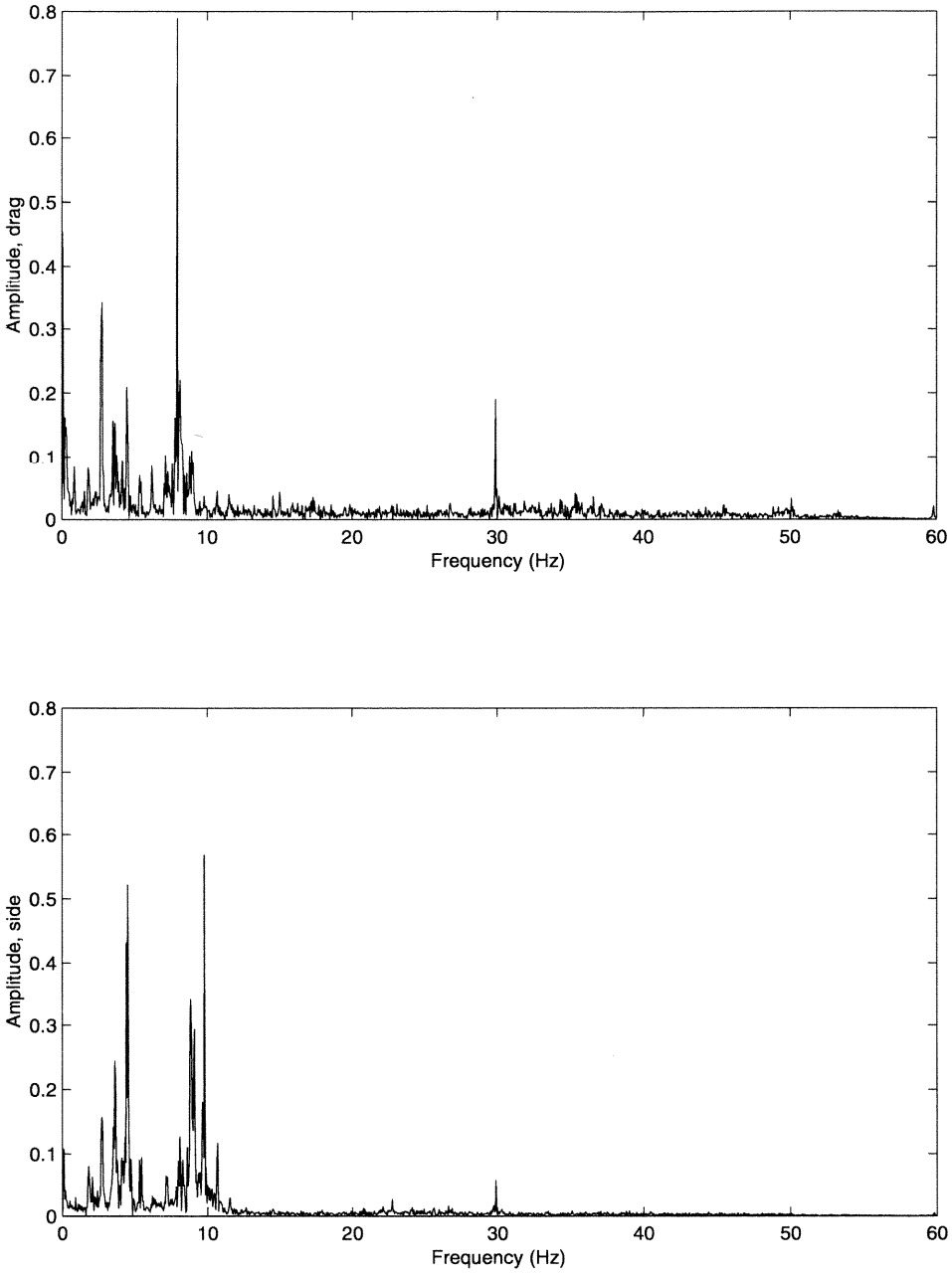

Figure B.2 FFTs of the force cell data shown in Figure B.1.

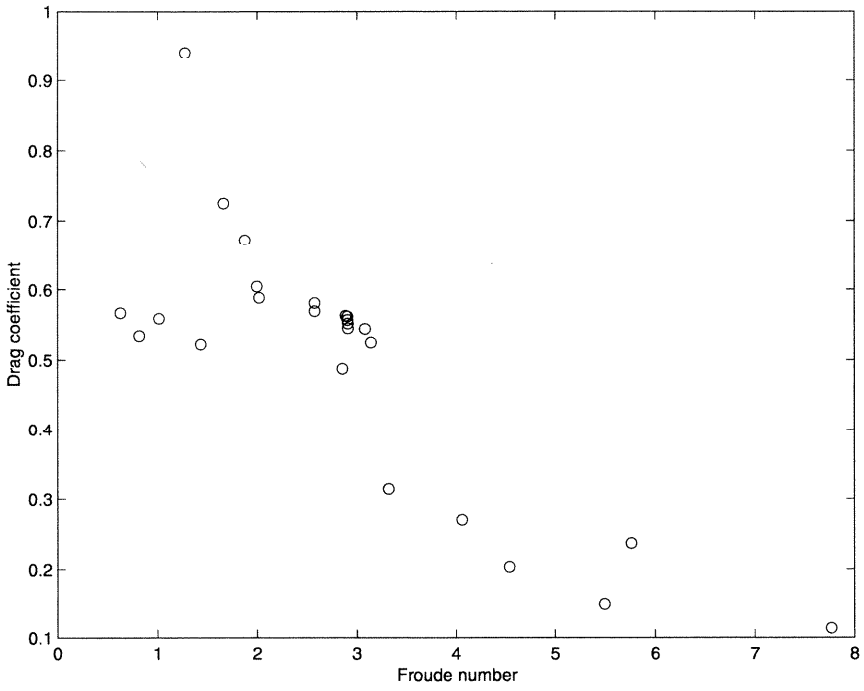

Figure B.3 Drag coefficient as a function of Froude number for the $\theta = 26°$ wedge model.

Appendix C

Void fraction measurements

The following figures contain time averaged, ensemble averaged, void fraction data for flow cross sections in the impact region of the plunging wave jet. Please refer to Chapter 5 for a more detailed description of the data.

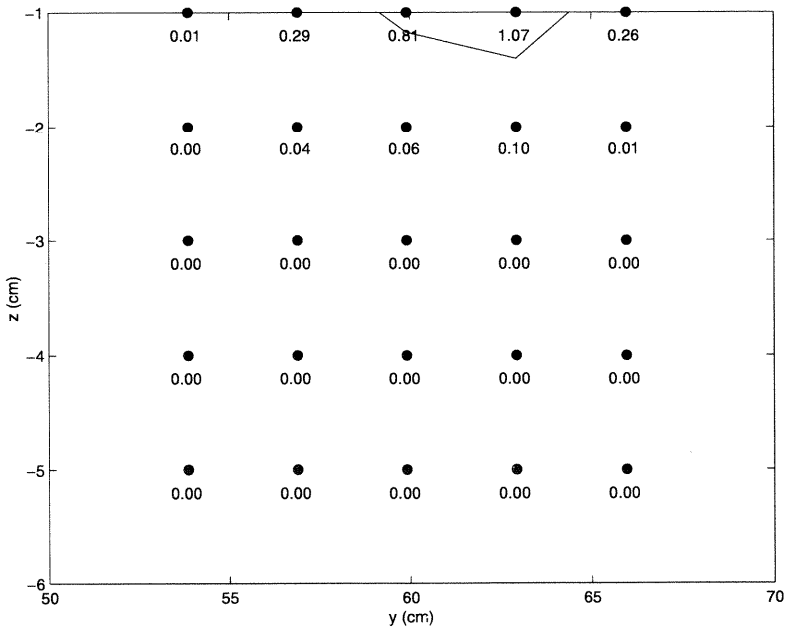

Figure C.1 Local time averaged void fraction cross section for $x = 73.4$ cm as viewed from downstream beneath the breaking wave; $\theta = 26°$, $\phi = 0°$, $U = 2.48$ m/s, $d = 7.89$ cm, and $\mathbf{F} = 2.82$.

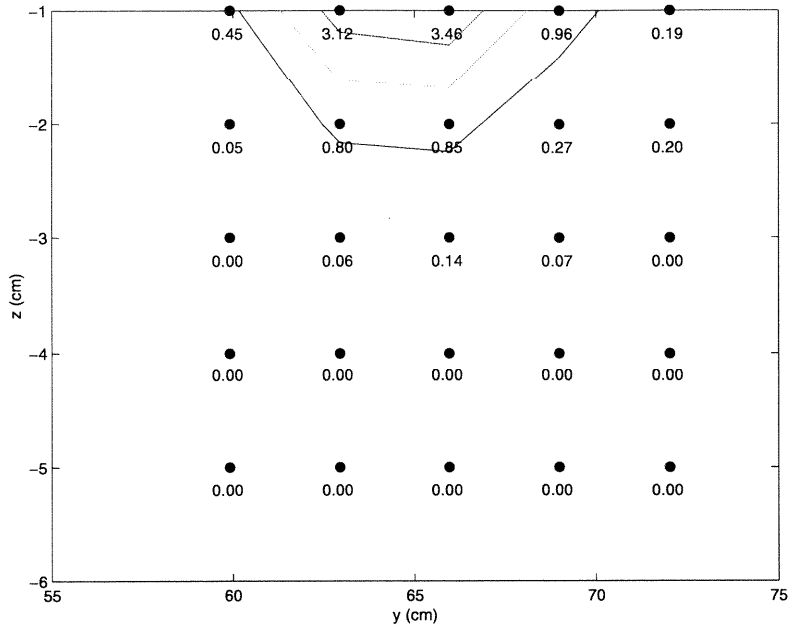

Figure C.2 Local time averaged void fraction cross section for $x = 81.0$ cm as viewed from downstream beneath the breaking wave; $\theta = 26°$, $\phi = 0°$, $U = 2.48$ m/s, $d = 7.89$ cm, and $\mathbf{F} = 2.82$.

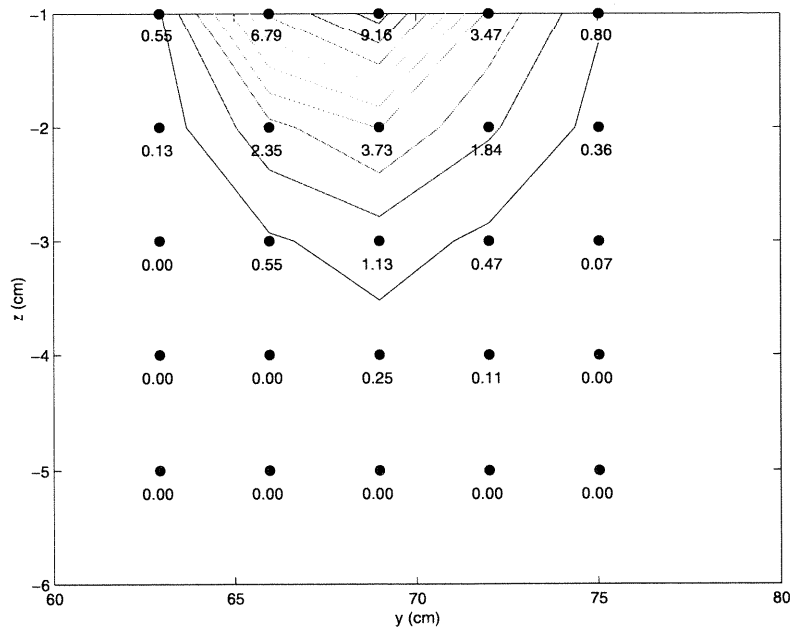

Figure C.3 Local time averaged void fraction cross section for $x = 91.2$ cm as viewed from downstream beneath the breaking wave; $\theta = 26°$, $\phi = 0°$, $U = 2.48$ m/s, $d = 7.89$ cm, and $\mathbf{F} = 2.82$.

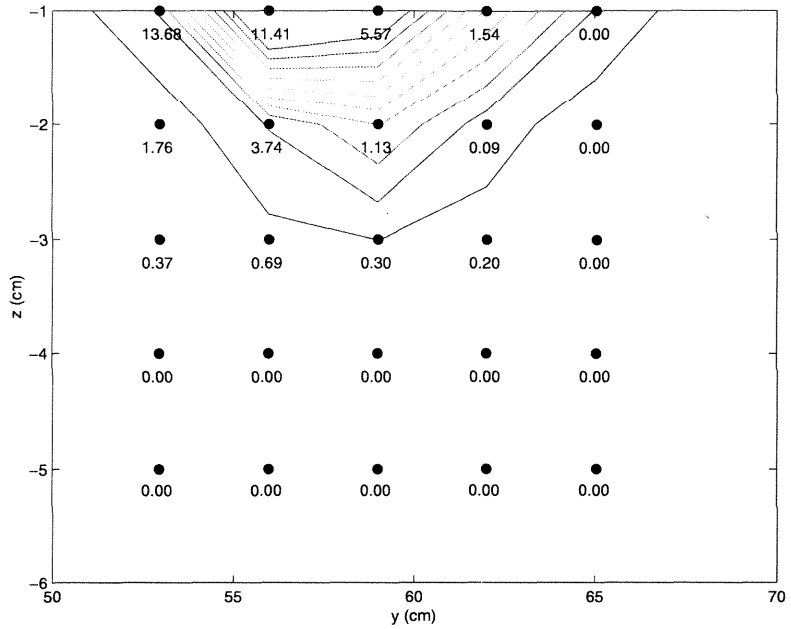

Figure C.4 Local time averaged void fraction cross section for $x = 70.8$ cm as viewed from downstream beneath the breaking wave; $\theta = 26°$, $\phi = 0°$, $U = 2.39$ m/s, $d = 6.47$ cm, and $\mathbf{F} = 3.00$.

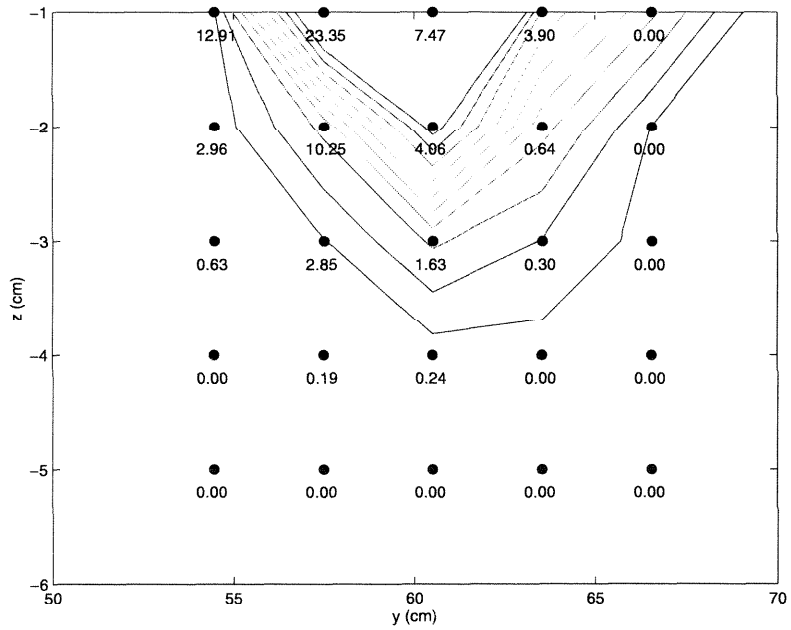

Figure C.5 Local time averaged void fraction cross section for $x = 75.9$ cm as viewed from downstream beneath the breaking wave; $\theta = 26°$, $\phi = 0°$, $U = 2.39$ m/s, $d = 6.47$ cm, and $\mathbf{F} = 3.00$.

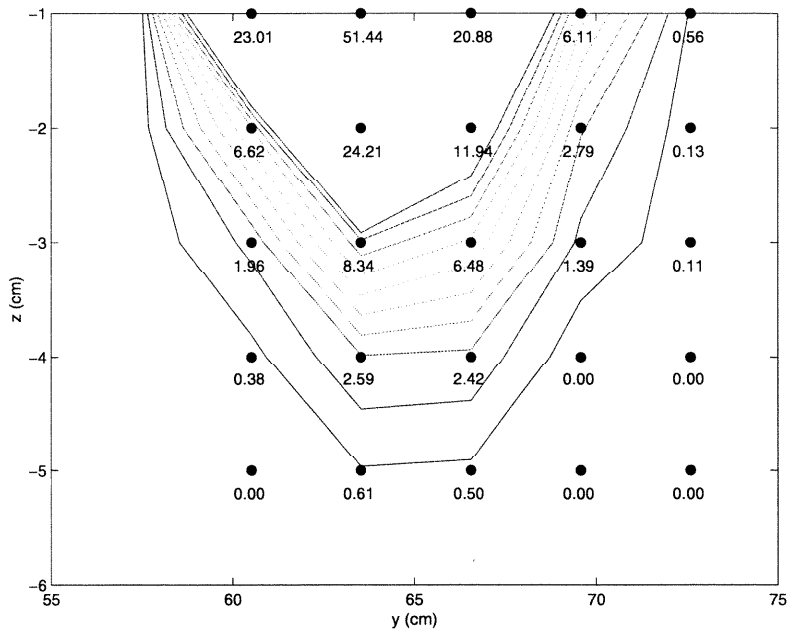

Figure C.6 Local time averaged void fraction cross section for $x = 84.2$ cm as viewed from downstream beneath the breaking wave; $\theta = 26°$, $\phi = 0°$, $U = 2.39$ m/s, $d = 6.47$ cm, and $\mathbf{F} = 3.00$.

Bibliography

[1] S. Baldy. A generation-dispersion model of ambient and transient bubbles in the close vicinity of breaking waves. *J. Geophysical Research*, 98(C10):18277–18293, 1993.

[2] R.N. Bernier. *Unsteady two-phase flow instrumentation and measurement.* PhD thesis, California Institute of Technology, Pasadena, California, 1982.

[3] A.K. Biń. Gas entrainment by plunging liquid jets. *Chemical Engineering Science*, 48(21):3585–3630, 1993.

[4] D.C. Blanchard and L.D. Syzdek. Mechanism for the water-to-air transfer and concentration of bacteria. *Science*, 170:626–628, 1970.

[5] D.C. Blanchard and A.H. Woodcock. Bubble formation and modification in the sea and its meteorological significance. *Tellus*, 9(2):145–158, 1957.

[6] F. Bonetto and R.T. Lahey. An experimental study on air carry under due to a plunging liquid jet. *Int. J. Multiphase Flow*, 19:281–294, 1993.

[7] P.M. Carrica et al. A polydisperse approach to the two-phase flow around a ship. Lyon, France, June 1998. Third International Conference on Multiphase Flow.

[8] J.W. Cartmill and M.Y. Su. Bubble size distribution under saltwater and freshwater breaking waves. *Dynamics of Atmospheres and Oceans*, 20:25–31, 1993.

[9] S.M. Çalişal and J.L.K. Chan. A numerical modeling of ship bow waves. *J. Ship Research*, 33(1):21–28, March 1989.

[10] H. Chanson. *A study of air entrainment and aeration devices on a spillway model.* PhD thesis, University of Canterbury, 1988.

[11] H. Chanson. Air bubble entrainment in free-surface turbulent flows. Technical Report CH46/95, University of Queensland, June 1995.

[12] H. Chanson and P.D. Cummings. Effects of plunging breakers on the gas contents in the ocean. *Marine Technology Society J.*, 28(3):22–32, 1994.

[13] H. Chanson and P.D. Cummings. Modeling air entrainment in plunging breakers. pages 783–792, Vancouver, Canada, August 1994. International Symposium: Waves-Physical and Numerical Modeling.

[14] R.B. Chapman. Free-surface effects of yawed surface-piercing plates. *J. Ship Research*, 20(3):125–136, September 1978.

[15] R.J. Cipriano and D.C. Blanchard. Bubble and aerosol spectra produced by a laboratory breaking wave. *J. Geophysical Research*, 86:8085–8092, 1981.

[16] P.D. Cummings and H. Chanson. Air entrainment in the developing flow region of plunging jets–part 1: theoretical development. *J. Fluids Engineering*, 119:597–602, 1997.

[17] P.D. Cummings and H. Chanson. Air entrainment in the developing flow region of plunging jets–part 2: experimental. *J. Fluids Engineering*, 119:603–608, 1997.

[18] R.M. Detsch and R.N. Sharma. The critical angle for gas bubble entrainment by plunging liquid jets. *Chemical Engineering Journal*, 44:157–166, 1990.

[19] W.H. Horrocks. Experiments made to determine the conditions under which specific bacteria derived from sewage may be present in the air of ventilating pipes, drains, inspection chambers, and sewers. *Proc. R. Soc. London*, 79B:255–266, 1907.

[20] M. Ishii. *Thermo-Fluid Dynamic Theory of Two-Phase Flow*. Eyrolles, Paris, 1975.

[21] G. Jensen. Berechnung der stationaren potentialstromung ein schiff unter berucksichtigung der nichtlinearen randbedingung an der wasseroberflache. Technical Report 484, Institut fur Schiffbau der Universitat Hamburg, 1988.

[22] B.R. Kerman, editor. *Sea Surface Sound-Natural Mechanisms of Surface Generated Noise in the Ocean*. Kluwer Academic, 1988. 639 pp.

[23] M. Koga. Bubble entrainment in breaking wind waves. *Tellus*, 34:481–489, 1982.

[24] H.K. Kytomaa. *Stability of the Structure in Multicomponent Flow*. PhD thesis, California Institute of Technology, Pasadena, California, 1987.

[25] E. Lamarre and W.K. Melville. Air entrainment and dissipation in breaking waves. *Nature*, 351:469–472, 1991.

[26] E. Lamarre and W.K. Melville. Instrumentation for the measurement of void-fraction in breaking waves: Laboratory and field results. *IEEE J. Oceanic Engineering*, 17(2):204–215, 1992.

[27] E. Lamarre and W.K. Melville. Void fraction measurements and sound-speed fields in bubble plumes generated by breaking waves. *J. Acoust. Soc. Am.*, 95(3):1317–1328, 1994.

[28] M.R. Loewen, M.A. O'Dor, and M.G. Skafel. Bubbles entrained by mechanically breaking waves. *J. Geophysical Research*, 101:20759–20769, 1996.

[29] M. Longuet-Higgins. On the disintegration of the jet in a plunging breaker. *J. Physical Oceanography*, 25(10):2458–2462, 1995.

[30] J.D. Maxwell. *A Treatise on Electricity and Magnetism*, volume 1. Clarendon Press, second edition, 1881.

[31] E.J. McKeogh. *A study of air entrainment using plunging water jets*. PhD thesis, Queen's University of Belfast, UK, 1978.

[32] E.J. McKeogh and D.A. Ervine. Air entrainment rate and diffusion pattern of plunging liquid jets. *Chemical Engineering Science*, 36:1161–1172, 1981.

[33] W.K. Melville. The role of surface-wave breaking in air-sea interaction. *Annual Rev. Fluid Mech.*, 28:279–321, 1996.

[34] H. Miyata and T. Inui. Non-linear ship waves. *Advances in Applied Mechanics*, 24:215–288, 1984.

[35] E.C. Monahan and M.A. Van Patten, editors. *Climate and Health Implications of Bubble-Mediated Sea-Air Exchange*. Connecticut Sea Grant College Program, 1989.

[36] S.-Y. Ni. *High Order Panel Methods for Potential Flows with Linear or Non-Linear Free Surface Boundary Conditions*. PhD thesis, Chalmers University of Technology, Goteborg, Sweden, 1987.

[37] F. Noblesse. A slender-ship theory of wave resistance. *J. Ship Research*, 27(1):13–33, 1983.

[38] F. Noblesse, D. Hendrix, and L. Kahn. Nonlinear local analysis of steady flow about a ship. *J. Ship Research*, 35(4):288–294, 1991.

[39] F.T. Ogilvie. The wave generated by a fine ship bow. *Proc. Ninth Symposium on Naval Hydrodynamics*, pages 1483–1524, 1969.

[40] R.D. Peltzer. White-water wake characteristics of surface vessels. NRL Memorandum Report 5335, Naval Research Laboratory, Washington, D.C., June 1984.

[41] A. Prosperetti, N.Q. Lu, and H.S. Kim. Active and passive acoustic behavior of bubble clouds at the ocean's surface. *J. Acoust. Soc. Am.*, 93(6):3117–3127, 1993.

[42] A. Prosperetti and H.N. Oguz. The impact of drops on liquid surfaces and the underwater noise of rain. *Annual Rev. Fluid Mech.*, 25:577–602, 1993.

[43] K. Sene. Air entrainment by plunging jets. *Chemical Engineering Science*, 43(10):2615–2623, 1988.

[44] S. Shroff and D. Liepmann. Spray generation over curved surfaces. ASME Fluids Engineering Division, June 1997.

[45] A. Teyssedou, A. Tapucu, and M. Lortie. Impedance probe to measure local void fraction profiles. *Rev. Sci. Instrum.*, 59(4):631–638, 1988.

[46] S.A. Thorpe. On the clouds of bubbles formed by breaking wind waves in deep water, and their role in air-sea gas thransfer. *Phil. Trans. R. Soc. London*, A304:155–210, 1982.

[47] M.P. Tulin and M. Wu. Divergent bow waves. Washington D.C., 1997. Twenty-First Symposium on Naval Hydrodynamics, National Academy Press.

[48] E. Van de Sande and J.M. Smith. Surface entrainment of air by high velocity water jets. *Chemical Engineering Science*, 28:1161–1168, 1973.

[49] E. Van de Sande and J.M. Smith. Jet break-up and air entrainment by low velocity turbulent water jets. *Chemical Engineering Science*, 31:219–224, 1976.

[50] V.A. Vanoni, N.H. Brooks, and F. Raichlen. 40m precision tilting flume. Technical Memo 67-3, W.M. Keck Laboratory of Hydraulics and Water Resources, California Institute of Technology, Pasadena, California, October 1967.